

1



2

# Exploiting CVD diamond properties for particle detection and identification

3

4

5

Matevž Červ

6

Vienna University of Technology

7

A thesis submitted for the degree of

8

*Doctor of technical sciences*

9

Geneva 2016



# <sup>10</sup> Contents

<sup>11</sup> <b>1</b>	<b>Introduction</b>	<b>1</b>
<sup>12</sup> 1.1	Fundamental research . . . . .	2
<sup>13</sup> 1.1.1	CERN . . . . .	3
<sup>14</sup> 1.1.2	Particle accelerators . . . . .	4
<sup>15</sup> 1.1.3	The ATLAS experiment . . . . .	5
<sup>16</sup> 1.1.4	Atominsttitut, Vienna . . . . .	6
<sup>17</sup> 1.1.5	n-ToF . . . . .	7
<sup>18</sup> 1.2	Particle detectors . . . . .	8
<sup>19</sup> 1.2.1	Semiconductor detectors . . . . .	9
<sup>20</sup> 1.2.2	Diamond sensors . . . . .	10
<sup>21</sup> <b>2</b>	<b>Signal formation in diamond</b>	<b>13</b>
<sup>22</sup> 2.1	Principles of signal formation in semiconductors . . . . .	14
<sup>23</sup> 2.1.1	Signal induction by moving charges . . . . .	16
<sup>24</sup> 2.1.2	Radiation-induced electrical pulses . . . . .	18
<sup>25</sup> 2.1.3	Signal charge fluctuations . . . . .	19
<sup>26</sup> 2.2	Carrier transport in a diamond sensor . . . . .	19
<sup>27</sup> 2.3	Electronics for signal processing . . . . .	22
<sup>28</sup> 2.3.1	Signal preamplifiers . . . . .	22
<sup>29</sup> 2.3.1.1	Current-sensitive amplifier . . . . .	23
<sup>30</sup> 2.3.1.2	Charge-sensitive amplifier . . . . .	24
<sup>31</sup> 2.3.1.3	Analogue electronic noise . . . . .	25
<sup>32</sup> 2.3.2	Analogue-to-digital converters . . . . .	25
<sup>33</sup> 2.3.3	Digital signal processing . . . . .	26
<sup>34</sup> <b>3</b>	<b>Experimental results</b>	
<sup>35</sup>	<i>Diamond irradiation study</i>	<b>28</b>
<sup>36</sup> 3.1	Measurement setup . . . . .	29
<sup>37</sup> 3.1.1	Preamplifiers . . . . .	29
<sup>38</sup> 3.1.1.1	Calibration . . . . .	30
<sup>39</sup> 3.1.2	Diamond samples . . . . .	31
<sup>40</sup> 3.1.3	Readout devices . . . . .	32
<sup>41</sup> 3.1.4	Setup for the efficiency study using $\beta$ particles . . . . .	32
<sup>42</sup> 3.1.5	Room temperature $\alpha$ -TCT setup . . . . .	33

## CONTENTS

---

43	3.1.6	Cryogenic $\alpha$ -TCT setup . . . . .	33
44	3.2	Charged particle pulses and spectra . . . . .	35
45	3.2.1	Noise limitations . . . . .	35
46	3.3	Radiation limitations . . . . .	37
47	3.3.1	Quantifying radiation damage in diamonds . . . . .	38
48	3.3.1.1	Irradiation with a $\pi_{300 \text{ MeV}}$ beam . . . . .	38
49	3.3.1.2	Charge collection efficiency and charge collection distance . . . . .	39
50	3.3.1.3	Irradiation damage factor . . . . .	40
52	3.3.2	Long-term measurement stability . . . . .	41
53	3.3.2.1	$\beta$ long-term stability . . . . .	42
54	3.3.2.2	$\alpha$ long-term stability . . . . .	43
55	3.4	Temperature limitations . . . . .	47
56	3.4.1	Temperature-variant $\alpha$ -TCT before irradiation . . . . .	49
57	3.4.2	Temperature-variant $\alpha$ -TCT after irradiation . . . . .	51
58	3.4.2.1	Collected charge as a function of temperature . . . . .	52
59	3.4.2.2	Charge trapping . . . . .	54
60	3.5	Conclusion . . . . .	58
61	<b>4</b>	<b>Charge monitoring</b>	
62		<i>The ATLAS Diamond Beam Monitor</i>	<b>59</b>
63	4.1	Luminosity measurements . . . . .	60
64	4.2	Diamond pixel module . . . . .	61
65	4.2.1	Sensors . . . . .	62
66	4.2.2	Front-end electronics . . . . .	63
67	4.3	Module assembly and quality control . . . . .	65
68	4.3.1	Assembly . . . . .	65
69	4.3.2	Testing . . . . .	66
70	4.3.3	Installation and commissioning . . . . .	67
71	4.4	Performance results . . . . .	68
72	4.4.1	Source tests . . . . .	68
73	4.4.2	Test beam results . . . . .	69
74	4.5	Operation . . . . .	72
75	4.5.1	Positioning . . . . .	72
76	4.5.2	Data taking during collisions . . . . .	73
77	4.6	Conclusion . . . . .	76
78	<b>5</b>	<b>Current monitoring</b>	
79		<i>Real-time particle identification</i>	<b>77</b>
80	5.1	Motivation . . . . .	78
81	5.2	Requirements . . . . .	78
82	5.3	Device specifications . . . . .	79
83	5.4	Pulse parameters . . . . .	79

## CONTENTS

---

84	5.5 Applications . . . . .	81
85	5.6 Description of the firmware . . . . .	82
86	5.6.1 Design constraints . . . . .	82
87	5.6.2 Analysis module . . . . .	83
88	5.6.3 Area and width measurement . . . . .	85
89	5.6.3.1 Vector cleaning . . . . .	86
90	5.6.3.2 Algorithm . . . . .	87
91	5.7 Control and data interface . . . . .	88
92	5.7.1 Software . . . . .	89
93	5.7.2 Data readout . . . . .	89
94	5.8 Performance results . . . . .	90
95	5.8.1 Comparison between the charge- and current-sensitive spec-	
96	troscopy . . . . .	91
97	5.9 Source calibration . . . . .	94
98	5.9.1 Source measurements – scatter plots . . . . .	96
99	5.9.1.1 $^{241}\text{Am}$ source . . . . .	96
100	5.9.1.2 $^{90}\text{Sr}$ and $^{60}\text{Co}$ source . . . . .	101
101	5.10 Applications in neutron instrumentation . . . . .	105
102	5.10.1 Thermal neutron flux monitoring . . . . .	105
103	5.10.1.1 Measurements . . . . .	106
104	5.10.1.2 Results and discussion . . . . .	107
105	5.10.1.3 Conclusion . . . . .	107
106	5.10.2 Fusion power monitoring . . . . .	107
107	5.10.2.1 Measurements . . . . .	108
108	5.10.2.2 Results and discussion . . . . .	109
109	5.10.2.3 Conclusion . . . . .	109
110	5.10.3 Fast and thermal neutron monitoring . . . . .	111
111	5.10.3.1 Measurements . . . . .	111
112	5.10.3.2 Results and discussion . . . . .	113
113	5.10.3.3 Conclusion . . . . .	113
114	5.11 Conclusion . . . . .	114

# <sup>115</sup> List of Figures

<sup>116</sup> 1.1	Standard model [22] . . . . .	3
<sup>117</sup> 1.2	The Large Hadron Collider [20] . . . . .	5
<sup>118</sup> 1.3	The ATLAS Experiment [38] . . . . .	6
<sup>119</sup> 1.4	The TRIGA MARK II neutron reactor [15] . . . . .	7
<sup>120</sup> 1.5	The calorimeter in the n-ToF area [19] . . . . .	8
<sup>121</sup> 1.6	The Insertable B-Layer – a silicon particle tracker installed in the ATLAS experiment in 2014 [34] . . . . .	10
<sup>122</sup> 1.7	A pCVD diamond pad detector [23] . . . . .	11
<sup>124</sup> 2.1	In the equivalent electrical circuit diagram, electron-hole creation and drift can be modelled as a current source with a capacitor in parallel . . . . .	15
<sup>125</sup> 2.2	Stopping power for muons according to the Bethe-Bloch formula [] . . . . .	16
<sup>126</sup> 2.3	A point-like charge inducing current in a conductive plane . . . . .	17
<sup>127</sup> 2.4	Charge carrier drift in diamond for $\beta/\gamma$ and for $\alpha$ particles . . . . .	18
<sup>128</sup> 2.5	Calculated intrinsic energy resolution for silicon and diamond . . . . .	20
<sup>129</sup> 2.6	Introduction of space charge in the diamond bulk. The induced current signal is proportional to the effective electrical field. $d$ is the thickness of the diamond sensor. . . . .	21
<sup>130</sup> 2.7	Introduction of impurities and non-uniformities into the crystal lattice due to radiation damage. . . . .	22
<sup>131</sup> 2.8	Simplified equivalent circuits of a current and charge amplifier . . . . .	23
<sup>132</sup> 2.9	Input and output signal of the current amplifier . . . . .	24
<sup>133</sup> 2.10	Input and output signal of the charge amplifier . . . . .	24
<sup>134</sup> 2.11	Input signal digitisation and quantisation error . . . . .	26
<sup>135</sup> 2.12	An example of an FPGA and an ASIC chip . . . . .	27
<sup>140</sup> 3.1	Diagram of a diamond detector readout chain. . . . .	29
<sup>141</sup> 3.2	Amplifiers used for the charge and current measurements . . . . .	30
<sup>142</sup> 3.3	Two scCVD diamond samples: A IIa 1scdhq (left) and an E6 S37 (right)	31
<sup>143</sup> 3.4	Positioning of the $\alpha$ -source on top of the sensor carrier . . . . .	34
<sup>144</sup> 3.5	Superimposed and averaged pulses (a, b and c, current amplifier) and distributions of deposited energy (d, e, f, charge amplifier) for three types of radiation. Note the scale on the X axis of the distributions. .	36

---

*LIST OF FIGURES*

---

147	3.6	Diamond radiation damage - a model based on displacements per atom [26]. Added are data points for protons and pions by RD42 [35] and one data point for pions measured in the scope of this thesis. . . . .	39
148	3.7	First figure shows the CCD for S37, S79 and S52 at a range of bias voltage settings. The charge collection distance at 1 V/ $\mu\text{m}$ bias voltage for the three diamond samples is then compared to the RD42 data for pion irradiation in the second figure. The data points are about 15–25 % lower than expected from the RD42 data [35]. . . . .	41
149	3.8	Relative increase of charge collection over time due to priming with the $^{90}\text{Sr}$ radioactive source. The charge collection for the non-irradiated S37 stays constant. The bias voltage for this measurement is 1 V/ $\mu\text{m}$ . . . . .	43
150	3.9	Relative decrease of collected charge with time for non-irradiated and irradiated diamond samples. . . . .	44
151	3.10	The signal of the irradiated and primed S79 deteriorates with time for both polarities. Every plot contains 60 superimposed pulses. . . . .	45
152	3.11	Deterioration of the pulse shapes with time . . . . .	46
153	3.12	Comparison of the five procedures for the “healing” process for an irradiated diamond that had been exposed to $\alpha$ radiation with a rate of $10^1 \text{ s}^{-1}$ , with the bias voltage switched on, for at least 30 minutes. . . . .	48
154	3.13	Varied bias voltage at a fixed temperature . . . . .	49
155	3.14	Several data points between 4 K and 295 K at a bias voltage of $\pm 500 \text{ V}$ . . . . .	50
156	3.15	Varied bias voltage at a fixed temperature for an irradiated sample . . . . .	52
157	3.16	After irradiation: several data points between 4 K and 295 K at a bias voltage of $\pm 500 \text{ V}$ . . . . .	53
158	3.17	Collected charge as a function of temperature . . . . .	55
159	3.18	Charge carrier lifetime decreases with irradiation, but is stable across the range of temperatures between 4 K – 75 K and 150 K – 295 K. The first figure shows the carrier lifetime s a function of temperature whereas the second figure depcits the carrier lifetime averaged over all temperatures and plotted against the $\pi$ irradiation dose . . . . .	57
160	4.1	Diamond detectors installed in high-energy physics experiments in the last decade, sorted by the active sensor area. The first four detectors from the left are radiation monitors whereas the right two are pixel trackers. . . . .	60
161	4.2	DBM module, top-down view. Visible is the flexible PCB with signal and power connections, the silicon sensor and a part of the FE-I4. Wire bonds from the PCB to the FE-I4 and to the sensor are also visible. . . . .	61
162	4.3	A pCVD wafer. The golden dots on the surface are the electrodes that are applied during the qualification test. The wafer is measured across the surface to find the regions with the highest efficiency. . . . .	62

## LIST OF FIGURES

---

187	4.4	FE-I4 layout, top-down view. The pink area are pixels grouped into columns, the green area below is the common logic and the red strip at the bottom are the wire bond pads. . . . .	63
188	4.5	Schematic of an analog pixel. Courtesy of the FE-I4 collaboration. . .	64
189	4.6	Module production with time . . . . .	67
190	4.7	Occupancy and pseudo-efficiency scans for the silicon (left) and diamond sensor (right) to check for disconnected regions and estimate the sensor's efficiency. Shadows of the electronic components are clearly visible because fewer electrons were able to traverse through such a higher amount of material. . . . .	70
191	4.8	Measurements of pseudo-efficiency and disconnected regions for all modules that went through the QC procedure . . . . .	71
192	4.9	An efficiency study of a prototype DBM diamond module in a test beam. The statistics are low ( $\sim 10$ hits/pixel) as the data was collected during a short run. . . . .	71
193	4.10	This photo highlights four telescopes installed onto the nSQPs and around the pipe . . . . .	72
194	4.11	Position of the DBM in the ATLAS experiment . . . . .	73
195	4.12	Occupancy of individual modules during collisions. Only 16 modules were taking data. . . . .	74
196	4.13	A diagram showing the radial distance $R_0$ and longitudinal distance $Z_0$ of the trajectory from the interaction point at the minimal distance $d$ . $Z$ is the axis along the beam line. Three module planes intercept a particle and reconstruct its trajectory. . . . .	74
197	4.14	These two plots show two parameters of particle tracks recorded by one of the DBM telescopes: radial and longitudinal distance of the projected tracks from the interaction point. . . . .	75
198	5.1	A pulse and its parameters . . . . .	80
199	5.2	Form Factor is the ratio between the measured area ( $a$ ) and the calculated area ( $A \times BW$ ) of the pulse. The calculated area is significantly larger than the measured area for a triangular triangular pulse, but less so for the rectangular one. The red and blue dot in the right plot are the value entries of the two pulses shown. The red and blue oval shapes depict the regions for the values expected from triangular and rectangular pulses. By carefully choosing the linear qualifier (dashed line) and taking only the entries below the cut rectangular pulses can be identified. . . . .	80
200	5.3	Firmware design structure . . . . .	82
201	5.4	Code design plan . . . . .	83

---

*LIST OF FIGURES*

226	5.5	A sample pulse. The first vector shows which samples are above the width measurement height. The second vector is a clean vector. The third line shows the position of the maximum amplitude. The vector cleaning algorithm starts from the maximum amplitude and continues in both ways along the vector. . . . .	86
227	5.6	This block counts the remaining binary ones in the clean vectors and outputs this value as the pulse width. . . . .	86
228	5.7	This block masks the input data with the clean vector and sums the remaining samples. . . . .	87
229	5.8	Vector cleaning routine outputs two vectors - one forward in time and one back in time from the peak of the pulse. . . . .	87
230	5.9	One logic step in the algorithm chain before and after Karnaugh minimisation. . . . .	88
231	5.10	Vector is divided into two 16-bit logic chains. The algorithm logic is then run on the two chains separately. The results are then merged into one 32-bit clean vector by using a set of AND gates. . . . .	88
232	5.11	Abstraction levels of the controller software . . . . .	89
233	5.12	This figure shows the capability of the device to analyse all arriving pulses for a range of input frequencies. The highest achievable rate with zero lost pulses is $5 \times 10^6$ s $^{-1}$ . . . . .	91
234	5.13	These diagrams show the linearity of the measurements and their stability with respect to analog noise. . . . .	92
235	5.14	Spectrum of a $^{148}\text{Gd}^{239}\text{Pu}^{241}\text{Am}^{244}\text{Cm}$ source using a Cx and a C2 amplifier . . . . .	93
236	5.15	Accumulated pulses for all runs . . . . .	95
237	5.16	$^{241}\text{Am}$ , e $^-$ collection. Qualifier: FWHM. Optional qualifiers: Amplitude, Form Factor. . . . .	98
238	5.17	$^{241}\text{Am}$ , h $^+$ collection. Qualifier: FWHM. . . . .	99
239	5.18	$^{241}\text{Am}$ area histograms for electron and hole collection. . . . .	100
240	5.19	$^{90}\text{Sr}$ scatter plots . . . . .	102
241	5.20	$^{60}\text{Co}$ scatter plots . . . . .	103
242	5.21	Energy distributions for $\gamma$ and $\beta$ particles. . . . .	104
243	5.22	Thermal neutrons, photons. Qualifier: FWHM. . . . .	107
244	5.23	Energy spectrum after applied qualifiers reveals the tritium and $\alpha$ peak	108
245	5.24	$^{239}\text{Pu}$ Be. Qualifiers: BW-FWHM, FWHM, Form Factor . . . . .	110
246	5.25	$^{239}\text{Pu}$ Be, energy distribution of the neutrons interacting in the ballistic centre. . . . .	111
247	5.26	Fast neutrons, thermal neutrons, photons. Qualifiers: BW-FWHM, FWHM, Form factor, Slope. . . . .	112
248	5.27	Energy spectrum in CROCUS before and after applied qualifiers . . . . .	113

*LIST OF FIGURES*

---

<sup>266</sup> **Chapter 1**

<sup>267</sup> **Introduction**

<sup>268</sup> The aim of the thesis is to present and discuss applications of diamond based particle  
<sup>269</sup> detectors.

<sup>270</sup> The introductory chapter paints a picture of the current state of particle physics  
<sup>271</sup> research. It presents some of the research institutes that are active in this field,  
<sup>272</sup> pushing the boundaries of human knowledge further. It explains their goals and the  
<sup>273</sup> means with which they are achieving them. Next section describes particle detectors  
<sup>274</sup> in a broad sense – their history and the types existing now. One type in particular –  
<sup>275</sup> a diamond detector – is then described more in detail.

<sup>276</sup> Second chapter discusses the properties of diamond detectors. Dissecting the  
<sup>277</sup> detector chain into individual parts and describing them in detail – sensors, amplifiers,  
<sup>278</sup> digitisers and signal processing units. We learn about energy resolution in diamond,  
<sup>279</sup> analog and digital noise contribution etc. Principles of signal formation are presented,  
<sup>280</sup> starting with the famous Shockley-Ramo theorem and building from there. We will  
<sup>281</sup> see that different types of radiation induce different electrical signals.

<sup>282</sup> The base laid down in the second chapter is complemented in the third where the  
<sup>283</sup> measurements are presented and the results discussed. The focus is on diamond's  
<sup>284</sup> measurement stability with respect to irradiation damage. To carry out this study,  
<sup>285</sup> two diamond sensors were irradiated to two different doses, with the measurements  
<sup>286</sup> carried out before and after irradiation.

<sup>287</sup> Building on the understanding of the behaviour of the diamond, two applications  
<sup>288</sup> were developed. The fourth chapter describes the Diamond Beam Monitor, a detec-  
<sup>289</sup> tor that makes use of the diamond's charge measurement capabilities and its high  
<sup>290</sup> radiation hardness. This detector has been installed in one of the largest particle  
<sup>291</sup> physics experiments in the world and is currently taking data. Here, its development  
<sup>292</sup> process is presented: the quality control procedures during assembly and installation,  
<sup>293</sup> its performance in the test environment and some recent experimental data.

<sup>294</sup> The final and most important chapter describes the real-time application for par-  
<sup>295</sup> ticle identification. Here the shape of the electrical signal of the diamond sensor is  
<sup>296</sup> used to discriminate different types of radiation in real time and dead time free. The  
<sup>297</sup> chapter includes the description of the device's logic and algorithms, lab test results  
<sup>298</sup> and the application in neutron monitoring.

## <sup>299</sup> 1.1 Fundamental research

<sup>300</sup> This section gives a short overview of the institutes and collaborations carrying out  
<sup>301</sup> fundamental physics research. The facilities were used for the research carried out in  
<sup>302</sup> this thesis.

<sup>303</sup> The aim of fundamental (even pure or basic) research is to improve the scientific  
<sup>304</sup> theories and verify them to improve our understanding of the universe. It does not  
<sup>305</sup> in itself focus on applying this research by developing products and is not meant to  
<sup>306</sup> create a direct return on investment. Instead, it expands the overall knowledge of the  
<sup>307</sup> human kind - by making the results freely available to the general public.

<sup>308</sup> Particle physics research peers into the smallest constituents of the universe, dis-  
<sup>309</sup> secting the atoms into quarks and electrons, catching cosmic rays and figuring out  
<sup>310</sup> what dark matter is made up of. Particle physicists want to explain the phenomena  
<sup>311</sup> surrounding us by studying the fundamental particles and the mechanisms governing  
<sup>312</sup> their interactions. By understanding this, we would be able to answer difficult ques-  
<sup>313</sup> tions; How did the universe begin? What is the invisible force (dark matter, dark  
<sup>314</sup> energy) pushing the galaxies apart from each other? Where does mass come from?  
<sup>315</sup> Why is there almost no antimatter in the universe? In this effort, scientists have  
<sup>316</sup> formed several theories. One of them, the Standard Model of particles, is currently  
<sup>317</sup> the best theory to describe the visible universe.

<sup>318</sup> **The Standard Model** (SM) is a physics theory developed in the 1970's [37]. It  
<sup>319</sup> was designed to explain the current experimental results. As such, it was also able to  
<sup>320</sup> predict new discoveries and was a driving force for the scientists to invest time and  
<sup>321</sup> money in developing new experiments. To date, it is by far the most established and  
<sup>322</sup> verified physics theory. It explains how the basic building blocks of matter – *fermions*  
<sup>323</sup> – interact with each other via mediators of interactions called *bosons*. There are two  
<sup>324</sup> main families of fermions - *quarks* and *leptons*, as shown in diagram 1.1. Each group  
<sup>325</sup> consists of six members divided into three *generations*, the first being the lightest and  
<sup>326</sup> most stable and the last the heaviest – unstable. The nature around us is made up  
<sup>327</sup> of the stable particles – those from the second or third generations can only be found  
<sup>328</sup> in cosmic rays or produced artificially using particle accelerators.

<sup>329</sup> Quarks have a spin of 1/2 and a charge of either +2/3 (up, charm, top) or -1/3  
<sup>330</sup> (down, strange, bottom) while the leptons have a spin of 1/2 and a charge of either 1  
<sup>331</sup> (electron, muon, tau) or 0 (electron neutrino, muon neutrino, tau neutrino). Leptons  
<sup>332</sup> only exist individually – they do not cluster. Quarks, however, immediately form a  
<sup>333</sup> cluster of either two (unstable), three (more stable) or five (unstable). Two up and  
<sup>334</sup> one down quark make up a proton whereas two down and one up quark make up a  
<sup>335</sup> neutron.

<sup>336</sup> In addition to fermions, each particle has its corresponding antiparticle – a particle  
<sup>337</sup> with the same mass but the opposite charge. If an antiparticle hits a particle, they  
<sup>338</sup> annihilate each other, producing energy in form of photons.

<sup>339</sup> Bosons are the carriers of force, mediating weak ( $W^+$ ,  $W^-$  and  $Z$  bosons), strong

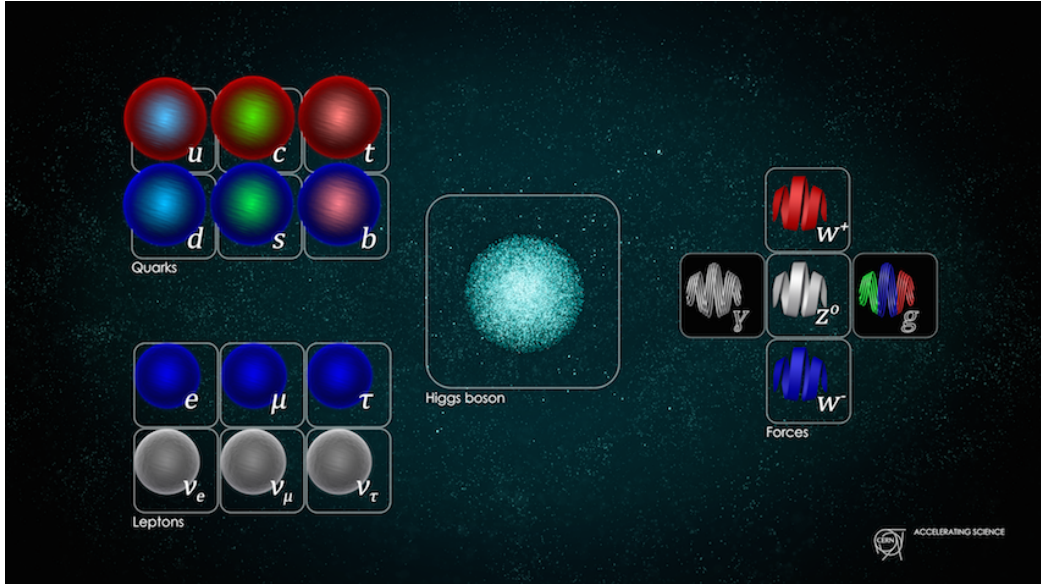


Figure 1.1: Standard model [22]

(gluons) and electromagnetic (photons) interactions. The weak interaction is responsible for the radioactive decay of subatomic particles, thus playing an essential role in nuclear fission – a process taking place in the stars. The electromagnetic interaction works at a macroscopic level – it allows particles to interact via electric and magnetic fields. The strong interaction is effective at distances of a femtometer and it governs how quarks interact and bind with each other. An additional boson is the Higgs boson and was discovered at CERN in 2012 [6]. It is a representation of the Higgs mechanism, which gives rise to the mass (or lack thereof) of all the particles in the Standard Model.

### 1.1.1 CERN

CERN (European Centre for Nuclear Research) [6] is a nuclear research institute housing the largest particle physics laboratory in the world. It straddles the Swiss-French border just outside Geneva. It was established in 1954 to bring the war-torn Europe together by means of fundamental scientific research. Today, it has 22 member state countries and several observer states. More than 10000 scientists, engineers, technicians, students and others from all around the globe work at CERN on many projects in research fields ranging from particle to nuclear physics. The scope is to probe the fundamental structure of the universe and to understand the mechanisms governing it. Therefore CERN's main function is to provide the infrastructure for high-energy physics experiments. These are carried out using large machines called particle accelerators. These instruments boost beams of particles to high energies before making them collide with each other or with stationary targets. The resulting collisions are recorded by particle detectors and later analysed by physicists. To carry out research on the smallest constituents of matter, their dynamics and struc-

## 1.1. FUNDAMENTAL RESEARCH

---

ture, very high energies are needed. This is why the most powerful accelerators are used for fundamental research. The largest accelerators at CERN are the Proton Synchrotron [], the Super Proton Synchrotron [36] and the Large Hadron Collider [].

### 1.1.2 Particle accelerators

A particle accelerator is a machine that accelerates beams of charged particles like protons, electrons, ions etc. It generates electric fields that add kinetic energy to the particles, speeding them up. It then uses magnets to retain them within a defined trajectory and inside the evacuated beam pipe. The trajectory can be either linear (linear accelerators) or circular (circular or cyclic accelerators). The advantage of the latter ones is that they can accelerate particles many times while keeping them in orbit.

Particle accelerators are used in numerous fields ranging from fundamental and material research, cancer treatment to industrial applications, such as biomedicine and material processing. There are several types of accelerators existing: electrostatic accelerators, linear accelerators (LINACs), cyclotrons, synrocyclotrons, synchrotrons, synchrotron radiation sources and fixed-field alternating gradient accelerators (FFAGs).

**The Large Hadron Collider** (LHC, figure 1.2) at CERN is the largest particle collider in the world. It is a 27 km long circular machine set up in a tunnel deep under the surface (ranging from 50 to 175 m). It accelerates two proton beams to the energy of 6.5 TeV per beam before it makes them to collide with each other at four different points around its circumference. The LHC was build between 1998 and 2008 and was first successfully started in 2010 and operated stably until 2013 when it underwent a two years long upgrade. They restarted its operation at the beginning of 2015. The hair-thin particle beams travel inside two evacuated pipes with a  $\sim$ 5 cm radius. Coils made up of a superconductive material are wound up around the pipes in special patterns. When they are cooled down to -271 °C using liquid helium, they become superconductive - the resistivity of the material drops significantly, minimising the heat dissipation despite high electric currents. These produce strong magnetic fields which bend the particles and keep them in a circular trajectory. The particles are accelerated when traversing the radiofrequency (RF) cavities with the RF frequency of 400 MHz. This oscillating frequency creates buckets – compartments for bunches of highly energetic particles – which are 2.5 ns long. Only one out of ten buckets is being filled, so the bunches are spaced at 25 ns. This defines the machine's clock as well as the maximum rate of collisions - the bunches travelling in the opposite direction will cross at the intersections up to 40 million times per second. Currently around 20 collisions occur during every bunch crossing, making the maximum collision rate of  $10^9$  per second. The number of collisions will further increase in the next years, when they will increase the number of particles in every bunch and decrease the transverse spread of the bunches – squeeze them, therefore increase their density and the collision probability.

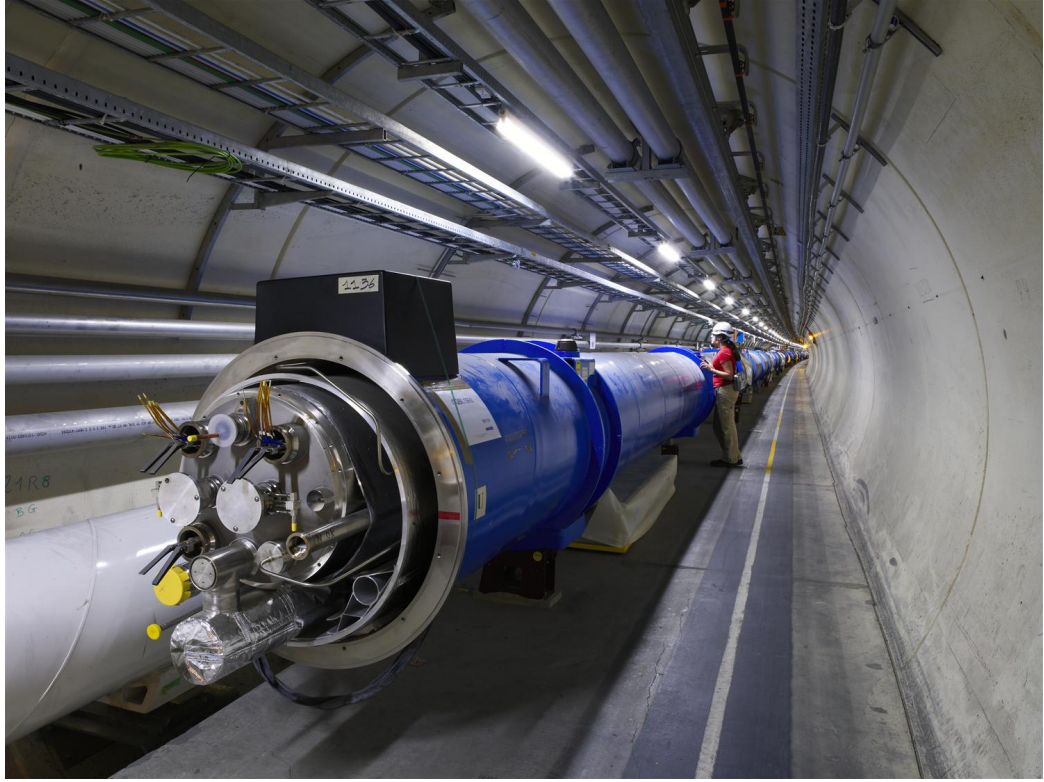


Figure 1.2: The Large Hadron Collider [20]

### 405 1.1.3 The ATLAS experiment

406 ATLAS (short for A Toroidal Lhc ApparatuS, figure 1.3) [] is a particle physics  
407 experiment at CERN. Its purpose is to verify current theories and search for new  
408 discoveries by observing and analysing high energy proton-proton collisions produced  
409 by the LHC. It is the biggest experiment at CERN by dimensions (45 m in length and  
410 26 m in height) and the number of people involved (more than 3000 physicists and  
411 engineers). The ATLAS detector consists of many detectors, each designed to measure  
412 a specific property of the particles and photons produced during the collision. The  
413 closest to the collision point is the Inner Detector (ID), which consists of several layers  
414 of highly spatially segmented semiconductor sensors. These can record the path of the  
415 individual particles and photons. In addition, a strong magnetic field of 2 T curves the  
416 paths of the charged particles, which in turn allows the ID to identify an individual  
417 particle's charge and momentum. The next two parts are the electromagnetic and tile  
418 calorimeter. These detectors weigh a few thousand tonnes and measure the energy of  
419 the particles that are stopping in the bulk. The only particles that make it through  
420 the calorimeters are muons. These are detected by the Muon Spectrometer, a set of  
421 large plates placed all around the inner layers. Last is the superconductive magnet,  
422 which provides the magnetic field through the whole of ATLAS except the ID, which  
423 already has its own magnets. To sum up, the Inner Detector measures the charge and  
424 momenta of the particles and photons, the calorimeters measure their energies, the

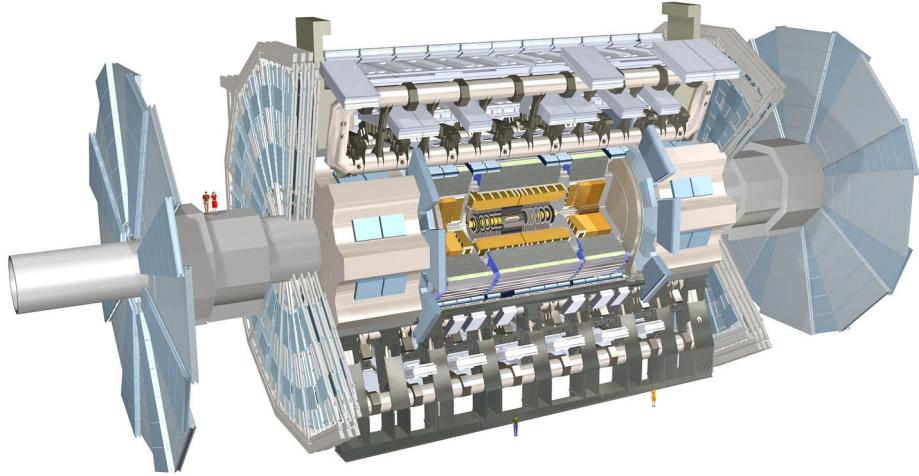


Figure 1.3: The ATLAS Experiment [38]

425 Muon Spectrometer measures muons and the magnets provide magnetic fields, which  
426 curve the trajectories of the charged particles, facilitating the charge and momentum  
427 measurements.

428 A complex Trigger and Data Acquisition system (TDAQ) is in place to distribute  
429 the clock signal, configure the detectors, trigger them and handle the output data.  
430 They are then stored at the CERN computer centre and distributed across the globe  
431 by means of the GRID – a cloud-like distributed data system.

432 The ATLAS detector has been designed to measure every collision taking place in  
433 its core. With 25 ns between collisions, this makes up 40 million collisions per second.  
434 In reality, the maximum achievable rate is about 300 kHz. The recorded collision  
435 is called an event. Every event holds information from all the detector channels  
436 within ATLAS. With  $\sim 10^6$  channels, an event size is approximately 10 MB. At the  
437 maximum achievable rate this means a data rate of up to 3 TB/s. Unfortunately  
438 no supercomputer existing today is capable of reading in and saving such a huge  
439 amount of data. This is where the trigger logic comes into play. It is programmed to  
440 decide in the order of tens of nanoseconds after an event whether this is a potentially  
441 interesting event or not. If so, it triggers the readout of the whole detector. This way,  
442 the recorded event rate is reduced from 300 kHz to  $\sim 500$  Hz, which is already within  
443 the limits of the computing centre's capabilities.

#### 444 1.1.4 Atominsttitut, Vienna

445 Atominsttitut (ATI) [2], an institute for atomic and subatomic physics, was estab-  
446 lished in 1958 in Vienna as an inter-university institute. It currently houses around

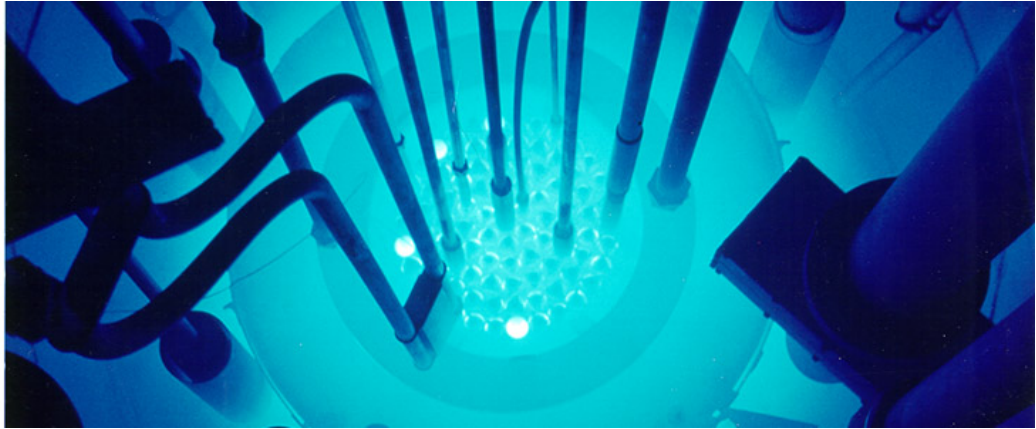


Figure 1.4: The TRIGA MARK II neutron reactor [15]

<sup>447</sup> 200 people involved in a broad range of research fields: quantum, particle, neutron,  
<sup>448</sup> nuclear, radiation and reactor physics, quantum optics etc. Its central facility is a  
<sup>449</sup> TRIGA MARK II neutron reactor (described in detail below).

<sup>450</sup> As of 2002 the ATI is part of the University of Technology in Vienna.

<sup>451</sup> **TRIGA MARK II neutron reactor** [12] is a reactor of a swimming-pool type  
<sup>452</sup> used for training, research and isotope production. It is one of 40 such reactors  
<sup>453</sup> worldwide, produced by an californian company General Atomic in the early 60's. It  
<sup>454</sup> is capable of continuous operation at a maximum output power of 250 kW. The reactor  
<sup>455</sup> core consists of 3 kg of 20 % enriched uranium ( $^{235}\text{U}$ ). The fuel moderator rods are  
<sup>456</sup> mostly made up of zirconium with low percentage of hydrogen and uranium. Both the  
<sup>457</sup> core and the rods are immersed in a pool of water as shown in figure 1.4 for the purpose  
<sup>458</sup> of cooling and radiation protection. The surrounding concrete walls are 2 m wide  
<sup>459</sup> with an added graphite layer for improved shielding. Four main experimental beam  
<sup>460</sup> holes are placed radially through the walls. All exits are heavily shielded to prevent  
<sup>461</sup> radiation damage to people, but still leaving enough space to set up experiments.  
<sup>462</sup> Apart from the beam holes, there are several other exits and components, e.g. a  
<sup>463</sup> thermal column for generation of thermal (low energetic) neutrons.

### <sup>464</sup> 1.1.5 n-ToF

<sup>465</sup> n-ToF (or neutron time-of-flight) [9] is a scientific collaboration with the aim of studying  
<sup>466</sup> neutron-nucleus interactions. Over 30 institutes and universities are currently  
<sup>467</sup> active members of this collaboration, among them Atominstitut in Vienna. n-ToF  
<sup>468</sup> is also a facility at CERN where the experiments are carried out in a 200 m long  
<sup>469</sup> experimental area. The knowledge stemming from the experimental results can then  
<sup>470</sup> be applied in various fields ranging from nuclear technology and cancer therapy to  
<sup>471</sup> astrophysics.

<sup>472</sup> A pulsed beam of highly energetic protons (20 GeV/c) is produced by the Proton  
<sup>473</sup> Synchrotron (PS) and aimed at a fixed lead spallation target. Each proton hitting

## 1.2. PARTICLE DETECTORS

---

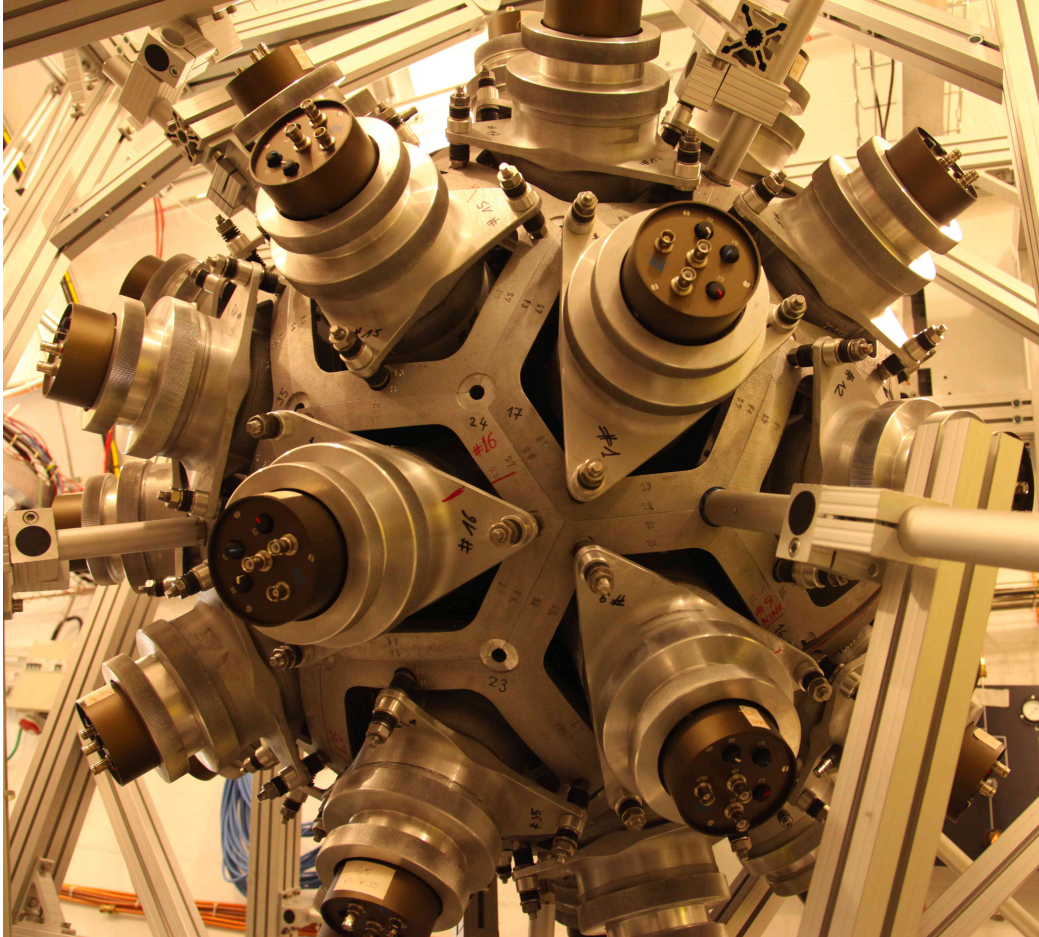


Figure 1.5: The calorimeter in the n-ToF area [19]

474 the target produces around 300 neutrons of various energies. Initially highly energetic  
475 neutrons are slowed down by the target and by a slab of water placed behind it. This  
476 broadens their energy spectrum, which then ranges from meV (thermal neutrons) to  
477 GeV (fast neutrons). The neutrons are then collimated and sent through a 185 m  
478 long evacuated pipe to the experimental area, where they are made to collide with  
479 another target or a sample. The radiation resulting from the collisions is detected by  
480 a set of dedicated detectors around the interaction point (seen in figure 1.5). Having  
481 different energies, neutrons travel with different speeds, highly energetic ones reaching  
482 the target faster than those with low energies. Analysis of the collisions with a precise  
483 timing allows us to determine the interaction probability with sample material as a  
484 function of incident neutron energy.

## 485 1.2 Particle detectors

486 Particle detectors, or radiation detectors, have first come into use at the end of the  
487 19th century. At that time Wilhelm Röntgen used a photographic plate onto which

he shone X-rays. Soon after, in 1912, Victor F. Hess discovered cosmic rays during a balloon flight. This paved the way for development of particle detectors. A cloud chamber was designed – a chamber filled with a supersaturated vapour of water or alcohol. If a highly energetic particle traversed the chamber, the mixture ionised, creating condensation nuclei. These traces were visible and were photographed. All the subsequent particle detectors relied on the same principle of interaction between the particles – ionisation. The bubble chamber invented in 1952 used a superheated transparent liquid – a liquid heated just below its boiling point. A particle ionised the liquid, forming microscopic bubbles along its trajectory. Then followed the spark chamber and the wire chamber where the particle ionised the gas, causing a spark between two parallel plates at a high potential difference. These are nowadays used in museums as showcases. Next were ionisation chambers, which measured the induced current of the free ionised charges moving in an externally applied electric field. Finally in the 1960s, semiconductor detectors were introduced. Their principle of operation is similar to that of an ionisation chamber, with the difference that a semiconductive material is used as an ionisation medium instead of gas. Every technology has its advantages and disadvantages. Nowadays an ensemble of several types of detectors is used as a single detector system. There are many considerations that need to be taken into account when designing such a system: detector geometry, segmentation, event rate, efficiency, readout, support structures, cabling, cooling, cost etc.

On large, particle detectors can be divided in two groups: tracking detectors and calorimeters. The former are designed to measure trajectories (momentum) of particles and photons with a minimal impact on their flight path or energy. They must be built with a high spatial resolution and lightweight. Typically they are semiconductor detectors. The calorimeters, on the other hand, measure the energy of the particles/photons by stopping them. This means they need to be heavy and dense. A typical physics experiment nowadays would consist of a tracking detector enclosed by a calorimeter. This way both the momentum and energy are derived, measuring energy, charge and trajectory of every particle/photon.

### 1.2.1 Semiconductor detectors

Semiconductor particle detectors are devices that use a semiconductor for detecting radiation. They work on the principle of an ionisation chamber. An incident particle or a photon ionises the atoms in the crystal lattice. The freed charges start drifting in an externally applied electric field, inducing current on the electrodes. The charges are freed if the deposited energy is higher than the energy band gap. There are many semiconductor materials currently existing, each with a different band gap. Germanium (Ge), for instance, has a band gap of 0.67 eV, which means that most of the electrons at the room temperature will already be in an excited state. Diamond's 5.5 eV band gap, on the other hand, is too high for the visible light to excite the electrons. Silicon with an energy gap of 1.12 eV has been the material of choice for the

## 1.2. PARTICLE DETECTORS

---

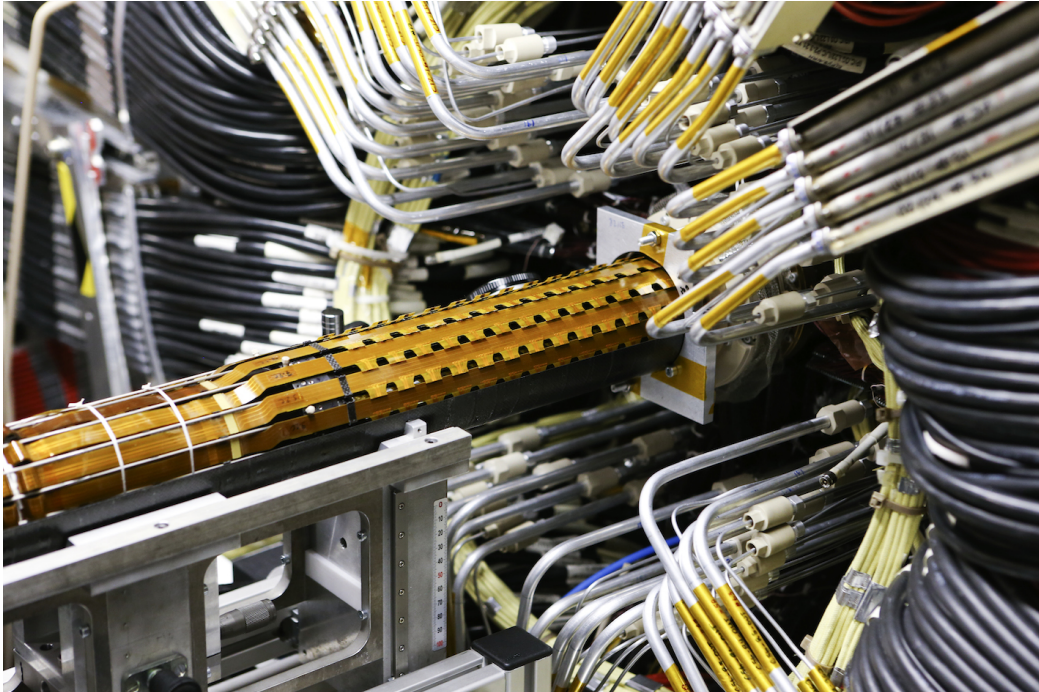


Figure 1.6: The Insertable B-Layer – a silicon particle tracker installed in the ATLAS experiment in 2014 [34]

529 majority of semiconductor applications, including radiation detectors. Semiconductor  
530 detectors are most widely used for tracking applications, like the Insertable B-Layer  
531 (see figure 1.6) [39], which was installed in ATLAS Experiment in 2014. They can  
532 be produced into light and thin sensors, they have a fast signal response, they are  
533 highly efficient and highly resistant to radiation damage. They also allow for a fine  
534 spatial segmentation to increase the tracking resolution. Semiconductor sensors come  
535 in several configurations. The simplest type is a pad – a single plate measuring  
536  $25 \text{ mm}^2$ . Pads are used for particle counting and radiation monitoring. Next is a  
537 strip detector, a more finely segmented detector made out of long parallel sensing  
538 areas or strips. Each strip has its own signal line for readout. Usually the strip  
539 detectors are used in pairs – one detector is placed on top of the other at a  $90^\circ$  angle  
540 to increase spatial resolution in both axes. The third and the most finely segmented  
541 is a pixel detector, consisting of a 2D array of independent sensing areas. In tracking  
542 applications, pixel detectors are used where the detection resolution is the highest.  
543 Due to their high production cost and a high number of signal channels, they can  
544 only cover limited areas. Strip detectors are cheaper to produce and can be used to  
545 cover larger areas in several consecutive layers.

### 546 1.2.2 Diamond sensors

547 Diamond has been known for over two millennia, valued for its mechanical properties  
548 and its appearance. When we learnt how to synthesise it, diamond found its way to

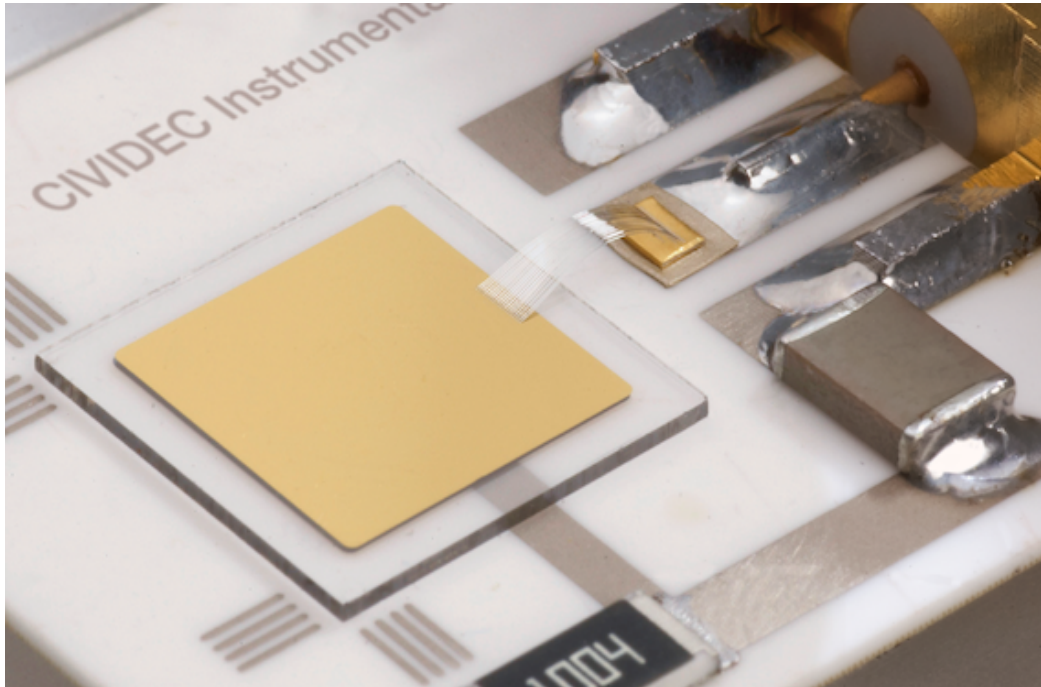


Figure 1.7: A pCVD diamond pad detector [23]

549 a broad range of industries which exploited its optical and electrical properties. The  
550 discovery of the Chemical Vapour Deposition (described below) as a new synthesis  
551 process gave rise to a range of new applications. From being used on machines  
552 for drilling tunnels it found its way to electronics, high-power switching devices,  
553 electrochemical systems, radiation sensors, quantum computing etc. Recently it was  
554 found that it also exhibit superconductivity. This thesis focuses on the use of diamond  
555 for radiation detection. Compared to a natural diamond, a detector-grade CVD  
556 diamond has almost no impurities (foreign atoms like nitrogen or boron). The carbon  
557 lattice is very uniform, which improves its electrical properties. It is an almost perfect  
558 insulator, but behaves as a semiconductor under certain conditions. Compared to  
559 silicon, the most widely used semiconductor material for radiation detection, it has  
560 many advantages, which are described in detail in chapter 2. Figure 1.7 shows a  
561 diamond pad detector produced by CIVIDEC Instrumentation GmbH.

562 **Chemical vapour deposition** (CVD) [] is a process where a material is deposited  
563 from a gas onto a substrate, involving chemical reactions. It is often carried out un-  
564 der high pressure and high temperatures. It takes place in enclosed chambers called  
565 furnaces with careful regulation of the temperature, pressure and gas mixture. Syn-  
566 thetic diamond is grown at 700–900 °C with a mixture of hydrogen and methane  
567 gas. At this temperature the molecules dissociate into carbon and hydrogen atoms.  
568 The carbon atoms are the building blocks and are deposited on the surface of the  
569 substrate. However, they would rather form graphitic bonds as they are more stable  
570 than diamond bonds. Nevertheless, with high pressure, high temperature and with  
571 added abrasive atomic hydrogen, the graphitic double bonds are broken up and con-

## 1.2. PARTICLE DETECTORS

---

572 vertyed into diamond bonds. The speed of the growth can be anywhere between 0.1  
573 and 10 micron per hour. The detector grade samples are grown at a rate of the order  
574 of 1 micron per hour. They can grow up to several millimetres in thickness. Their  
575 width, however, depends entirely on the substrate used. Diamond can be deposited  
576 on various materials: diamond, silicon, tungsten, quartz glass etc. The substrate  
577 material must be able to withstand the high temperatures during the CVD process.  
578 The diamond substrate does not need any surface pre-treatment. Carbon atoms form  
579 bonds with atoms in the existing crystal structure. This is the homoepitaxial growth  
580 where the newly deposited atoms retain the orientation of the structure in the sub-  
581 strate. Other non-diamond substrates, however, need to be pre-treated, usually by  
582 being polished using diamond powder. Some powder particles remain on the surface,  
583 acting as seeds for the growth of small crystals or grains. These grains grow and  
584 at some point merge with the adjacent ones, making up a compact material. The  
585 lower side is later polished away. These diamonds are called *polycrystalline* (pCVD)  
586 whereas those grown on a diamond substrate are *single crystal* (sCVD) diamonds.  
587 The area of the former can be large - up to  $0.5 \text{ m}^2$  or more compact  $15 \text{ cm}^2$  in the case  
588 of detector grade diamonds. The sCVD diamonds, on the other hand, can currently  
589 only measure up to  $1.5 \text{ cm}^2$ .

590

## Chapter 2

591

### Signal formation in diamond

592 This chapter describes the fundamentals of signal formation in a diamond sensor, as  
593 well as its use as a particle detector. This is described in section 2.1 where energy  
594 deposition and signal formation mechanism are explained. Then some examples of  
595 ionisation are shown. Later, some of the internal lattice defects that effect the signal  
596 are described. The final section contains the description of the remaining part of the  
597 signal chain – signal amplifiers, digitisers and devices for signal processing. Noise  
598 contributions are discussed at every stage of the signal chain.

599 There are many types of radiation sensors existing, but in this chapter we will  
600 focus on semiconductors, in particular on diamond sensors. Diamond is a good insu-  
601 lator, but behaves as a semiconductor in certain cases. In fact, the main principle of  
602 operation is the same for diamond, silicon and other semiconducting materials – ion-  
603 isation. An incident highly energetic charged particle ionises the atoms in the lattice,  
604 freeing electrons and holes, which then drift towards positively and negatively charged  
605 electrodes, inducing an electrical signal. A sensor converts the energy deposited by a  
606 particle or a photon to an electrical signal.

607 Silicon is currently considered as the industry standard for particle detection.  
608 However, there are some disadvantages of using silicon instead of diamond, due to  
609 significant differences in the material properties. In particular, the properties of silicon  
610 change significantly with radiation. For instance, the leakage current increases, which  
611 in turn increases shot noise and can lead to a thermal runaway. In addition, due to  
612 induced lattice defects, which act as charge traps, its charge collection efficiency starts  
613 dropping quickly. Both are true for diamond as well, but on a much smaller scale.

614 Table 5.2 compares the properties of diamond and silicon. Some of these values  
615 will be revisited and used in the course of this thesis.

Property	Diamond	Silicon
Band gap energy $E_g$ (eV)	5.5	1.12
Electron mobility $\mu_e$ ( $\text{cm}^2 \text{ V}^{-1} \text{ s}^{-1}$ )	1800	1350
Hole mobility $\mu_h$ ( $\text{cm}^2 \text{ V}^{-1} \text{ s}^{-1}$ )	1200	450
Breakdown field ( $\text{V cm}^{-1}$ )	$10^7$	$3 \times 10^5$
Resistivity ( $\Omega \text{ cm}$ )	$> 10^{11}$	$2.3 \times 10^5$
Intrinsic carrier density ( $\text{cm}^{-3}$ )	$< 10^3$	$1.5 \times 10^{10}$
Mass density ( $\text{g cm}^{-3}$ )	3.52	2.33
Atomic charge	6	14
Dielectric constant $\epsilon$	5.7	11.9
Displacement energy (eV/atom)	43	13 – 20
Energy to create an e-h pair (eV)	13	3.6
Radiation length (cm)	12.2	9.6
Avg. signal created/ $\mu\text{m}$ (e)	36	89

617 Table 2.1: Comparison diamond – silicon []

 618 

## 2.1 Principles of signal formation in semiconduc- 619 tors

 620 There are several ways the particles can interact with the sensor: via bremsstrahlung [],  
 621 elastic or inelastic scattering (e-h pair production). Bremsstrahlung is radiation cre-  
 622 ated when a particle is deflected from its original path due to attraction of the core of  
 623 an atom. This is in principle an unwanted effect in semiconductors as it decreases the  
 624 spatial resolution of the sensor. Elastic scattering is deflection of the particle's tra-  
 625 jectory without energy loss. Inelastic scattering is the interaction through which the  
 626 atom is ionised and an electron-hole pair is created. All these effects are competing  
 627 and are dependent on the particle's mass, momentum etc.

 628 Semiconductors are materials that are conductive only under specific  
 629 conditions. They can be made up of atoms with four electrons in their valence band  
 630 (e.g. silicon–Si, carbon–C or germanium–Ge) or as combinations of two or more  
 631 different materials (e.g. gallium arsenide–GaAs). The atoms in the lattice form  
 632 valence bonds with adjacent atoms, making solid crystal structures. These bonds  
 633 can break up if sufficient external energy is applied. The electron that was forming  
 634 the bond is kicked out, leaving behind a positively charged ion with a vacancy in its  
 635 valence band (see figure 2.1a). A free electron-hole pair is thus created. The free  
 636 electron travels through the crystal until it is caught by another hole. Similarly, the  
 637 hole also “travels” through the material. Its positive charge attracts a bound electron  
 638 in the vicinity, which breaks from the current bond and moves to the vacancy, leaving  
 639 a new hole behind. The process continues, making it look like the vacancy – the hole  
 640 – is traveling through the material.

 641 The electrons need to absorb a certain energy to get kicked out of the atomic  
 642 bond – to get ionised. The minimal energy required to excite (ionise) an electron in  
 643 a semiconductor is equal to the energy gap  $E_g$ . Typical widths of the forbidden gap  
 644 are 0.7 eV in Ge, 1.12 eV in Si, 1.4 eV in GaAs and 5.5 eV in Di. Due to the small

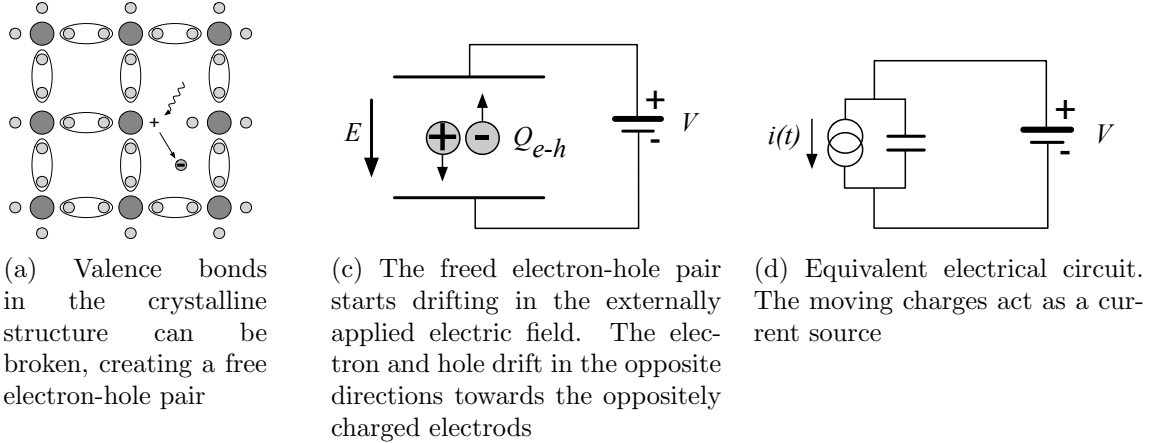


Figure 2.1: In the equivalent electrical circuit diagram, electron-hole creation and drift can be modelled as a current source with a capacitor in parallel

band gap in semiconductors some electrons already occupy the conduction band at room temperature (RT). The intrinsic carrier concentration  $n_i$  in semiconductors is given as

$$n_i = T^{3/2} \cdot \exp\left(-\frac{E_g}{2kT}\right) \quad (2.1)$$

wherein  $k = 1.381 \times 10^{-23} \text{ m}^2 \text{ kg s}^{-2} \text{ K}^{-1}$  is the Boltzmann constant and  $T$  is the temperature.

If an external electric field is applied to the crystalline structure, the free electrons and holes drift toward the positive and negative potential, respectively (see figure 2.1c). While drifting, the charges couple with the electrodes, inducing current in the circuit, which is explained by the Shockley–Ramo theorem (see subsection below). The charges recombine upon reaching the electrodes.

### Energy deposition of $\alpha$ radiation and heavy ions

**Energy deposition of  $\beta$  and  $\gamma$  radiation** The mean energy loss of a particle traversing the detector with respect to its momentum is given with the the Bethe-Bloch equation []:

$$-\left\langle \frac{dE}{dx} \right\rangle = \frac{4\pi}{m_e c^2} \cdot \frac{n z^2}{\beta^2} \cdot \left( \frac{e^2}{4\pi\epsilon_0} \right)^2 \cdot \left[ \ln \left( \frac{2m_e c^2 \beta^2}{I \cdot (1 - \beta^2)} \right) - \beta^2 \right] \quad (2.2)$$

The resulting function for a muon (a heavy electron) is shown in figure 2.2. At the momentum of around 300 MeV/c the particle deposits the lowest amount of energy. That is called a minimum ionising particle or a MIP.

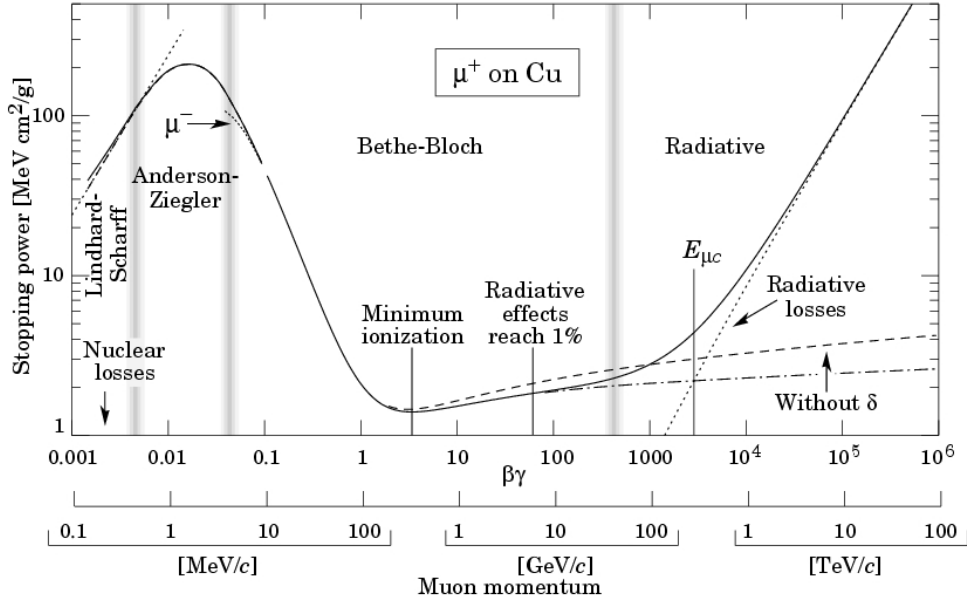


Figure 2.2: Stopping power for muons according to the Bethe-Bloch formula []

### 662 2.1.1 Signal induction by moving charges

663 The book [17] gives a simple introduction to understanding signal induction in a  
 664 conducting plane by a point-like charge. The idea behind it lies in the coupling of  
 665 the charge with the electrode. The electrode can be in this case modelled as an  
 666 infinite conducting plane. When the point charge  $q$  is created (e.g. an electron-hole  
 667 pair created via ionisation), its electrostatic field lines immediately couple with the  
 668 electrode, as seen in figure 2.3a. The electric field on the metal surface due to a  
 669 point-like charge  $q$  at the distance  $z_0$  equals

$$E_z(x, y) = \frac{q z_0}{2\pi\epsilon_0(x^2 + y^2 + z_0^2)^{\frac{3}{2}}} \quad E_y = E_z = 0. \quad (2.3)$$

670 A mirror charge appears on the conducting plane, with a charge density distribution

$$\sigma(x, y) = \epsilon_0 E_z(x, y) = \frac{q z_0}{2\pi(x^2 + y^2 + z_0^2)^{\frac{3}{2}}}. \quad (2.4)$$

671 The charge density integrated over the whole plane gives the mirror charge  $Q$ , which  
 672 has the opposite value of the point charge  $q$ :

$$Q = \int_{-\infty}^{\infty} \int_{-\infty}^{\infty} \sigma(x, y) dx dy = -q. \quad (2.5)$$

673 Now we segment the plane into infinitely long strips with a width  $w$  whereby each  
 674 of the strips is grounded (figure 2.3c). With the charge density distribution 2.4, the

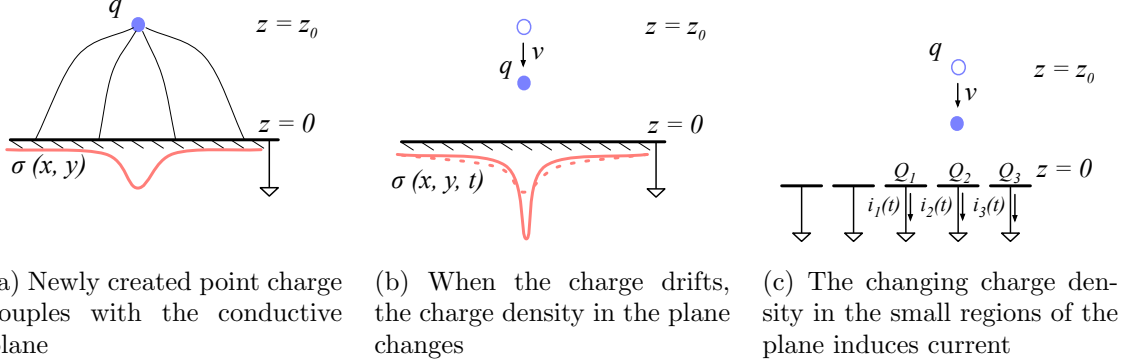


Figure 2.3: A point-like charge inducing current in a conductive plane

675 resulting mirror charge on a single strip  $Q_2$  directly below the point charge ( $x =$   
 676  $0, y = 0$ ) will be equal to

$$Q_2(z_0) = \int_{-\infty}^{\infty} \int_{-w/2}^{w/2} \sigma(x, y) dx dy = -\frac{2q}{\pi} \arctan\left(\frac{w}{2z_0}\right) \quad (2.6)$$

677 If the charge starts moving towards the conducting plane, the mirror charge density  
 678 distribution also changes (see figure 2.3b). This results in the  $Q_2[z_0(t)]$  to change  
 679 with time, inducing an electric current  $i_n(t)$ :

$$i_n(t) = -\frac{d}{dt} Q_2[z_0(t)] = -\frac{\partial Q_2[z_0(t)]}{\partial z_0} \frac{\partial z_0(t)}{\partial t} = \frac{4qw}{\pi[4z_0(t)^2 + w^2]} v. \quad (2.7)$$

680 The movement of the point-like charge therefore induces current in the conducting  
 681 plane. The induced current is linearly dependent on the velocity of the point-like  
 682 charge.

683 W. Shockley [42] and S. Ramo [40] independently proposed a theory which explains  
 684 how a moving point charge induces current in a conductor. The Shockley-Ramo  
 685 theorem can therefore be used to calculate the instantaneous electric current induced  
 686 by the charge carrier or a group of charge carriers. It can be used for any number of  
 687 electrodes. It states that the current  $I_n^{\text{ind}}(t)$  induced on the grounded electrode  $n$  by  
 688 a point charge  $q$  moving along a trajectory  $\mathbf{x}(t)$  equals

$$I_n^{\text{ind}}(t) = -\frac{dQ_n(t)}{dt} = -\frac{q}{V_w} \nabla \Psi_n[\mathbf{x}(t)] v(t) = -\frac{q}{V_w} \mathbf{E}_n[\mathbf{x}(t)] v(t), \quad (2.8)$$

689 where  $\mathbf{E}_n(\mathbf{x})$  is the electric field in the case where the charge  $q$  is removed, electrode  $n$   
 690 is set to voltage  $V_w = 1$  and all other electrodes are grounded.  $\mathbf{E}_n(\mathbf{x})$  is also called the  
 691 *weighting field* of electrode  $n$  and is defined as the spatial differential of the *weighting*  
 692 *potential*:  $\mathbf{E}_n(\mathbf{x}) = \nabla \Psi_n(\mathbf{x})$ . In the case of two parallel electrodes, the weighting field  
 693 is  $E_w = -\frac{d\Psi}{dx} = -1/d$ , where  $d$  is the distance between the electrodes. The resulting  
 694 induced current is therefore

$$i(t) = \frac{q}{d} v_{\text{drift}}(x, t), \quad (2.9)$$

## 2.1. PRINCIPLES OF SIGNAL FORMATION IN SEMICONDUCTORS

---

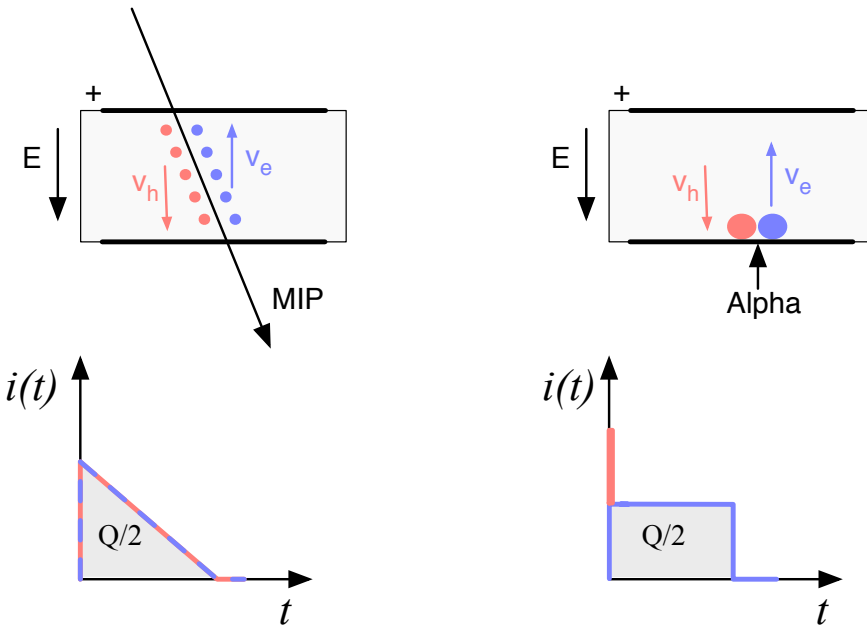


Figure 2.4: Charge carrier drift in diamond for  $\beta/\gamma$  and for  $\alpha$  particles

695 whereby  $v_{\text{drift}}$  is the drift velocity of the point-like charge and  $d$  is the distance between  
 696 the electrodes.

### 697 2.1.2 Radiation-induced electrical pulses

698 When a highly-energetic particle travels through the sensor, it interacts with atoms  
 699 in the lattice. It ionises the valence electrons, creating electron-hole (e-h) pairs on its  
 700 way. It can either deposit only a fraction of its energy and fly exit the sensor on the  
 701 other side or it can get stopped in the bulk, depositing all of its energy. A special  
 702 case is when it interacts with the core of the atom in the middle of the sensor via  
 703 a nuclear interaction. All these various types interactions produce different amounts  
 704 and different spatial distributions of e-h pairs. The induced electrical current will  
 705 therefore differ for different types of interaction. Two most frequent types are shown  
 706 in figure 2.4. The first diagram shows the interaction of a minimum ionising particle  
 707 (an electron or a proton) or in some cases a photon, if it is energetic enough. The  
 708 electrons and holes are created all along the trajectory of the particle and imme-  
 709 diately start drifting towards the positive and negative electrode, respectively. At  
 710 the beginning, all charges drift and contribute to the induced current. Those closest  
 711 to the electrodes have a very short drift path and recombine quickly, reducing the  
 712 induced current. Gradually all the charge carriers recombine. The resulting current  
 713 signal is a triangular pulse with a sharp rising edge and a linear falling edge. The  
 714 accumulated charge  $Q_s$  equals to the sum of the contributions of the positive and

negative charge carriers. The second type of interaction happens when the particle is stopped in the diamond close to the point of entry. Most of its energy is deposited in a small volume close to the electrode. A cloud of charge carriers is created and the charges with the shorter path to the electrode recombine almost instantly. The carriers of the opposite charge, however, start drifting through the sensor to the other electrode. In an ideal diamond sensor, their velocity is constant throughout the drift up until they recombine on the other side. The contribution of the first charge cloud is a peak with a short time. The cloud drifting through the sensor, on the other hand, induces a current signal with a flat top. The resulting signal has a shape of a rectangle, with a spike in the beginning. This spike is filtered out in a real device because it is too fast for the electronics existing currently. The accumulated charge  $Q_s$  is equal to a half of the deposited charge by the stopped particle.

The two aforementioned types of interactions have well defined signal responses. Nuclear interactions on the other hand yield various results. The resulting signal shape depends on the decay products of the interaction – they can be  $\alpha$ ,  $\beta$  or  $\gamma$  quanta, inducing a mixed shaped signal.

### 2.1.3 Signal charge fluctuations

Two of the important sensor characteristics are the magnitude of the signal and the fluctuations of the signal at a given absorbed energy. They determine the relative resolution  $\Delta E/E$ . For semiconductors the signal fluctuations are smaller than the simple statistical variance  $\sigma_Q = \sqrt{N_Q}$ , where  $N_Q$  is the number of released charge pairs (ratio between the total deposited energy  $E_0$  and the average energy deposition  $E_i$  required to produce an electron-hole pair). [] shows that the variance is  $\sigma_Q = \sqrt{F N_Q}$ , where  $F$  is the Fano factor [] (0.08 for diamond and 0.115 for silicon []). Thus, the variance of the signal charge is smaller than expected,  $\sigma_Q \approx 0.3\sqrt{N_Q}$ . The resulting intrinsic resolution of semiconductor detectors is

$$\Delta E_{FWHM} = 2.35\sqrt{FEE_i} \quad (2.10)$$

wherein  $E_i(Si) = 3.6$  eV and  $E_i(C) = 13$  eV. E.g., for an  $\alpha$  particle with energy  $E_\alpha = 5.486$  MeV the calculated resolution in diamond is equal to  $\Delta E_{FWHM} = 5.6$  keV. This defines the maximum achievable resolution for energy spectroscopy with semiconductors. Figure 2.5 shows the calculated energy resolution function for silicon and diamond.

## 2.2 Carrier transport in a diamond sensor

This section describes the carrier transport phenomena in diamond. This theory provides the basis for discussion about the measurements in chapter 3.

Free charge carriers in a semiconductor get thermally excited and scatter in random directions with a thermal velocity  $v_{th}$  []. Their integral movement due to thermal

## 2.2. CARRIER TRANSPORT IN A DIAMOND SENSOR

---

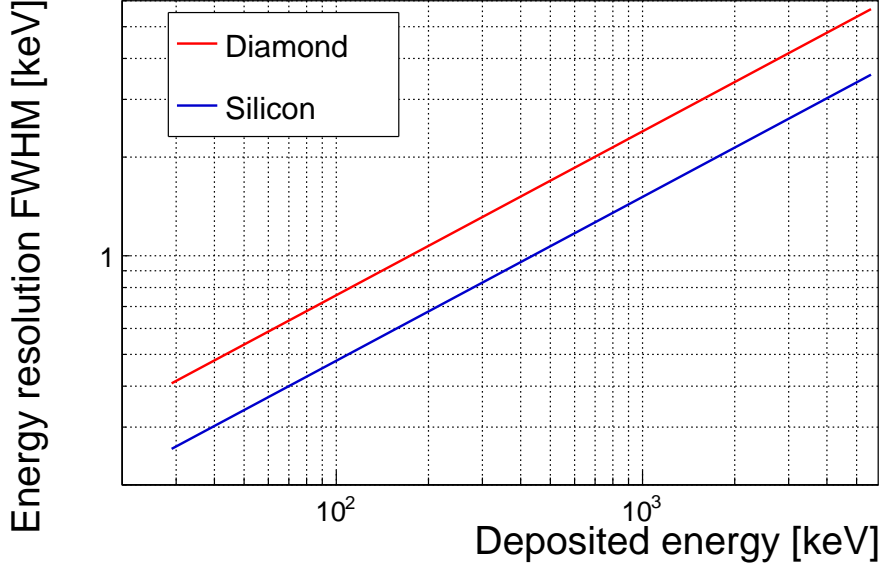


Figure 2.5: Calculated intrinsic energy resolution for silicon and diamond

excitation equals zero. Their transport is instead by means of drift and diffusion. Diffusion is caused by the concentration gradient. In its presence the carriers tend to scatter in the direction of the lower concentration. Drift on the other hand is caused by an externally applied electrical field. In that case the carriers move in parallel to the field lines. In a sensor with a high applied field the diffusion contribution is negligible.

**Diffusion** The concentration profile dissolves with time forming a Gaussian distribution with variance  $\sigma(t) = \sqrt{Dt}$ .

**Drift velocity and mobility** The charge carriers drift through the diamond bulk with a drift velocity  $v_{\text{drift}}(E)$ , which is proportional to the electric field  $E$  at low electric fields:  $v_{\text{drift}} = \mu E$ . The proportionality factor  $\mu$  is defined as the mobility in  $\text{cm}^2\text{V}^{-1}\text{s}^{-1}$ . For higher fields, however, the velocity saturates. The final equation for  $v_{\text{drift}}$  is therefore

$$v_{\text{drift}}(E) = \mu(E)E = \frac{\mu_0 E}{1 + \frac{\mu_0 E}{v_{\text{sat}}}} \quad (2.11)$$

where  $\mu_0$  is the low field mobility and  $v_{\text{sat}}$  is saturation velocity. The drift velocity can be retrieved experimentally via the transit time measured with the Transient Current Technique (TCT). This technique enables the measurement of transit time  $t_t$  of the carriers through the sensor with the thickness  $d$ .

$$v_{\text{drift}}(E) = \frac{d}{t_t(E)}. \quad (2.12)$$

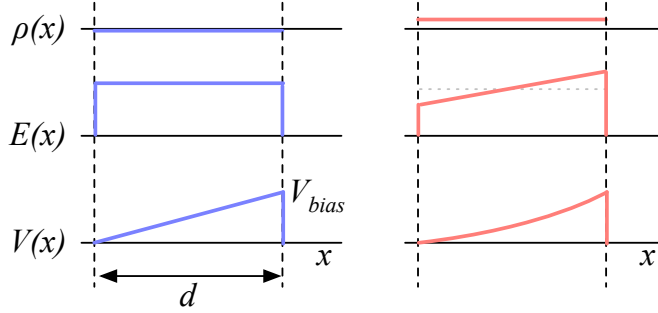


Figure 2.6: Introduction of space charge in the diamond bulk. The induced current signal is proportional to the effective electrical field.  $d$  is the thickness of the diamond sensor.

768 The velocities for holes and electrons usually differ. In diamond, the holes travel  
 769 30 % faster than electrons []. The measurements in chapter 3 empirically confirm this  
 770 statement.

771 **Velocity saturation** At higher drift velocities the carriers lose more energy to the  
 772 lattice. They induce increasingly more lattice vibrations (phonon transport) with  
 773 increased velocity. There is a velocity limit above which the carriers cannot reach –  
 774 velocity saturation. Thesis [] defines this velocity to be  $v_{\text{sat}}^e = v_{\text{sat}}^h = (14.23 \pm 0.12) \times$   
 775  $10^6$  cm/s for both positive and negative charge carriers.

776 **Space charge** Poisson's equation shows that

$$\frac{d^2\Phi(x)}{dx^2} = \frac{dE(x)}{dx} = \frac{\rho(x)}{\epsilon} \quad (2.13)$$

777 where  $\rho(x)$  is the space charge distribution,  $E$  is the electrical field and  $\Phi$  is the voltage  
 778 potential. In an ideal diamond, the externally applied high voltage potential on the  
 779 two electrodes decreases linearly through the bulk. The electrical field is therefore  
 780 constant throughout the sensor and the space charge distribution across it equals  
 781 0. However, in some cases space charge is introduced in the bulk, uniformly or non-  
 782 uniformly. It can do so by means of trapping of charge carriers in the non-uniformities  
 783 in the lattice or it can already be introduced during the production of the diamond  
 784 material. The space charge can be either permanent or changing – sometimes it is  
 785 possible to reduce it by means of priming. All in all, it is very important to reduce  
 786 it because it affects the shape of the electrical signal. Since the drift velocity of  
 787 the charge carriers is proportional to the electrical field, the charges change their  
 788 velocity while drifting through the space charge region. Figure 2.7 compares the  
 789 voltage potential, electrical field, space charge for an ideal sensor and for that with a  
 790 uniformly distributed positive space charge.

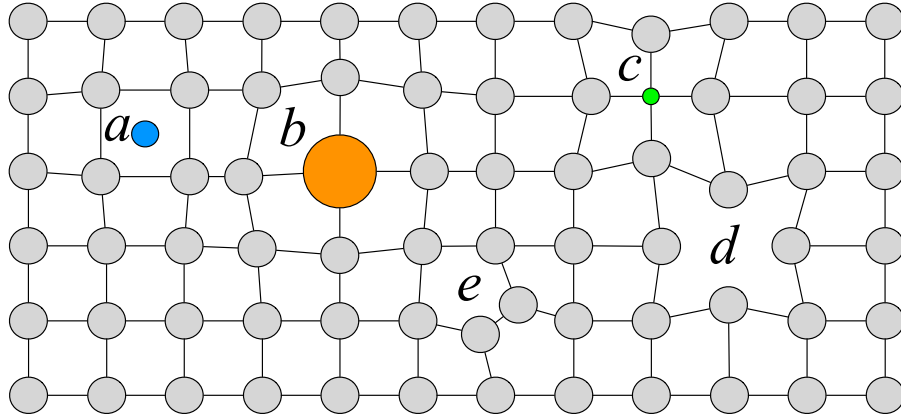


Figure 2.7: Introduction of impurities and non-uniformities into the crystal lattice due to radiation damage.

791 **Radiation damage** The diamond crystal lattice is very strong and uniform. However, when the highly energetic particles or photons impinge the diamond, they can 793 damage the crystal structure. Figure ?? shows several examples of the lattice damage:

- 794 a) foreign interstitial (e.g. H, Li),
- 795 b, c) foreign substitutional (e.g. N, P, B),
- 796 d) vacancy and
- 797 e) self interstitial.

798 These non-uniformities – traps – form new energy levels in the forbidden gap. The 799 drifting charge carriers are stopped by these traps, which in effect reduces the induced 800 current. The energy level of the trapped carrier is reduced from the conduction band 801 to the energy level of the trap. Different types of lattice damage have different energy 802 levels. The release time depends on the level (shallow, deep trap).

## 803 2.3 Electronics for signal processing

804 This section describes the electronics of a detector, starting with a description of 805 signal amplifiers and then discussing the digitisation and signal processing. All these 806 stages are necessary to extract information from the sensor. First, the signal has to be 807 amplified. Then it is digitised and finally processed in a specially designed processor 808 or a logic unit.

### 809 2.3.1 Signal preamplifiers

810 The signal charge generated in the sensor by a single highly energetic particle or 811 photon is of the order of fC. The induced current is ranging between  $10^{-8}$  A ( $\beta, \gamma$

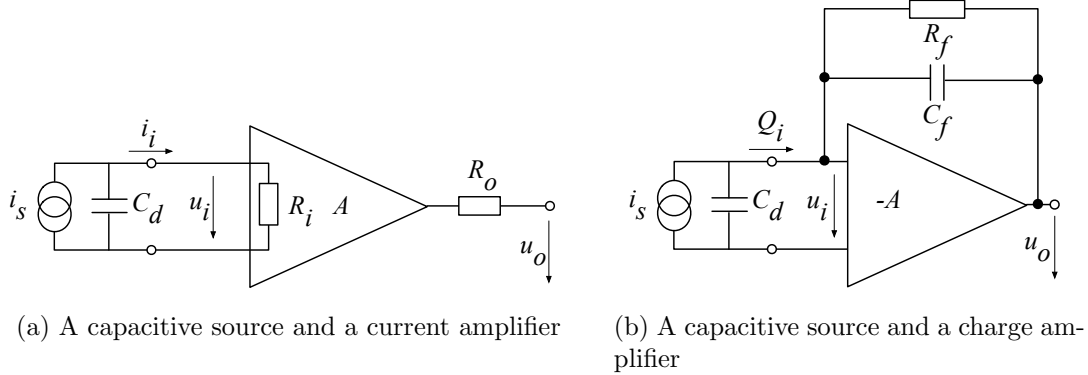


Figure 2.8: Simplified equivalent circuits of a current and charge amplifier

812 radiation) and  $3 \times 10^{-7}$  A ( $\alpha$  radiation). Signals as low as these have to be pre-  
 813 amplified before processing. Depending on the measurement, several types of signal  
 814 amplifiers can be used. The preamplifiers have to be designed carefully to minimise  
 815 electronic noise while maximising gain – thus maximising the signal-to-noise ratio  
 816 (SNR). In addition, they have to have a high bandwidth limit because the signals  
 817 from the diamond sensors are very short. A critical parameter is the total capaci-  
 818 tance, i.e. sensor capacitance and input capacitance of the preamplifier. The SNR  
 819 improves with a lower capacitance. Several types of amplifiers can be used, all of  
 820 which affect the measured pulse shape. They behave differently for resistive or ca-  
 821 pacitive sources. Given that semiconductors are capacitive sources, we will focus on  
 822 these. Two preamplifiers are used most commonly, a current and a charge amplifier.  
 823 Both are described below in detail.

### 824 2.3.1.1 Current-sensitive amplifier

825 Figure 2.8a shows the equivalent circuit of a capacitive source and a current amplifi-  
 826 er. An amplifier operates in current mode if the source has a low charge collection  
 827 time  $t_c$  with respect to the  $R_i C_d$  time constant of the circuit. In this case the sensor  
 828 capacitance discharges rapidly and the output current  $i_o$  is proportional to the in-  
 829 stantaneous current  $i_i$ . The amplifier is providing a voltage gain, so the output signal  
 830 voltage  $u_o$  is directly proportional to the input voltage  $u_i$ :

$$u_o(t) = A \cdot R_i \cdot i_s(t). \quad (2.14)$$

831 The detector capacitance  $C_{\text{det}}$  together with the input resistance of the amplifier  $R_i$   
 832 defines the time constant of the signal (see figure 2.9). The higher the  $C_{\text{det}}$  is, the  
 833 slower will be the response of the amplifier. For the case of the diamond sensor, which  
 834 has the capacitance of the order of 2 pF and the input resistance of 50  $\Omega$ , the resulting  
 835 time constant is  $\tau = 10^{-10}$  s. This yields the signal rise time  $t_r \sim 2.2\tau = 0.22$  ns.

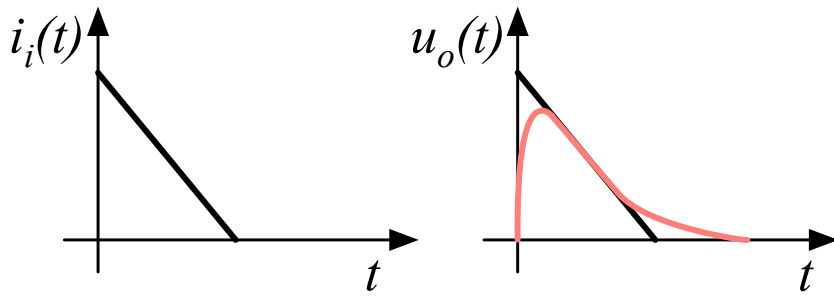


Figure 2.9: Input and output signal of the current amplifier

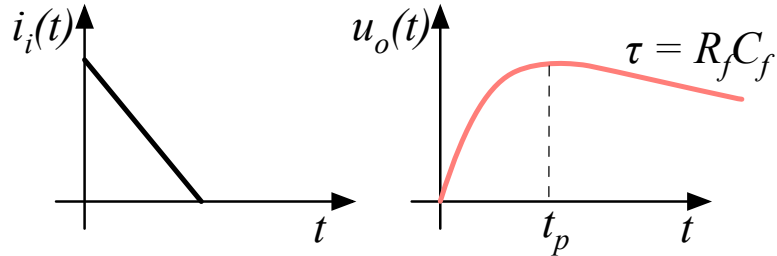


Figure 2.10: Input and output signal of the charge amplifier

### 836 2.3.1.2 Charge-sensitive amplifier

837 In order to measure integrated charge in the sensor, a feedback loop is added to the  
838 amplifier (see figure 2.8b). The feedback can be used to control the gain and input  
839 resistance, as well as to integrate the input signal. The charge amplifier is in principle  
840 an inverting voltage amplifier with a high input resistance.

841 In an ideal amplifier the output voltage  $u_o$  equals  $-Au_i$ . Therefore the voltage  
842 difference across the capacitor  $C_f$  is  $u_f = (A + 1)u_i$  and the charge deposited on the  
843 capacitor is  $Q_f = C_f u_f = C_f(A + 1)u_i$ . Since no current can flow into the amplifier,  
844 all of the signal current must charge up the feedback capacitance, so  $Q_f = Q_i$ .

845 In reality, however, charge-sensitive amplifiers respond much slower than is the  
846 duration of the current pulse from the sensor. In addition, a resistor is added to the  
847 feedback line in parallel to the capacitor. The resistor and capacitor define the decay  
848 time constant of the pulse (see figure 2.10). This is necessary to return the signal to  
849 its initial state and ready for a new measurement.

850 **2.3.1.3 Analogue electronic noise**

851 Electronic noise determines the ability of a system to distinguish signal levels. The  
 852 analogue signal contains a lot of information, which can quickly be erased or altered  
 853 if the signal properties change. It is therefore instrumental to understand the noise  
 854 contributions to the signal to qualify the information it carries. There are several  
 855 noise contributions, of which the important ones are listed below. The thermal noise  
 856 is the dominant noise contribution in the use case for diamond detector signal ampli-  
 857 fication and therefore defines the limitations of the detector system. Thermal noise  
 858 or Johnson–Nyquist [] noise is generated by the random thermal motion of charge  
 859 carriers in the conductor. The frequency range of the thermal noise is from 0 to  
 860  $\infty$  with a more or less uniform distribution. Therefore this is nearly a white noise.  
 861 The resulting signal amplitude has a Gaussian distribution. The RMS of the noise  
 862 amplitude is defined as

$$u_{\text{RMS}} = \sqrt{4k_B RT \Delta f} \quad (2.15)$$

863 where  $k_B$  is the Boltzmann constant,  $R$  is the resistance of the conductor,  $T$  its  
 864 temperature and  $\Delta f$  the frequency range. This equation shows that it is possible to  
 865 reduce the noise RMS by either (1) reducing the frequency range, (2) reducing the  
 866 resistance of the conductor or (3) cooling the conductor.

867 Contributions of shot noise, flicker noise and burst noise and other types are not  
 868 significant relative to the thermal noise. However, the contributions of external factors  
 869 can severely deteriorate the signal. This means the noise produced by capacitive or  
 870 inductive coupling with an external source, which causes interference in the signal.  
 871 These effects can be reduced by shielding the electronics and avoiding ground loops.

872 **2.3.2 Analogue-to-digital converters**

873 An analogue-to-digital converter (ADC) is a device that converts the analogue elec-  
 874 trical signal on the input to its digital representation - a series of digital values. This  
 875 involves a quantisation – *sampling* of the signal at a defined sampling period, resulting  
 876 in a sequence of samples at a discrete time period and with discrete amplitude values.  
 877 The resolution of the ADC is the number of output levels the ADC can quantise to  
 878 and is expressed in bits. For instance, an ADC with a resolution  $n = 8$  bit will have  
 879 the dynamic range  $N = 2^n = 256$  steps. The resulting voltage resolution  $Q_{\text{ADC}}$  at  
 880 the input voltage range of  $V_{\text{ADC}} = \pm 50$  mV is then equal to

$$Q_{\text{ADC}} = \frac{V_{\text{ADC}}}{2^n} = \frac{100 \text{ mV}}{2^8 \text{ steps}} = 0.39 \text{ mV/step.} \quad (2.16)$$

881 With a sampling period of  $t_s = 1$  ns this will produce the sampling rate of  $f_s = 1$  GSPS  
 882 (gigasample per second).

883 **Quantisation error and quantisation noise** (or a round-off error) is a contribu-  
 884 tion to the overall measurement error due to digitisation (rounding). It is defined  
 885 as a difference between the actual analog value and a digitised representation of this

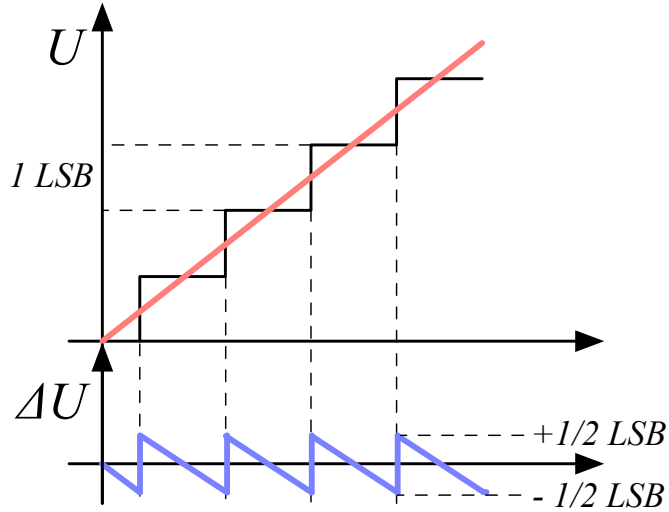


Figure 2.11: Input signal digitisation and quantisation error

886 value. The error is defined by the least significant bit (LSB), as seen in figure 2.11.  
 887 Typically, the input signal amplitude is much larger than than the voltage resolution.  
 888 Therefore the quantisation error is not directly correlated with the signal and has an  
 889 approximately uniform distribution []:

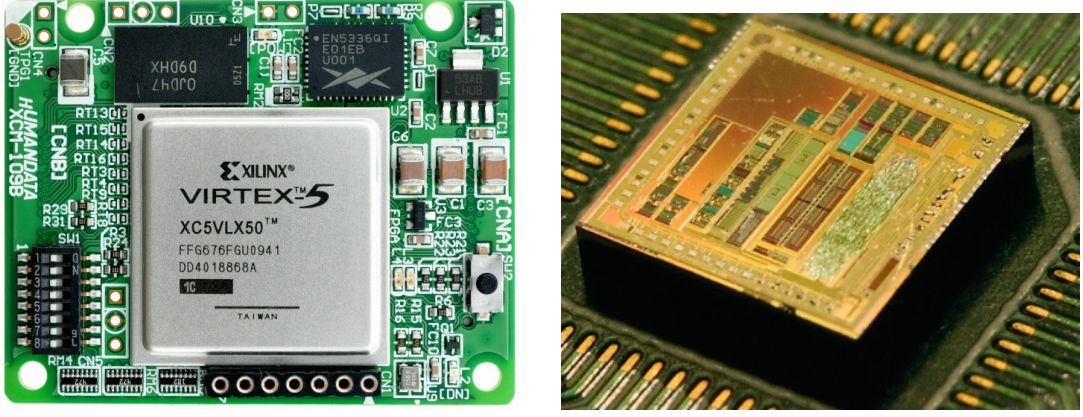
$$\Delta Q_{\text{ADC}} = \frac{1}{\sqrt{12}} \text{ LSB} \sim 0.289 \text{ LSB}. \quad (2.17)$$

890 For the example above the quantisation error will be  $\Delta Q_{\text{ADC}} = 0.289 \cdot 0.39 \text{ mV} = 0.11 \text{ mV}$ .  
 891 The error depends strongly on the linearity of the ADC, but this will not be discussed  
 892 in this document as the devices used have ADCs with a linear response.

### 893 2.3.3 Digital signal processing

894 The digitised signal can be processed to extract useful information. Therefore after  
 895 the signal amplification and digitisation the signal is routed in a device which handles  
 896 the analysis. The signal can either be processed immediately (in real time) or it can  
 897 be saved to a data storage for analysis at a later stage (offline). The devices carrying  
 898 out the processing can be multipurpose (e.g. Field programmable gate arrays) or  
 899 dedicated (e.g. application-specific integrated circuits). Each of the two has its  
 900 advantages and disadvantages, which are listed below.

901 **Field programmable gate array (FPGA)** is an integrated circuit designed to be  
 902 reprogrammable and reconfigured after manufacturing. It consists of a set of logic  
 903 gates that can be interconnected in numerous combinations to carry out a logic op-  
 904 eration. Many such logic operations can take place in parallel, making the FPGA a



(a) Xilinx Virtex 5 FPGA [13]

(b) ASIC [1]

Figure 2.12: An example of an FPGA and an ASIC chip

powerful tool for signal processing. FPGAs are often used during system development or in systems in which the requirements might change with time. They can be reprogrammed in the order of seconds. In addition, the logic design only needs minor changes when migrating to a newer version of the FPGA chip of the same vendor. They also offer faster time-to-market with comparison to application-specific solutions, which have to be developed. On the other hand, the price per part can be significantly higher than for the application-specific solutions. Also, their other major disadvantages are a high power consumption and a relatively low speed. However, today's solutions are capable of clock speeds of the order of 500 MHz. Together with the integrated digital signal processing blocks, embedded processors and other modules, they are already very powerful and versatile. All in all, FPGAs are a good choice for prototyping and limited production, for projects with a limited requirements for speed and complexity.

918 **Application-specific integrated circuit** (ASIC) is an integrated circuit designed  
919 for a specific use. The design cannot be modified after chip production, as compared  
920 to FPGAs. On the other hand, the ASICs can be optimised to perform a required  
921 operation at a high speed and at a low power consumption. In addition, due to the  
922 specific design the size of the chip can be much smaller. ASICs can be designed  
923 as hybrid chips, containing both a digital and an analog part. To update the chip,  
924 the design has to be submitted to a foundry, which produces the new chips with a  
925 turnover time of 4–6 weeks. The costs of a submission start at \$ 50 000, but the  
926 price per part can be reduced significantly with a high volume. To sum up, ASICs  
927 are used for high volume designs with well defined requirements where some stringent  
928 constraints in terms of power consumption and speed have to be met.

<sub>929</sub> **Chapter 3**

<sub>930</sub> **Experimental results**

<sub>931</sub> ***Diamond irradiation study***

<sub>932</sub> This chapter contains the measurement results of data taken with diamond sensors.  
<sub>933</sub> First the measurement setup is described (section 3.1). Then the measured particle  
<sub>934</sub> spectra are shown in 3.2. This is followed by a study of effects of irradiation damage  
<sub>935</sub> on the electrical signal of the diamond detector and its lifetime. The last section  
<sub>936</sub> shows the results of the measurements of irradiated diamond samples at cryogenic  
<sub>937</sub> temperatures. The aim of these studies is to find the operational limitations of dia-  
<sub>938</sub> mond detectors for spectroscopy and tracking applications. The studies compare the  
<sub>939</sub> experimentally acquired data with the theory from the previous chapter and define  
<sub>940</sub> limitations of the diamond detectors in terms of noise, radiation and temperature.

<sub>941</sub> Diamond sensors are mainly used for two types of measurements: particle counting  
<sub>942</sub> and spectroscopy. The first type of measurements depends on the sensor's efficiency –  
<sub>943</sub> the ability to detect all or at least a known percentage of radiation quanta (particles  
<sub>944</sub> or photons) that hit it. The energy of the radiation is not so important; what bears  
<sub>945</sub> the information is the rate and the spatial distribution. Here the radiation does  
<sub>946</sub> not necessarily stop in the bulk, but rather continues its way. In spectroscopy, on  
<sub>947</sub> the other hand, the idea is that a particle stops within the sensor, depositing all  
<sub>948</sub> its energy, which is then measured via the freed charge carriers. The aim of the  
<sub>949</sub> experiments described in this chapter is to:

- <sub>950</sub> 1. Quantify the efficiency of the sCVD diamond in counting mode,
- <sub>951</sub> 2. Quantify the degradation of efficiency with respect to the received radiation  
<sub>952</sub> dose,
- <sub>953</sub> 3. Quantify the macroscopic effects on charge carrier behaviour with respect to  
<sub>954</sub> the received radiation dose and
- <sub>955</sub> 4. Define limitations for its use in spectroscopy.

<sub>956</sub> The results discussed here show that there are several limitations for using diamond as  
<sub>957</sub> a measurement device. All of them need to be taken into account for the measurement

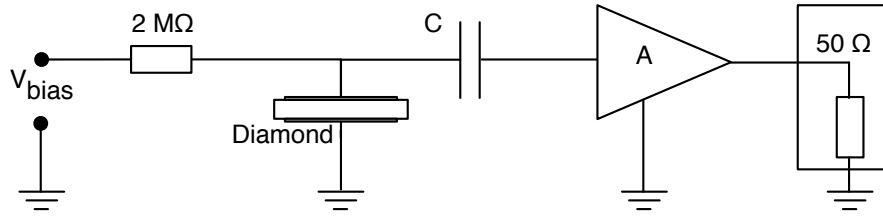


Figure 3.1: Diagram of a diamond detector readout chain.

device to perform reliably and stably. The first step is to build a setup that is insensitive to external electromagnetic interferences and minimises electrical noise in the system. The setup needs to be calibrated before use. Then, the measurement conditions have to be defined, such as the temperature, the type of radiation and its flux. This allows us to estimate the lifetime of the detector and predict the longterm change of the signal. This change can then be accounted for when interpreting the output data.

### 3.1 Measurement setup

To get reliable measurement results, great care has to go towards designing a measurement setup that minimises the noise in the measurements. Shielding has to be applied wherever possible. For instance, aluminium foil can be wrapped around the exposed parts of the system to shield them from external radio-frequency (RF) interferences. In addition, the sensors have to be covered to prevent the light from shining directly onto them. The incident photons can deposit enough energy to increase the leakage current of the detector.

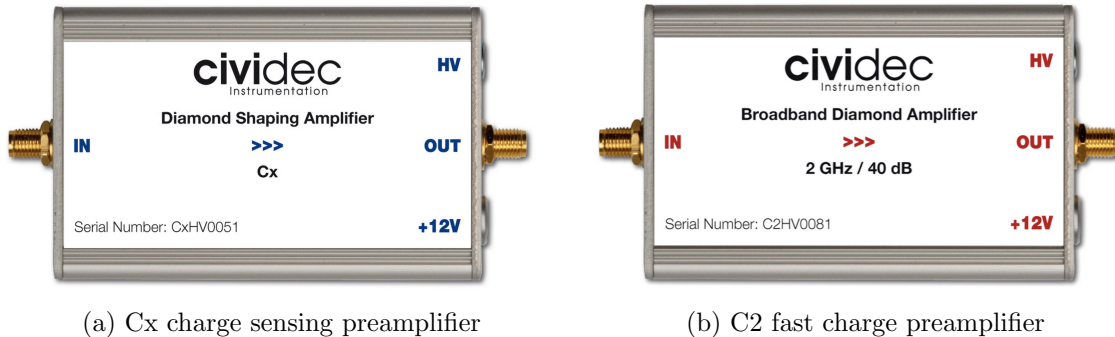
The measurements using diamond that are explained in these chapters were carried out using several measurement setups, but they are all similar in terms of the electrical signal chain. The measurement chain consists of three main parts: a diamond sensor, a signal preamplifier and a readout device, as seen in diagram 3.1. The signals propagating along the analogue chain (before being digitised by the readout device) are fast – in the GHz bandwidth range – and with low amplitudes – of the order of tens of  $\mu\text{V}$ . This gives rise to importance of RF shielding. Also, the connection between the carrier and the preamplifier has to be as short as possible to avoid capacitive signal losses in the transmission line. Finally, the system needs to be grounded properly.

#### 3.1.1 Preamplifiers

Two preamplifiers are used for the measurements, one sensitive to charge and the other to current. *CIVIDEC Cx* (figure 3.2a) is a charge sensing amplifier. Its high SNR (equivalent noise charge of  $300 + 30 \text{ pF}^{-1} \text{ e}^-$  and a reported gain of  $\sim 12 \text{ mV/fC}$ ) makes it a good choice for spectroscopic measurements with diamond

### 3.1. MEASUREMENT SETUP

---



(a) Cx charge sensing preamplifier

(b) C2 fast charge preamplifier

Figure 3.2: Amplifiers used for the charge and current measurements

987 sensors. *CIVIDEC C2* (figure 3.2b) is a fast current preamplifier with a 2 GHz band-  
 988 width limit. It is used for TCT measurements because of its fast response and a good  
 989 SNR. Both are embedded in an RF-tight aluminium box to reduce the noise pickup.  
 990 Both have an AC coupled input and an output with a  $50 \Omega$  termination.

#### 991 3.1.1.1 Calibration

992 The amplifiers have to be calibrated before use to determine their gain. Both are  
 993 calibrated using a square signal generator with a known amplitude step of  $U_{\text{in}} =$   
 994  $(252 \pm 5)$  mV. A 2 GHz oscilloscope with a 10 GS/s sampling is used to carry out  
 995 these measurements.

996 In the case of the Cx charge sensitive amplifier, the signal is routed through a  
 997 capacitor with a calibration capacitance  $C_{\text{cal}} = (0.717 \pm 0.014)$  pF and then to the  
 998 input of the amplifier. The pulse area behind the capacitor is  $a_{\text{cal}} = (5.0 \pm 0.5)$  pVs,  
 999 with the signal amplitude on the output amounting to  $U_{\text{Cx}} = (1.95 \pm 0.05)$  V. The  
 1000 input voltage step combined with the calibration capacitance yields a calibration  
 1001 charge  $Q_{\text{cal}} = C_{\text{cal}} \cdot U_{\text{in}} = (181 \pm 5)$  fC. The gain of the Cx amplifier is therefore  
 1002  $A_{\text{Cx}}^{\text{Q}} = \frac{U_{\text{Cx}}}{Q_{\text{cal}}} = (9.3 \pm 0.4)$  mV/fC or  $A_{\text{Cx}}^{\text{a}} = \frac{U_{\text{Cx}}}{a_{\text{cal}}} = (390 \pm 40)$  mV/pVs. The area-based  
 1003 amplification factor has a higher uncertainty ( $\sim 10\%$ ) than the amplitude-based  
 1004 factor ( $\sim 4\%$ ) due to the measurement limitations of the oscilloscope. Nevertheless,  
 1005 it can be used as an estimate for the integrated charge of a current pulse.

1006 To calibrate the C2 current amplifier, only the amplitude gain has to be measured.  
 1007 The input signal amplitude has to be such that it keeps the output amplitude within  
 1008 the amplifier's linear range, that is  $\pm 1$  V. The signal from the generator is therefore  
 1009 routed through a 36 dB attenuator to decrease its amplitude to  $U_{\text{inAtt}} = (3.95 \pm$   
 1010  $0.05)$  mV. Two amplifiers with different gains have been measured, because both  
 1011 are used for the measurements at different times. The output of the first amplifier  
 1012 amounts to  $U_{\text{C2-1}} = (860 \pm 5)$  mV. This yields the amplification gain equal to  $A_{\text{C2-1}} =$   
 1013  $\frac{U_{\text{inAtt}}}{U_{\text{C2-1}}} = (217 \pm 3)$ . The second amplifier has the output equal to  $U_{\text{C2-2}} = (632 \pm 5)$  mV  
 1014 with the gain equal to  $A_{\text{C2-2}} = (152 \pm 3)$ .

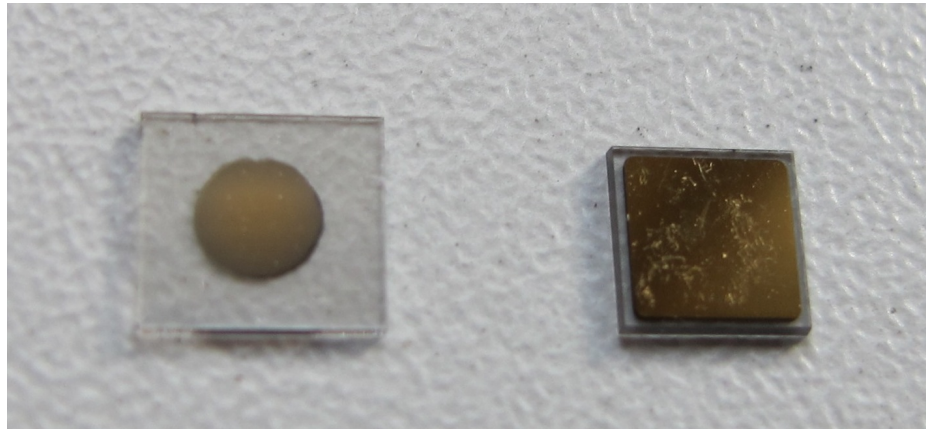


Figure 3.3: Two scCVD diamond samples: A IIa 1scdhq (left) and an E6 S37 (right)

### 3.1.2 Diamond samples

Detector-grade diamonds are very difficult to produce, mostly because it is very difficult to ensure a high enough purity of the lattice. The sensor samples used for these studies were bought at Element Six (E6) [5]. They all have the same standard dimensions. sCVD diamonds with dimensions  $4.7 \times 4.7 \text{ mm}^2$  are already sufficiently large for most of the beam monitoring applications and still affordable. One of the samples with dimensions of  $5.6 \times 5.3 \text{ mm}^2$  produced by IIa Singapore [7] was also sent to CERN to be characterised. The target thickness for all the samples is  $500 \mu\text{m}$ . Diamonds this thick yield a high enough signal-to-noise ratio for MIPs to be measured by the electronics. Table 3.1 shows all the samples used for this study. Two of them were later irradiated with 300 MeV pions and then compared to the pre-irradiated state. Irradiation doses for damaging the material need to be high – above  $10^{12}$  particles per  $\text{cm}^2$  to be able to observe change in the sensor’s behaviour.

	Name	Type	Producer	Dimensions [ $\text{mm}^2$ ]	Thickness [ $\mu\text{m}$ ]	Electrode	Irradiated
	S37	sCVD	E6	$4.7 \times 4.7$	548	Cr/Au	no
	S50	sCVD	E6	$4.7 \times 4.7$	537	Cr/Au	no
	S52	sCVD	E6	$4.7 \times 4.7$	515	Cr/Au	$1 \times 10^{14} \pi \text{ cm}^{-2}$
	S79	sCVD	E6	$4.7 \times 4.7$	529	Cr/Au	$3.63 \times 10^{14} \pi \text{ cm}^{-2}$
	ELSC	sCVD	E6	$4.7 \times 4.7$	491	Cr/Au	no
	1scdhq	sCVD	IIa	$5.6 \times 5.3$	460	Cr/Au	no

Table 3.1: Diamond sensor samples used

The diamond samples have quoted impurity densities of  $\leq 2 \times 10^{14} \text{ cm}^{-3}$  and nitrogen incorporation of  $\leq 1 \text{ ppb}$ . The electrodes were added by various companies and institutes. For instance, S52 was metallised by a company DDL (now defunct) while the Physics Department of the University of Firenze, Italy metallised the S79. There are also several techniques for producing the electrodes. The DDL contacts consist of three layers: DLC (diamond-like carbon)/Pt/Au with 4/10/200 nm thicknesses, respectively. The metallisation for S79, on the other hand is made up of Cr/Au with

### 3.1. MEASUREMENT SETUP

---

a total thickness of  $\sim$ 400 nm. The area coverage also differs from sample to sample. Diamonds must not be metallised until the very edge as the proximity of contacts with a high potential can lead to sparking. However, the areas not covered by the metallisation are less efficient because the fringe fields at the edges are not as strong as in the middle. This effectively reduces the sensitive area of the sensors. In the diamonds used here the effective area was anywhere from  $9\text{ mm}^2$  to  $18\text{ mm}^2$ . Leakage current through the bulk was below 1 ns, but increased for the irradiated samples. The capacitance was of the order of  $(2.0 \pm 0.3)\text{ pF}$ .

#### 3.1.3 Readout devices

Electrical signals in diamond detectors are in the GHz frequency range. To preserve this information, the readout device has to have a high bandwidth limit. For instance, a 250 MHz limit is enough for the spectroscopic measurements with the Cx charge amplifier, but might be insufficient for the current measurements with the C2 amplifier. Two devices are used take data shown in this chapter. The first choice is a 2 GHz LeCroy WaveRunner 204MXi-A. This specific model has a high enough limit for the fast current preamplifier signals. It offers a versatile solution for analogue signal readout – it is fast to set up and reliable. It is very convenient for use in lab tests and for experiments where small amounts of data are taken and where speed is not crucial. However, its slow acquisition speed turns out to be a bottleneck in the test beam experiment. Its initial 100 Hz readout rate decreases to a mere 20 Hz within 20 minutes, because every single trigger is saved as a separate file and the Windows operating system is not capable of handling 10000+ files in a single directory easily. This is why it has been exchanged with a DRS4 [4], an analogue readout device developed by PSI, Switzerland. This compact device is capable of recording up to four waveforms at a time at a steady rate of up to 500 Hz. Its 700 MHz bandwidth limitation is sufficient for the signal from the charge amplifier.

#### 3.1.4 Setup for the efficiency study using $\beta$ particles

The efficiency study of the diamond sensors has been carried out at CERN in the North Hall test beam facility. There a straight high-energy particle beam of  $\pi_{120}\text{ GeV}$  is provided to the users to calibrate their detectors. The beam had a transverse spread of  $\sigma = 10\text{ mm}$  in both axes. The particle rate is of the order of  $10^4\text{ }\pi\text{ cm}^{-2}\text{ s}^{-1}$ . A diamond sensor embedded in a PCB carrier has been placed in the beam spot perpendicular to the beam and connected via an SMA connector directly to a charge amplifier (described below). The amplified signal is read out using a LeCroy oscilloscope and a DRS4 analogue readout system (both described below). A computer is used as a controller and data storage for the readout device. A beam telescope is used as a reference detector. It is a device that helps to cross-check the measurements of the devices under test (DUTs) and to carry out spatially resolved studies on the DUTs. It consists of several pixellated sensor planes placed in series, which can track a particle's trajectory with a precision of a few  $\mu\text{m}$ . The sensor planes are positioned

in front of the DUT and behind it. Then the beam telescope acts as a trigger system – it triggers the readout of both the telescope data and DUT data when both the planes in front and behind the DUT recorded a hit by the incident particle. A particle detected by all the planes within the DUT window and the DUT itself counts towards its efficiency whereas a hit missed by the DUT means that the DUT is not 100 % efficient. To discard the hits that miss the DUT completely, a region of interest (ROI) can be chosen in the beam telescope planes. The equation for calculating the sensor efficiency is therefore

$$\epsilon = \frac{N_{\text{DUT}} \wedge N_{\text{telescope}}}{N_{\text{telescope}}} \quad (3.1)$$

for an ROI smaller than the sensitive region of the diamond.

### 3.1.5 Room temperature $\alpha$ -TCT setup

This TCT study is a follow-up of an extensive diamond TCT study at cryogenic temperatures [28]. The room-temperature TCT measurements have been carried out in the lab. The setup consists of a diamond sensor embedded in a PCB carrier, a current amplifier and an oscilloscope. To measure  $\alpha$  particles, their energy loss during their trajectory has to be minimised. Therefore the diamond is placed inside a vacuum chamber. The chamber is a steel tube with a diameter of 5 cm. On one side it is connected to a vacuum pump via a steel pipe. A feedthrough with an SMA connector is placed on the other side. A C2 current amplifier is connected directly onto the feedthrough. The amplified output is connected to the oscilloscope via an SMA cable. An  $^{241}\text{Am}$  source with a diameter of 2 cm and a height of 0.5 cm is fixed onto the sensor carrier (figure 3.4a, figure 3.4b). Then the carrier is inserted in the chamber and fixed in place using an air-tight clamp. The pump can then be switched on. It is capable of providing the inside pressure as low as  $10^{-4}$  mbar after approximately one hour of operation, but measurements can take place even after five minutes of evacuation, at around  $10^{-3}$  mbar. The most important thing to bear in mind is to switch the bias voltage of the sensor OFF during the process of evacuation, because the gas becomes more conductive at the pressure of the order of  $10^{-1}$  mbar, which is at the bottom of Paschen's curve [21]. A failure to switch off the bias voltage may cause a spark between the signal and ground line, destroying the amplifier.

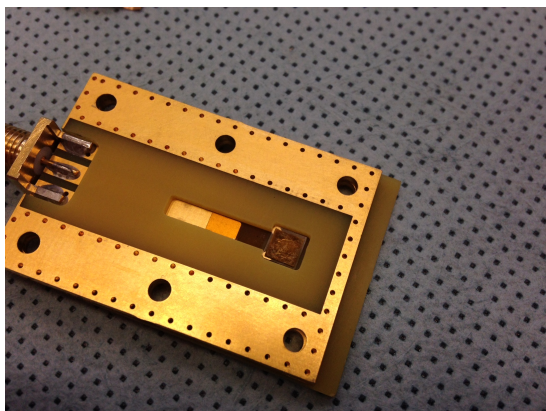
### 3.1.6 Cryogenic $\alpha$ -TCT setup

The experiment at cryogenic temperatures has been carried out in the cryolab at CERN. The room-temperature TCT setup has to be modified to allow for measurements at temperatures as low as 2 K. It consists of three parts:

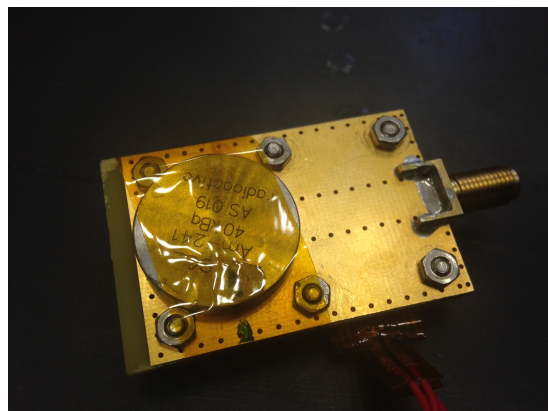
1. a cryostat – a thermally insulated cylinder capable of containing liquid helium,
2. an inlet – an air-tight mechanical tube with valves and feedthroughs at the top that is lowered in the liquid helium and

### 3.1. MEASUREMENT SETUP

---



(a) PCB carrier with an embedded diamond sample



(b) Radioactive source over the carrier

Figure 3.4: Positioning of the  $\alpha$ -source on top of the sensor carrier

1114     3. the diamond sample embedded in a PCB carrier with a fitted temperature  
1115     sensor, a heater and cables leading to the feedthroughs.

1116     The setup is described in detail in [28].

1117     When the diamond sample is placed in the PCB carrier and the  $^{241}\text{Am}$  source is in  
1118     place, the inlet is sealed and lowered in the empty cryostat. Then the inside volume  
1119     of the inlet is evacuated to down to  $10^{-5}$  mbar while the liquid helium is flowing into  
1120     the cryostat. To improve the thermal contact between the diamond and the coolant,  
1121     a small amount of helium gas is added inside the evacuated inlet, setting the vacuum  
1122     to around  $10^{-3}$  mbar. This value changes with time, because the gas condenses on  
1123     the walls of the inlet, reducing the number of floating particles. For this reason the  
1124     helium gas has to be added on an irregular basis. Every addition causes a significant  
1125     undershoot of the sample temperature, which had to be corrected for using a heater  
1126     placed on the back of the PCB carrier. Also, the added gas deteriorates the vacuum  
1127     inside the inlet. It is very important to monitor the pressure so as not to let it rise  
1128     above  $10^{-2}$  mbar. The gas at this pressure is significantly more conductive and could  
1129     cause a short circuit between the two diamond plates or in the SMA connectors,  
1130     destroying the amplifier. Furthermore, at approximately 60 K the helium gas has to  
1131     be evacuated from the inlet to avoid a potential explosion due to the expansion of  
1132     the gas with temperature.

1133     When the sample is cooled to the minimum temperature achievable by means  
1134     of liquid helium without over-pressurising it (4.2 K), the measurements start. A  
1135     temperature sensor placed on the back of the PCB carrier is used to measure the  
1136     temperature of the sample. After every temperature data point, the current through  
1137     the heater placed in the PCB next to the diamond sample is increased, warming up  
1138     the sample. The initial temperature time constant of the order of tenths of seconds at  
1139     low temperatures increases with temperature. Even more so when helium is evacuated  
1140     from the inlet at 60 K, removing the thermal bridge between the wall of the inlet and

the diamond sample. At the room temperature (RT), the time constant increases to the order of minutes.

## 3.2 Charged particle pulses and spectra

In previous chapter the ionisation profiles for different types of radiation were discussed. It is known that  $\beta$  and  $\gamma$  radiation induces a triangular electric pulse whereas  $\alpha$  radiation induces a rectangular one. However, their amplitude, width and rise/fall time depend heavily on the type of interaction with the diamond, the purity of the diamond and the bandwidth of the amplifier and the oscilloscope. This section shows the signal pulses of  $\alpha$ ,  $\beta$  and  $\gamma$  radiation with their respective energy distributions for the case of a diamond detector. Then follows a discussion of effects of noise on these measurements.

A CIVIDEC C2 current amplifier together with the LeCroy oscilloscope (both with a bandwidth limit of 2 GHz) has been used to record the pulse shapes whereas the Cx charge amplifier is used for charge measurement. A 2 GHz bandwidth limit defines the minimum rising time equal to  $t_r \simeq \frac{0.34}{BW} = \frac{0.34}{2 \times 10^9} = 170$  ps, therefore the system is capable of measuring pulses with a minimum FWHM  $\simeq 170$  ps. This already makes it impossible to measure the initial peak in the  $\alpha$  response due to the two flavours of charge carriers travelling. If a charge carrier travelling through the bulk takes  $t_{t1} \sim 6$  ns to get to the electrode on the other side ( $d_1 \sim 500$   $\mu m$ ), the carrier with the opposite charge and a shorter path to the closer electrode – max.  $d_2 \sim 10$   $\mu m$  – only takes  $t_{t2} \sim \frac{d_2}{d_1} t_{t1} = 120$  ps. A drift time this short induces a current pulse that is too narrow for the C2 amplifier or the oscilloscope to be able to observe.

Figure 3.5 shows a set of pulses and an averaged pulse for  $\alpha$ ,  $\beta$  and  $\gamma$  radiation using an  $^{241}Am$ ,  $^{90}Sr$  and  $^{60}Co$  source, respectively. The particles are measured with the non-irradiated sCVD diamond S37.  $\alpha$  particles always produce the same signal pulse, but with a high noise RMS. The averaging suppresses the noise while still retaining most the information. It does, however, smear the rising and falling edge, increasing the rise time. The  $t_r$  is now of the order of 0.5 ns. Both  $\beta$  and  $\gamma$  pulses look similar - triangular and with a wide range of amplitudes. Here the pulse count is low, so the pulses with a high amplitude are not recorded. A trigger set very high would be needed to “catch” them with the oscilloscope.

### 3.2.1 Noise limitations

Noise is a major limiting factor in particle detection. It defines the minimum measurable particle energy and the minimum measurement resolution. It is hence important to minimise the electric noise in the detector signal. The major noise contribution comes from poor shielding from external electromagnetic sources. These often cause ringing, whereby the signal oscillates with a frequency defined by the external source. The ringing makes high-frequency measurements impossible. Another source of noise

### 3.2. CHARGED PARTICLE PULSES AND SPECTRA

---

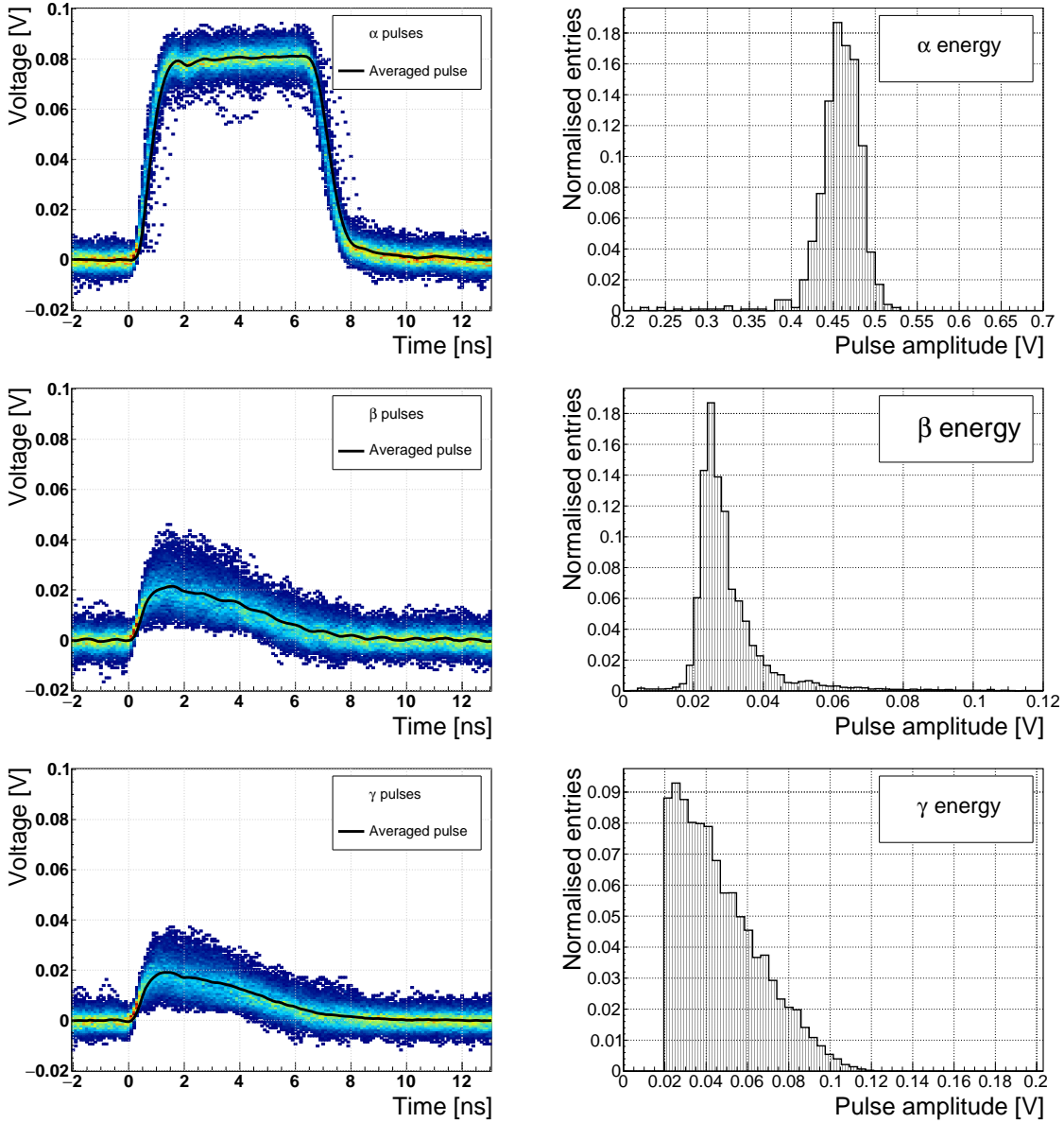


Figure 3.5: Superimposed and averaged pulses (a, b and c, current amplifier) and distributions of deposited energy (d, e, f, charge amplifier) for three types of radiation. Note the scale on the X axis of the distributions.

is the sensor itself. In the case of silicon, natural light increases the number of thermally excited free charge carriers, increasing the leakage current. This is not the case for diamond, which is with its high energy band gap insensitive to visible light. Nevertheless, any noise produced by the sensors is amplified by the signal amplifiers, which add an additional noise of the analogue electrical circuit to the amplified signal. Finally, the digitisers add the quantisation noise to the digitised signal. If the measurement range is significantly higher than the actual measured signal, the quantisation noise can be a significant contributor to the decrease of the overall mea-

1188 surement resolution.

### 1189 3.3 Radiation limitations

1190 Exposure to ionising radiation degrades sensors. It deforms the lattice by displacing  
1191 the atoms. Various types of lattice defects can be created in diamond, similar to those  
1192 in silicon: vacancies, interstitials etc. [31] These deformations introduce new discrete  
1193 energy levels between the valence and conduction band. Charge carriers drifting in  
1194 their vicinity can get trapped, their energy falling to the energy level of the trap.  
1195 Their emission back to the conduction band depends on how deep the trap is (how  
1196 far away from the conduction band it is). The carriers caught in the shallow traps of  
1197 the order of 100 meV below the conduction band are excited back up already by means  
1198 of the thermal excitation. This phenomenon has a short time constant, dependant  
1199 on the environmental temperature. Those stopped by deep traps near the middle  
1200 of the band gap need more energy and thus more time to be emitted to either the  
1201 conduction or valence band. Some charge carriers remain trapped for long periods.  
1202 If they build up in a certain region of the diamond, their charge starts affecting the  
1203 surrounding electric field – space-charge forms. It can either help or counteract the  
1204 field, depending on the polarity of the carrier.

1205 The energy band jumping goes the other way, too. The carriers in the valence  
1206 band may use the intermediate energy levels as “stepping stones” to jump to the  
1207 conduction band and start drifting in the externally applied electric field. This is  
1208 called the leakage current.

1209 The electrons and holes stopped in these traps cause a decrease of the induced  
1210 current on the electrodes. This yields a lower integrated charge in an irradiated sensor  
1211 than that in a non-irradiated one. Charge collection efficiency is therefore correlated  
1212 with the level of irradiation.

1213 This section contains a study of the effects of pion ( $\pi_{300 \text{ MeV}}$ ) irradiation on the  
1214 charge collection efficiency of sCVD diamond detectors. To carry out this study,  
1215 two diamond samples have been irradiated to doses of  $1 \times 10^{14} \pi \text{ cm}^{-2}$  (S79) and to  
1216  $3.63 \times 10^{14} \pi \text{ cm}^{-2}$  (S52). Then a test beam campaign has to be carried out to observe  
1217 the charge collection efficiency at different bias voltage settings. The efficiency values  
1218 acquired are used to determine the effective drop in efficiency with respect to received  
1219 radiation dose. This is to test if the collected charge  $Q$  is inversely proportional to  
1220 the received dose  $\Phi$ . A procedure defined by a collaboration researching diamond  
1221 behaviour RD42 has been applied to the measured values to extract the damage factor.  
1222 The next subsection contains measurements and results of a long-term stability study  
1223 using  $\alpha$  and  $\beta$  particles. In particular, the charge collection efficiency as a function  
1224 of time is measured during the measurements with  $\beta$  and  $\alpha$  radiation. To investigate  
1225 this effect on the scale of charge carriers, the change of TCT pulses with time is  
1226 observed. Finally, a procedure that improves the pulse shape and with it the charge  
1227 collection is proposed.

### 3.3. RADIATION LIMITATIONS

---

#### 3.3.1 Quantifying radiation damage in diamonds

Radiation damage varies with the type of radiation (particles or photons) and its energy. There are several models existing [27, 26] that try to explain the impact of irradiation and to provide *hardness factors* to compare the radiation damage between different particles. The standard way is to convert the damage into *neutron equivalent* [14]. Some models have been extensively verified with simulations and with experiments. In these experiments charge collection in sensors is measured before and after irradiation. This procedure is repeated several times, with a measurement point taken after every irradiation. When a set of measurements of charge collection is plotted against the radiation dose received by a specific particle at a specific energy, a damage factor  $k_\lambda$  can be extracted. Damage factors have to be measured across a range of energies and types of radiation to properly quantify the damage in the sensors. They are then compared against the simulations to verify that the experimental observations are in line with the theory.

Diamond is an expensive material and the technology is relatively new as compared to silicon. Therefore not many institutes are carrying out diamond irradiation studies. To join the efforts, the RD42 collaboration [11] was formed. It gathers the experimental data from diamond irradiation studies. Unlike with silicon, the experimental results so far show no significant correlation with the NIEL (non-ionising energy loss) model [27], which correlates detector efficiency with the number of lattice displacements. Therefore an alternative model was proposed [26], correlating the diamond efficiency with the number of displacements per atom (DPA) in the bulk. The idea is that if the recoil energy of an incident particle is higher than the lattice binding energy (42 eV for diamond), the atom is displaced from its original position. The newly formed vacancy acts as a trap for drifting charge carriers. The more displacements that form in the bulk, the higher is the probability that a drifting carrier will get trapped, effectively reducing the induced signal. However, different types of particles interact differently with the bulk. In addition the mechanisms of interaction at low energies are different to those at high energies. To assess the damage for individual particles at a range of energies, simulations need to be run first. The simulation shown in [26] shows the DPA model for a range of energies of proton, pion and neutron irradiation in diamond. Figure 3.6 contains the simulation results as well as the superimposed empirical results of several irradiation studies. According to the figure, a 300 MeV pion beam damages the diamond bulk twice as much as a 24 GeV proton beam. The data points obtained by RD42 are also added to the figure. They have been normalised to damage by 24 GeV protons. Finally, the data point measured in the scope of this thesis has been added for comparison. The derivation is done below.

##### 3.3.1.1 Irradiation with a $\pi_{300 \text{ MeV}}$ beam

The samples were irradiated at the Paul Scherrer Institute (PSI) [10] by means of a beam of pions with an energy of 300 MeV (kinetic energy 191.31 MeV) and with a

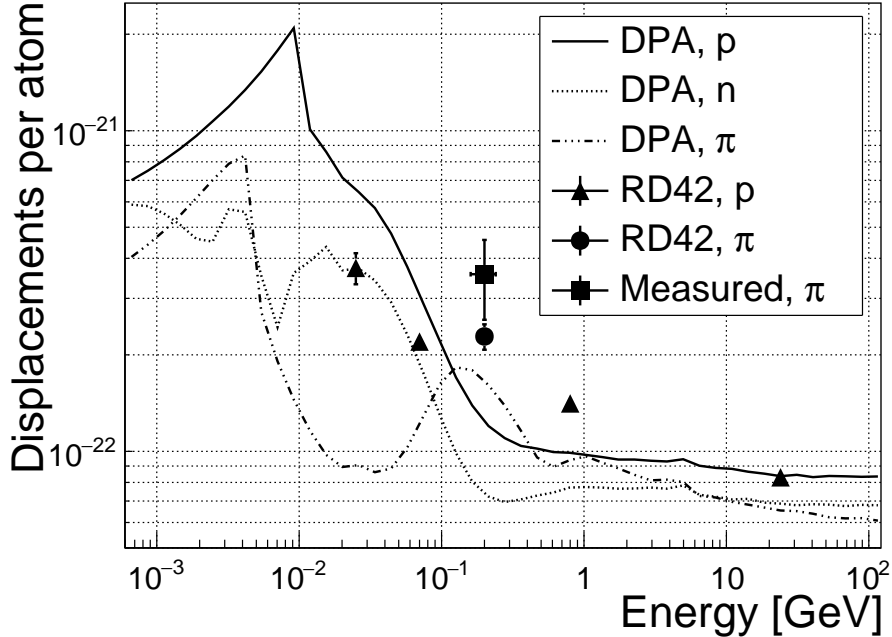


Figure 3.6: Diamond radiation damage - a model based on displacements per atom [26]. Added are data points for protons and pions by RD42 [35] and one data point for pions measured in the scope of this thesis.

flux of up to  $1.5 \times 10^{14} \pi \text{ cm}^{-2}$  per day. The system has a 10 % uncertainty on the beam energy. In addition, their quoted uncertainty on the measurement has an error of  $\pm 20\%$ . Looking at the pion damage curve in figure 3.6,  $\pi_{300 \text{ MeV}}$  point sits on a steep section of the DPA curve. This means that a deviation in beam energy can have a significant effect on the damage.

Two diamond samples, S52 and S79, were put in the  $\pi_{300 \text{ MeV}}$  beam in the 2014 PSI irradiation campaign; S52 to  $(1 \pm 0.21) \times 10^{14} \pi \text{ cm}^{-2}$  and S79 to  $(3.63 \pm 0.77) \times 10^{14} \pi \text{ cm}^{-2}$ . During the process, the golden electrodes got slightly activated, but the activation decayed in two weeks.

### 3.3.1.2 Charge collection efficiency and charge collection distance

Three diamonds – non-irradiated S37 and irradiated S52 and S79 – were tested in a  $\pi_{120 \text{ GeV}}$  test beam in the SPS North Experimental Area at CERN [18] before and after irradiation. The goal was to estimate the charge collection efficiency (CCE) and charge collection distance (CCD) as a function of irradiation dose. The samples were primed (pumped) prior to data taking using a  $^{90}\text{Sr}$  radioactive source. The data were then taken at a range of bias voltages ranging from 30 V to 900 V, yielding between 0.06 V/ $\mu\text{m}$  and 1.8 V/ $\mu\text{m}$  electrical field in the bulk. Every data point contained approximately  $5 \times 10^4$  measured particles. The charge deposited by the particles was measured using a CIVIDEC Cx charge preamplifier. As expected, the integrated

### 3.3. RADIATION LIMITATIONS

---

1288 amplitude spectrum followed a landau distribution. Its most probable value (MPV)  
 1289 was used to calculate the most probable collected charge  $Q_i$ :

$$Q_i [e^-] = \frac{Q_i [fC]}{1.6 \times 10^{-4}} = \frac{MPV [mV]}{A [mV/fC]} \cdot 6.241 \times 10^4 \quad (3.2)$$

1290 where  $A = 9.2 \text{ mV/fC}$  is the preamplifier gain factor. The CCD was then calculated  
 1291 using the average number of electron-hole pairs produced per micrometer in diamond  
 1292  $\delta_d = 36 \text{ e-h } \mu\text{m}^{-1}$  (from table 5.2):

$$CCD = \frac{Q_i}{\delta d} \quad (3.3)$$

1293 The resulting CCD for the three measured samples at bias voltages ranging from  
 1294  $0.2\text{--}1.6 \text{ V } \mu\text{m}^{-1}$  is shown in figure 3.7a. S37 exhibits a full collection distance already  
 1295 at  $0.4 \text{ V } \mu\text{m}^{-1}$  whereas the irradiated samples have a more gentle increase of CCD  
 1296 with increasing bias voltage. It is evident that at  $1 \text{ V } \mu\text{m}^{-1}$  the maximum CCD has  
 1297 not been reached in the case of S79 and S52. Nevertheless, to compare the measured  
 1298 data point with those provided by RD42, the CCD at  $1 \mu\text{m}$  has to be taken.

#### 1299 3.3.1.3 Irradiation damage factor

1300 The irradiation damage factor  $k$  is a way to quantify irradiation damage of a specific  
 1301 particle at a specific energy. Via this factor different types of irradiation can be  
 1302 compared. It is obtained experimentally by measuring the CCD of a number of  
 1303 samples at various irradiation steps and fitting the equation 3.5 to the data.  $\lambda$  is the  
 1304 measured CCD,  $\lambda_0$  is the CCD of a non-irradiated sample and  $\Phi$  the radiation dose.  
 1305 As a reference, the damage factor for 24 GeV protons is set to  $1 \times 10^{-18} \mu\text{m}^{-1} \text{ cm}^{-2}$ .

$$\frac{1}{\lambda} = \frac{1}{\lambda_0} + k_\lambda \cdot \Phi \quad (3.4)$$

$$\lambda = \frac{\lambda_0}{k_\lambda \lambda_0 \Phi + 1} \quad (3.5)$$

1306 The data points with the maximum CCD obtained in the test beam measurements  
 1307 are plotted against radiation dose received (see figure 3.7b). Equation 3.5 is fitted  
 1308 to the data points and a damage factor  $k_\lambda = (4.4 \pm 1.2) \times 10^{-18} \mu\text{m}^{-1} \text{ cm}^{-2}$  was  
 1309 obtained. This value is for a factor of two higher than the damage factor obtained by  
 1310 RD42. This could be due to an insufficient priming time ahead of the measurement.  
 1311 In addition, the diamond samples have not been polished and re-metallised after  
 1312 irradiation, as is the case for the RD42. Also, with only two samples measured, the  
 1313 statistical uncertainty is high. Nevertheless, it can be concluded that the 300 MeV  
 1314 pions damage the diamond bulk more than the 24 GeV protons.

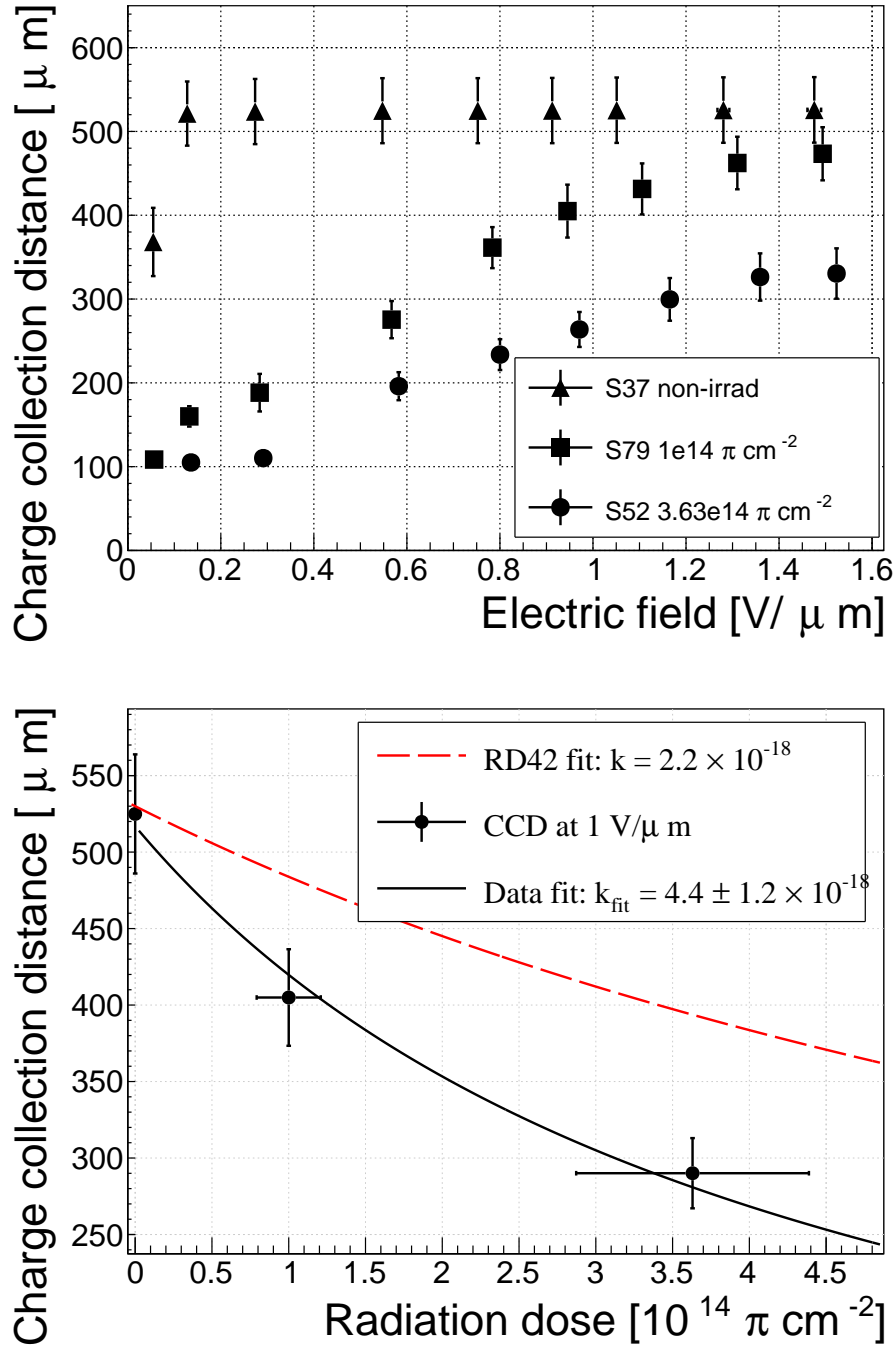


Figure 3.7: First figure shows the CCD for S37, S79 and S52 at a range of bias voltage settings. The charge collection distance at 1 V/μm bias voltage for the three diamond samples is then compared to the RD42 data for pion irradiation in the second figure. The data points are about 15–25 % lower than expected from the RD42 data [35].

### <sup>1316</sup> 3.3.2 Long-term measurement stability

<sup>1317</sup> An important requirement for particle detectors is a stable performance over long  
<sup>1318</sup> periods of time. For instance, the charge collection for a defined radiation type and

### 3.3. RADIATION LIMITATIONS

---

1319 quantity must not change over time or has to change in a predicted way. Diamonds  
1320 are stable as long as their environment and their operating point does not change  
1321 significantly. The stability of diamond detectors depends on many factors (material  
1322 purity, polishing process, electrode material, irradiation damage etc.). The aim is  
1323 to study the behaviour of diamond under controlled conditions, with the goal to  
1324 understand its limitations. One of these limitations is for sure the received radiation  
1325 dose as it can affect the long-term stability of the sensor during operation.

1326 The three diamond samples (S37, S79 and S52) have been exposed to two different  
1327 types of ionising radiation for a longer period to see if their behaviour changes over  
1328 time. Two parameters have been observed in particular:

- 1329     1. Charge collection of  $\beta$  particles and
- 1330     2. Charge collection and ionisation profile of  $\alpha$  particles.

1331 The results in this and in the next section will show that, in both cases, priming plays  
1332 an important role in improving the diamond measurement stability.

#### 1333 3.3.2.1 $\beta$ long-term stability

1334 The diamond samples have undergone a long-term stability test using  $\beta$  radiation.  
1335 This has been done using a  $^{90}\text{Sr}$  source emitting  $\sim 2$  MeV electrons at a rate of  
1336 approximately  $10^4 \text{ e}^- \text{ cm}^{-2}$ . To simulate the initial conditions in HEP experiments,  
1337 the sensors must not be primed before starting the measurements. The measurement  
1338 setup consists of a diamond sample (S37, S52 or S79) with the Cx spectroscopic  
1339 amplifier, a silicon diode with a C6 amplifier for a trigger and a  $^{90}\text{Sr}$  source on  
1340 top. A particle emitted by the source traverses the sensor bulk and hits the silicon  
1341 diode, triggering the analogue signal readout. The source is left on the top for the  
1342 course of the experiment. The measurements, however, are taken at discrete times.  
1343 For every data point, approximately  $10^4$  triggers are recorded. The offline analysis  
1344 of the recorded signal pulse amplitudes yields a landau distribution for every data  
1345 point. The most probable value (MPV) of the distribution is proportional to the  
1346 collected charge by the diamond sensor. The resulting graph of charge collection over  
1347 time (see figure 3.8) shows that the charge collection efficiency improves when the  
1348 diamond sensor is primed with a  $\beta$  source. This is especially evident in the case of  
1349 the two irradiated samples. S79 achieves close to a full efficiency whereas S52 reaches  
1350 about 50 %. Both increases are significant. At a received dose of approximately  
1351  $4 \times 10^6$  particles the signal stabilises. As expected, the signal of the non-irradiated  
1352 S37 does not change with time – this pure sCVD diamond sample has the maximum  
1353 collection distance from the start of the measurement.

1354 It should be noted that the  $\sim 2.28$  MeV electrons emitted by this source are not  
1355 MIPs; their charge deposition is higher than that of an electron MIP, according to the  
1356 Bethe-Bloch distribution [16]. Nevertheless, for the purpose of these measurements  
1357 this energy was adequate since only the relative change in charge collection was of  
1358 our interest.

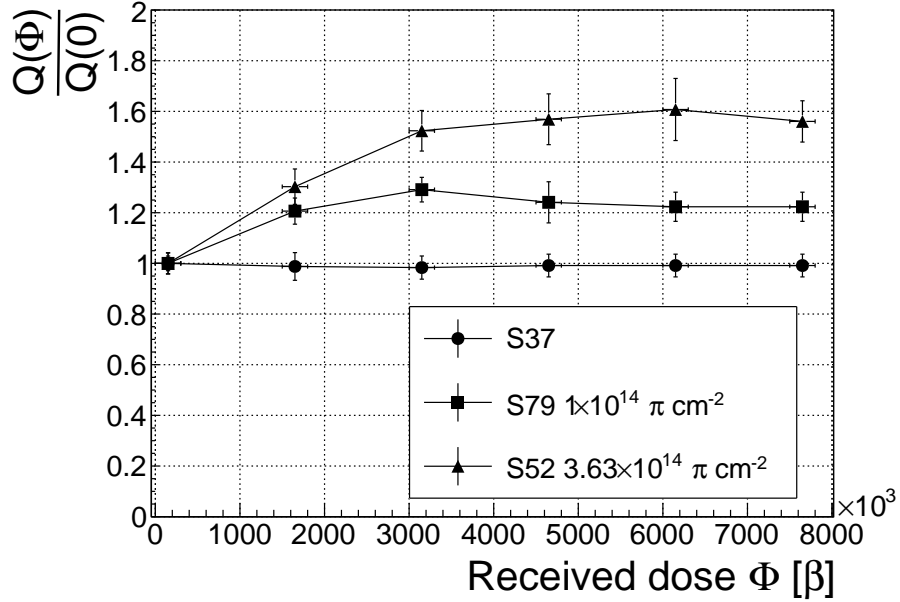


Figure 3.8: Relative increase of charge collection over time due to priming with the  $^{90}\text{Sr}$  radioactive source. The charge collection for the non-irradiated S37 stays constant. The bias voltage for this measurement is 1 V/ $\mu\text{m}$ .

To sum up, diamond is a good choice for  $\beta$  radiation detection. Even if damaged by radiation, it reaches a stable charge collection at a received dose of  $\sim 4 \times 10^6$  MIP particles. The efficiency decreases with a high irradiation dose (effects visible above  $10^{12}$  MIP  $\text{cm}^{-2}$ ). However, the decrease can be accounted for if the damage factor and the rate and energy of the particles are known.  $\gamma$  radiation has a similar impact on the diamond as the  $\beta$  because the ionisation mechanism is the same. The incident photons, if they interact with the diamond, prime the bulk, causing the increase in charge collection efficiency. The difference, however, is that the interaction probability (cross section) is lower for gammas [41, 25].

### 3.3.2.2 $\alpha$ long-term stability

This part discusses the stability of irradiated diamond sensors during  $\alpha$  measurements. An  $^{241}\text{Am}$  source is used, emitting  $\alpha$  particles with a mean energy of 5.5 MeV. It is safe to assume that they will behave differently than when subject to  $\beta$  radiation. This is due to the point-like charge carrier creation when an  $\alpha$  particle penetrates the bulk and stops at a depth of  $\sim 14 \mu\text{m}$  (for a 5.5 MeV particle). The deposited energy produces  $\frac{5.5 \text{ MeV}}{13.6 \text{ eV}} = 4 \times 10^5$  e-h pairs. Compared to a MIP, which produces an MPV of  $500 \mu\text{m} \times 36 \text{ e-h } \mu\text{m}^{-1} = 18 \times 10^3$  e-h pairs in a  $500 \mu\text{m}$ , the collected charge is for a factor of 22 higher. In addition, the energy is deposited in a small volume –  $14 \mu\text{m}$  in depth and  $\sim 20 \text{ nm}$  radially [28]. This dense distribution of charge carriers affects their behaviour at the start of the drift. Furthermore, carriers of only one

### 3.3. RADIATION LIMITATIONS

---

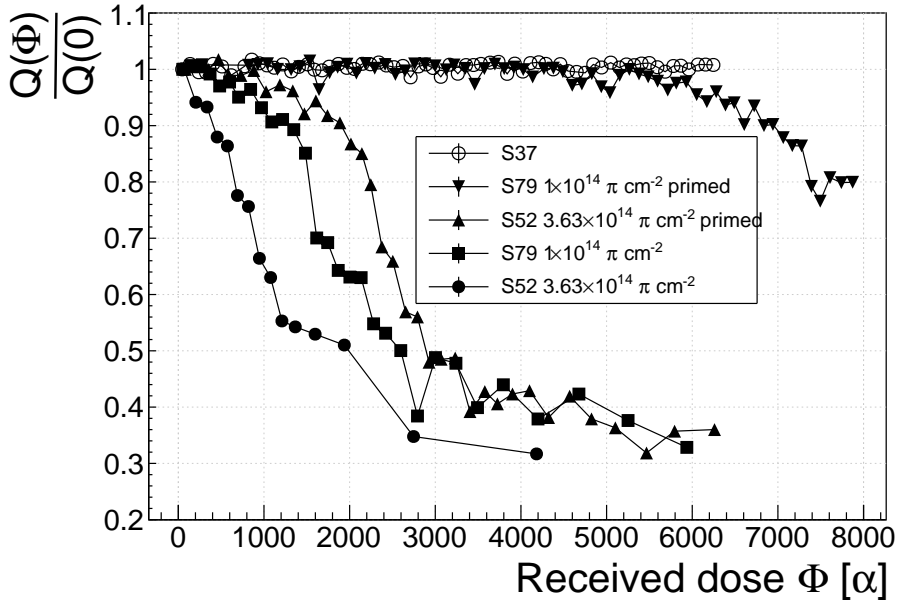


Figure 3.9: Relative decrease of collected charge with time for non-irradiated and irradiated diamond samples.

1379 polarity drift through the sensor while those of the opposite polarity almost instantly  
 1380 recombine with the adjacent electrode. Taking into account that the diamond bulk  
 1381 has been damaged by irradiation, these two phenomena might have an effect on the  
 1382 operation of the detector on a macro scale.

1383 The first test has been carried out using the Cx spectroscopic amplifier, with  
 1384 the bias voltage of the samples set to +500 V. Figure 3.9 shows the results of 6500  
 1385 recorded hits at a rate of  $\sim 7$  particles per second. The collected charge  $Q(\Phi)$  for  
 1386 the non-irradiated sample is stable as compared to the initial collected charge  $Q(0)$   
 1387 (plotted as a relative value  $\frac{Q(\Phi)}{Q(0)}$ ). It is expected that the irradiated samples will have  
 1388 a lower charge collection efficiency than the non-irradiated sample. However, their  
 1389 initial efficiency suddenly drops after a certain period of time. The initial efficiency  
 1390 after priming with  $\beta$  particles is higher than that without priming, but eventually it  
 1391 deteriorates again. In addition, the spread of measured energies increases significantly.  
 1392 Finally, the particle counting rate decreases with the decreased efficiency.

1393 To investigate this sudden drop in efficiency, the current pulse shapes using a  
 1394 C2 current amplifier have to be observed (see figure 3.10). The shape of the pulse  
 1395 holds more information about the charge carrier properties in the sensor than solely  
 1396 the value of the integrated charge. This time only the primed S79 sample has been  
 1397 tested. Both hole and electron collection are observed to determine whether they  
 1398 behave differently or not. The sample has been measured long enough for the pulse  
 1399 shapes to start changing. The data in figures 3.10 show that the initially stable pulses  
 1400 start deteriorating – suddenly several different shapes start appearing, some still very  
 1401 similar to those from the beginning while the others with almost zero amplitude.

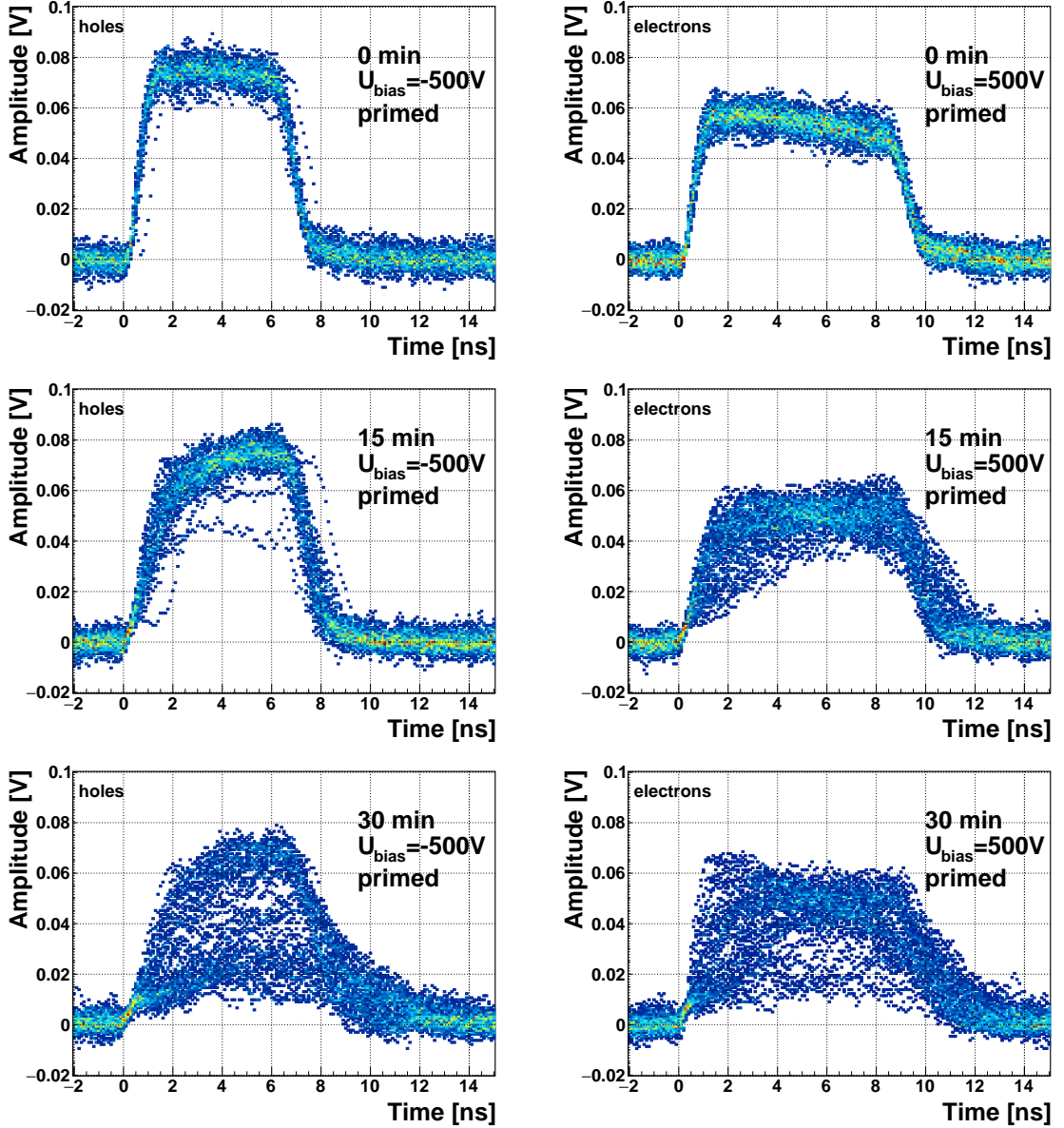


Figure 3.10: The signal of the irradiated and primed S79 deteriorates with time for both polarities. Every plot contains 60 superimposed pulses.

1402 Some charges get stopped in the charge traps in the bulk for a long time, building  
 1403 up regions of space charge. The built up space charge affects the electric field, making  
 1404 it non-uniform. The non-uniform field in turn affects the drifting carriers, slowing  
 1405 them down or speeding them up, depending on the field gradient. Since the movement  
 1406 of the carriers is inducing the electric current, the field gradient can be observed in  
 1407 the signal.

1408 The second test with the C2 current amplifier has been carried out as follows: At  
 1409 the beginning of the test when the diamond is still operating stably, 60 pulses are  
 1410 recorded. An average pulse is calculated. This is a reference pulse for the subsequent

### 3.3. RADIATION LIMITATIONS

---

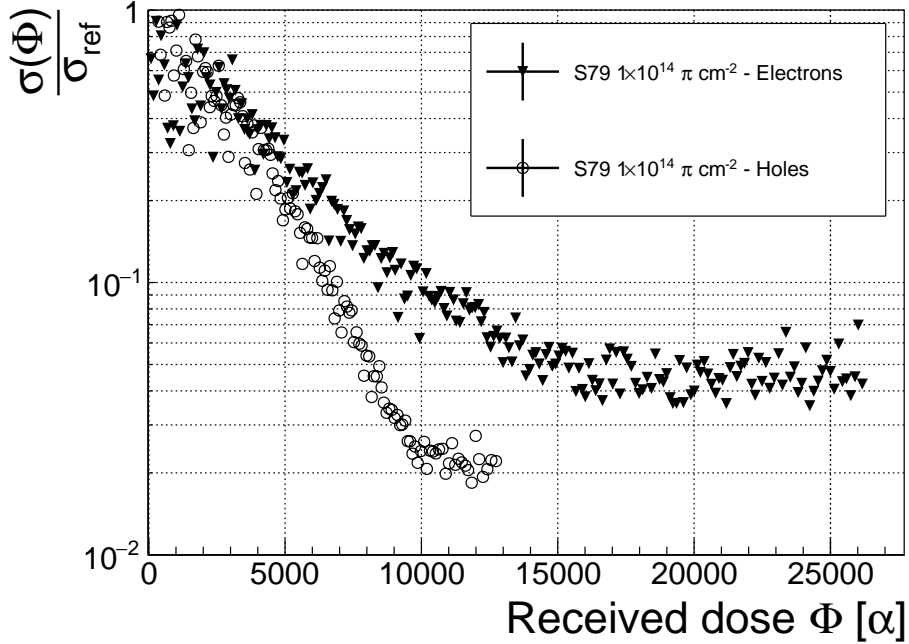


Figure 3.11: Deterioration of the pulse shapes with time

measurement points. Then an RMS of the single pulses with respect to the reference pulse is calculated and the values are summed together ( $\sigma_{\text{ref}}$ ).

All the subsequent data points also consist of a set of 60 pulses. At every data point the summation of the RMS values of the individual pulses with respect to the initial averaged pulse is calculated ( $\sigma$ ). The ratio between the initial  $\sigma_{\text{ref}}$  and discrete values  $\sigma$  gives a measure of change of the pulse shape with respect to the reference pulse at the start of the measurement. Figure 3.11 shows the ratio  $\frac{\sigma_{\text{ref}}}{\sigma(\alpha \text{ dose})}$ . From the data obtained it can be concluded that initial pulse shape quickly starts deteriorating. In fact, the deterioration of the shape follows an approximate exponential decay function, which can be fitted to the data. The resulting decay constants for electrons and holes are  $\tau_e = (4400 \pm 150) \alpha^{-1}$  and  $\tau_h = (3300 \pm 140) \alpha^{-1}$ . The electrons retain the initial shape for longer. The deteriorated shapes also seem to be for a factor of 2 better than those of the holes.

Finally, an effort has been made to find a way for the pulse shapes to return to their initial state. Five methods are listed:

1. Removing the source and leaving the bias voltage switched on,
2. Removing the source and switching the bias voltage off,
3. Priming with  $\gamma$  at a rate of  $400 \text{ s}^{-1}\text{cm}^{-1}$  without applied bias voltage,
4. Priming with  $\beta$  at a rate of  $1000 \text{ s}^{-1}\text{cm}^{-1}$  with applied bias voltage and
5. Priming with  $\beta$  at a rate of  $1000 \text{ s}^{-1}\text{cm}^{-1}$  without applied bias voltage.

---

*CHAPTER 3. EXPERIMENTAL RESULTS*  
*DIAMOND IRRADIATION STUDY*

---

1431 The diamond sample S79 is first primed using a  $^{90}\text{Sr}$  source for about one hour.  
1432 Then the bias voltage is switched on and an  $^{241}\text{Am}$  source is put on top. The pulses  
1433 produced by the incident  $\alpha$  particles have a proper rectangular pulse at the beginning,  
1434 but then start changing – first gradually and later increasingly more in an erratic way,  
1435 as described in the text above. After approximately 30 minutes, one of the methods is  
1436 tested. When a “healing” procedure is started, a set of 60 pulses is taken at irregular  
1437 points of time to observe the change in the pulse shape and to assess the quality of the  
1438 “healing” procedure. Then the bias voltage is switched off and the sample is primed  
1439 again to reset its state before starting with the next run.

1440 The results depicted in figure 3.12 show that the methods (3) and (5) improve the  
1441 shape, method (2) helps slowly, (1) does not show any change with time and (4) at first  
1442 improves, but then significantly degrades the shape. The effect observed in method  
1443 (4) has already been described in [32]. The “healing” process therefore depends on  
1444 the rate of radiation, the bias voltage and the time of exposure. The ionising radiation  
1445 creates free charges, which quickly recombine close to the place of generation. It is  
1446 likely that they also release the charges trapped during the measurement, reducing the  
1447 overall effect of the space charge. The traps get filled with both flavours of carriers,  
1448 thus they are neutralised. The pulse shape gradually returns to its initial state.

	Procedure	Source	Bias voltage	Effectiveness
1449	1	/	ON	no
	2	/	/	slow
	3	$^{60}\text{Co}$	/	YES
	4	$^{90}\text{Sr}$	ON	no
	5	$^{90}\text{Sr}$	/	YES

1450 Table 3.2: Effectiveness of healing procedures

1451 In summary, the shape of the pulses caused by  $\alpha$  radiation changes with time  
1452 for irradiated samples. The shape of the pulses gets distorted and becomes erratic.  
1453 Charge collection decreases and its spread increases. This happens even faster for  
1454 non-primed diamonds. To “heal” the diamond – to bring the pulse shapes back to  
1455 their initial shape – the sample must be primed using a  $\beta$  or a  $\gamma$  source for several  
1456 minutes at the bias voltage set to 0 V. Switching to the inverse polarity for a few  
1457 seconds helps a bit, but in a long run distorts the signal, which cannot get back to  
1458 its initial shape.

## 1459 **3.4 Temperature limitations**

1460 A test has been carried out to evaluate the effect of temperature changes on the  
1461 output signal of the diamond sensors. A cryostat filled with liquid helium is used to  
1462 cool down the sensor during the measurement process. The current signal response  
1463 to  $\alpha$ -particles is measured at 18 temperature points between 4 K and 295 K. At every  
1464 temperature point, a set of 300 pulses is read out at various bias voltages. Resulting  
1465 data show that the charge collection is stable down to 150 K, where it starts decreasing

### 3.4. TEMPERATURE LIMITATIONS

---

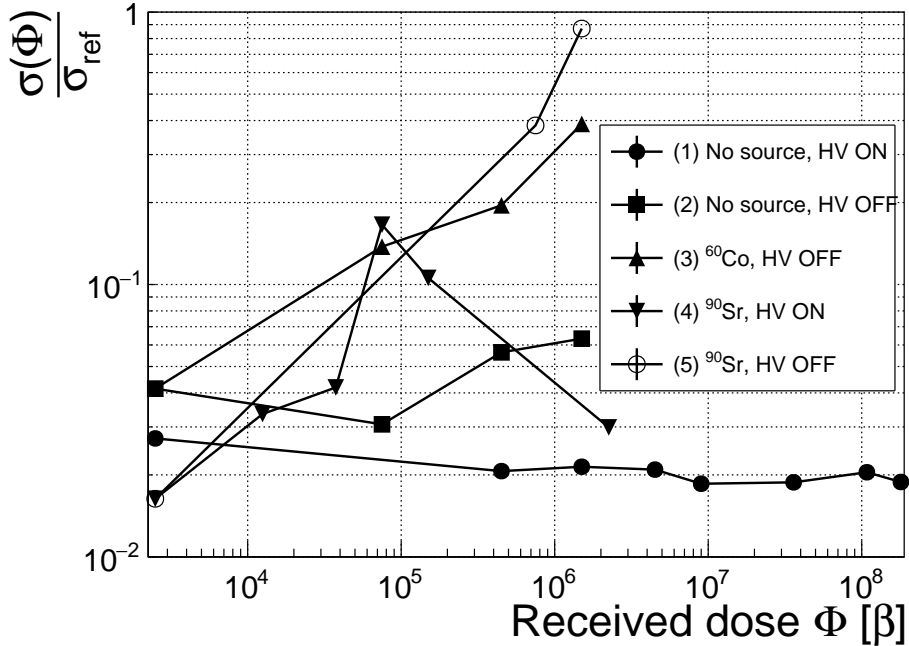


Figure 3.12: Comparison of the five procedures for the “healing” process for an irradiated diamond that had been exposed to  $\alpha$  radiation with a rate of  $10^1 \text{ s}^{-1}$ , with the bias voltage switched on, for at least 30 minutes.

and stabilises again at about one third of the initial value at 75 K. This behaviour was first measured and discussed by H. Jansen [28].

The band gap energy in diamond is equal to  $E_g = 5.5 \text{ eV}$  while the average energy to produce an electron-hole pair is  $E_{e-h} = 13.25 \text{ eV}$ . This means there is excessive energy deposited in the diamond bulk. The incident  $\alpha$ -particle stops within  $\sim 10\text{--}15 \mu\text{m}$  of the bulk, transferring all its energy to the lattice during deceleration. A part of this energy directly ionises the carbon atoms, creating free electron-hole pairs. The positively charged hole and the negatively charged electron in the hole attract each other via the Coulomb force and may undergo a bonding process during which a phonon is emitted.

The remaining energy, however, is converted into lattice vibrations (phonons [45, 28]). This means that the lattice within the ionisation volume (approximately  $\sim 15 \mu\text{m} \times \sim 2 \text{ nm}$  in size) is briefly heated up. The hot plasma then cools down to the temperature of the surrounding material by heat dissipation, (i.e. phonon transport). The free electron binds the free hole into a bound state (not recombination) – the exciton [33]. The exciton binding energy is 80 meV. At higher temperatures, the lattice provides enough energy to excite the electron from the exciton state back to the conduction band. At lower temperatures, however, the exciton lifetime increases, which means that it will take a longer time for the electrons to get re-excited to the conduction band. The re-excitation lifetime at room temperature is  $\sim 30 \text{ ps}$ , increasing to  $\sim 150 \mu\text{s}$  at 50 K [28]. This means that some of the bound electrons will not even start drifting

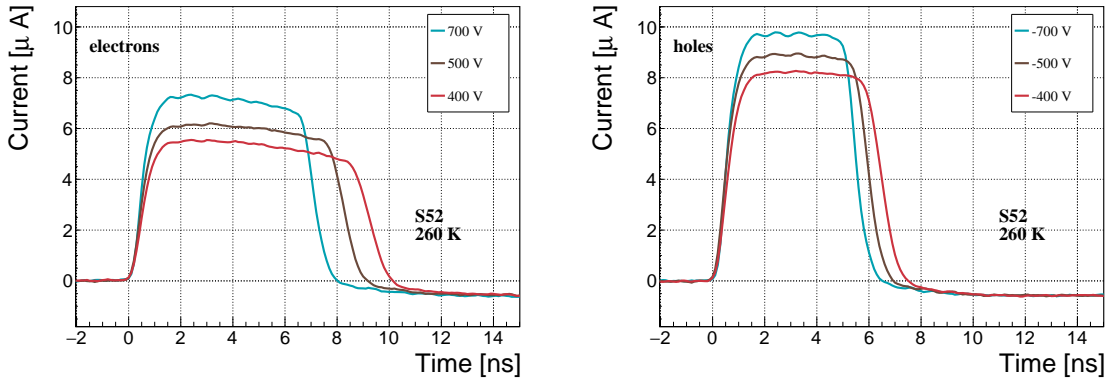


Figure 3.13: Varied bias voltage at a fixed temperature

1487 within the period of  $\sim 10$  ns, which is the expected carrier drift time. When they  
 1488 are finally freed, the current they induce is already hidden in the electronics noise.  
 1489 The effective area of the observed current pulse is therefore smaller than that of a  
 1490 pulse induced by all the carriers drifting at the same time. This in effect reduces the  
 1491 measured collected charge. The longer the time constant, the lower the measured  
 1492 collected charge, as shown in figure 3.17 below.

### 1493 3.4.1 Temperature-variant $\alpha$ -TCT before irradiation

1494 Three sCVD diamond samples have been tested at a range of temperatures using  
 1495 the  $\alpha$ -TCT technique. At each temperature point, the bias voltage is set to several  
 1496 positive and negative values. A set of 300 pulses is recorded at every data point  
 1497 and averaged offline. The resulting averaged pulses of sample S37 at the 260 K  
 1498 temperature point and a bias voltage of  $\pm 400$  V,  $\pm 500$  V and  $\pm 700$  V are shown in  
 1499 figure 3.13. The pulses induced by holes as charge carriers are shorter than those  
 1500 induced by electrons, which means that holes travel faster in diamond. The area of  
 1501 the pulse, however, is the same for both polarities, which corresponds to the fact that  
 1502 the same amount of charges is drifting in both cases.

1503 Figure 3.14 shows pulses at a bias voltage set to  $\pm 500$  V across the range of  
 1504 temperatures between 4 K and 295 K – room temperature (RT). Several conclusions  
 1505 can be drawn by observing their shape. First, the pulse shapes change with decreasing  
 1506 temperature. The pulse time gets shorter, hinting at the faster carrier drift velocity  
 1507  $v_{\text{drift}}$ . Second, between 150 K and 75 K there is a significant change in shape - the  
 1508 time constant of the rising edge increases significantly and the pulse area decreases.  
 1509 From 75 K down to 4 K there is no significant observable change. Last, the top of  
 1510 the pulse at the S52 is not flat, which means that a portion of the drifting charge is  
 1511 lost along its way. This is due to charge trapping, likely by means of crystal defects  
 1512 or impurities.

### 3.4. TEMPERATURE LIMITATIONS

---

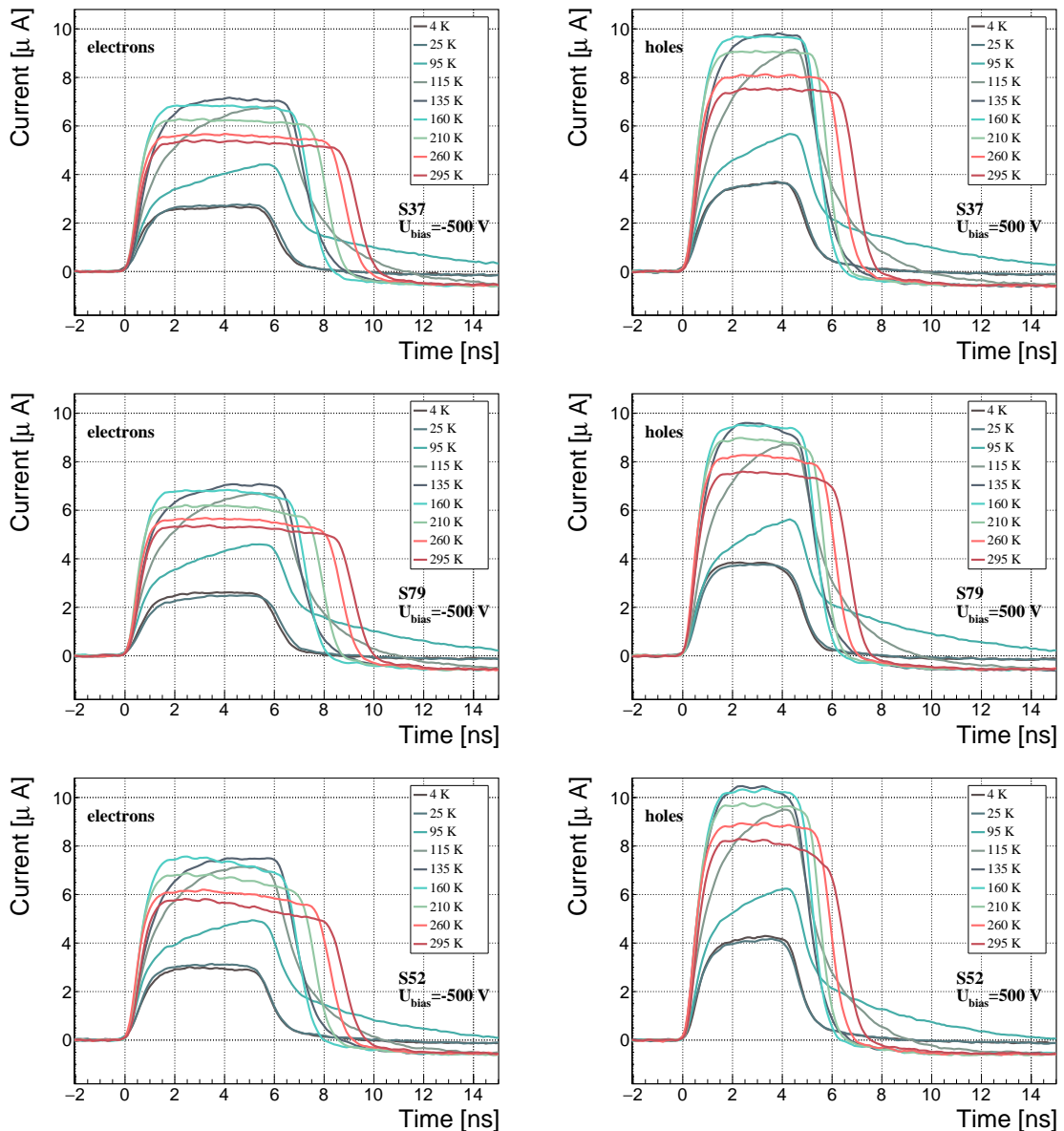


Figure 3.14: Several data points between 4 K and 295 K at a bias voltage of  $\pm 500 \text{ V}$

### 3.4.2 Temperature-variant $\alpha$ -TCT after irradiation

The irradiated S79 and S52 have been re-tested in the cryostat after irradiation. The aim was to see how their pulse shapes change with decreasing temperature, in particular the decaying top of the pulses (see figure 3.15). The decay time gives information on trapping of charge carriers while travelling through the diamond bulk. A variation of the decay time constant as a function of temperature might help to reveal the type and depth of the charge traps. To observe these effects or lack thereof, a number of requirements has to be met. First, the diamond samples are intentionally not primed prior to the experiment because priming would improve the pulse shapes and possibly change the decay time constant of the signal. Second, keeping in mind that the pulse shape of irradiated diamonds changes with time, the duration of the measurement of an individual data point has to be short – of the order of 30 seconds. Last, the sequence of the bias voltage settings is important, the reason for which is explained below.

Unfortunately it is not possible to avoid temporal pulse changes. For instance, one measurement point takes approximately one minute. After the measurement, the bias voltage polarity is swapped for a few seconds to bring the diamond back into its initial state. But a few seconds with respect to a minute is not enough. Therefore, when the bias voltage is set to the next value, there is still some residual effect of the previous measurement. Similar to the effects of polarisation, this effect is also decreasing the pulse height. This can be observed in figure 3.15, which shows the resulting pulses of S52 for bias voltages of  $\pm 200$  V,  $\pm 300$  V,  $\pm 400$  V and  $\pm 500$  V at 230 K and 260 K. In this case the measurements sequence is: 230K (200 V, 300 V, 400 V, 500 V, -500 V, -400 V, -300 V), 260 K (-200 V, -300 V, -400 V, -500 V, 500 V, 400 V, 300 V). The changes in pulse shapes for holes at 230 K and 260 K cannot be attributed to the temperature change. Instead, the explanation could lie in diamond “polarisation”. This means that, when exposed to an electric field with  $\alpha$  measurements ongoing, the diamond builds up an internal electric field of inverse polarity, which effectively reduces the overall electric field. This internal field does not dissipate when the external bias voltage is switched off. It can be said that the diamond becomes “polarised”. When switching the polarity of the external bias voltage, the internal and external electric field point in the same direction at the beginning, increasing the overall electric field and with it the pulse height. In figure 3.15, this happens when switching from 500 V (figure 3.15a) to -500 V (figure ??) at 230 K. The built up polarisation contributes to the pulse having a sharp rising edge and a high amplitude. This effect decays during the next two voltage points. There would be a handful of ways to avoid this polarisation effect in the data:

1. After every data point invert the bias voltage and leave it to return to a neutral state for the same amount of time,
2. Make a hysteresis of data points, going from minimum negative to maximum positive bias several times,

### 3.4. TEMPERATURE LIMITATIONS

---

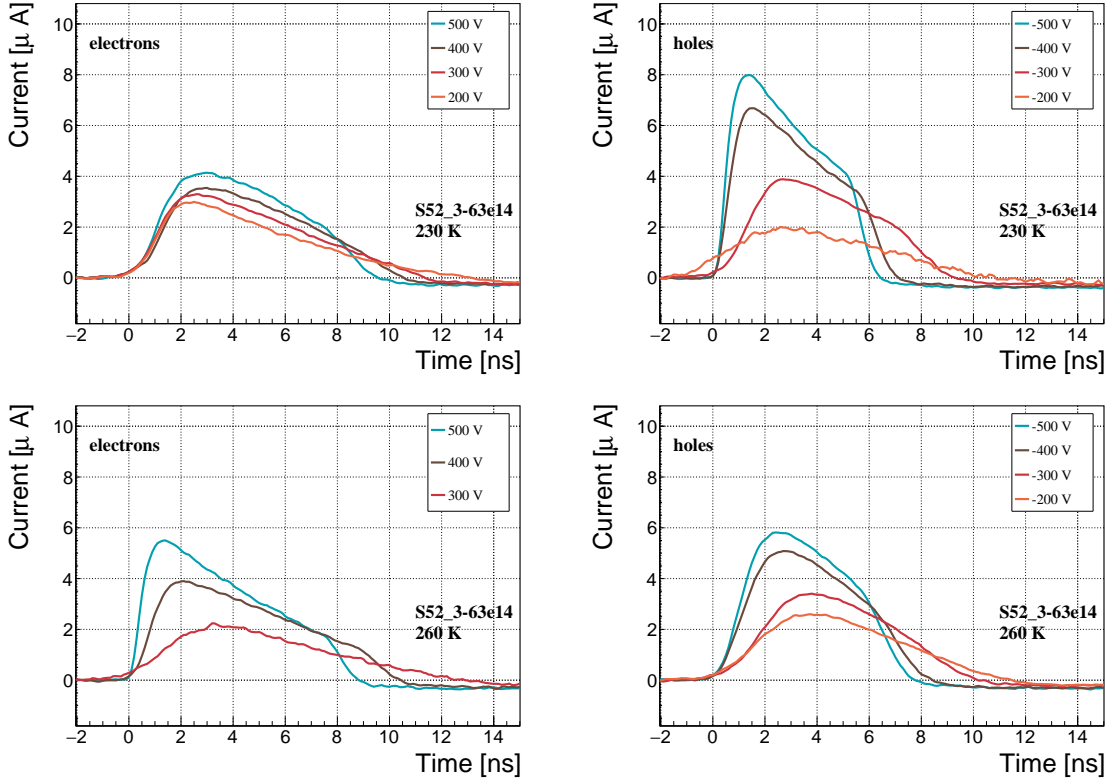


Figure 3.15: Varied bias voltage at a fixed temperature for an irradiated sample

1555        3. Reduce the measurement time at every bias voltage setting.

1556        Unfortunately, options (1) and (2) are very time consuming and would increase the  
 1557        overall experiment time to over one day. The third option would worsen the resulting  
 1558        averaged pulses. In the end an alternative option was chosen: alternating the start-  
 1559        ing bias voltage and the sequence at every temperature point. With this option, a  
 1560        meaningful systematic error in analysing the pulse shapes can be attained.

1561        Figure 3.16 shows the irradiated S52 and S79 as well as the non-irradiated S37  
 1562        for comparison, all at a bias voltage of  $\pm 500$  V and at several temperature points  
 1563        between 4 K and RT. It is evident that the radiation damage affected the shape of  
 1564        the pulses across all temperatures.

#### 1565        3.4.2.1 Collected charge as a function of temperature

1566        The area below the current pulse is proportional to the charge collected by the dia-  
 1567        mond detector. The collected charge is observed as a function of temperature. First,  
 1568        the amplitude values of the averaged pulses at a bias voltage of  $\pm 500$  V and across the  
 1569        temperature range between 4 K and 295 K have to be integrated. Then a calibration  
 1570        factor is used to derive the charge for all data points. This factor is obtained using  
 1571        a Cx charge-sensitive amplifier. The resulting values for electrons and holes are plot-  
 1572        ted in figures 3.17a and 3.17b, respectively. Thesis [28] gives a model that explains

**CHAPTER 3. EXPERIMENTAL RESULTS**  
**DIAMOND IRRADIATION STUDY**

---

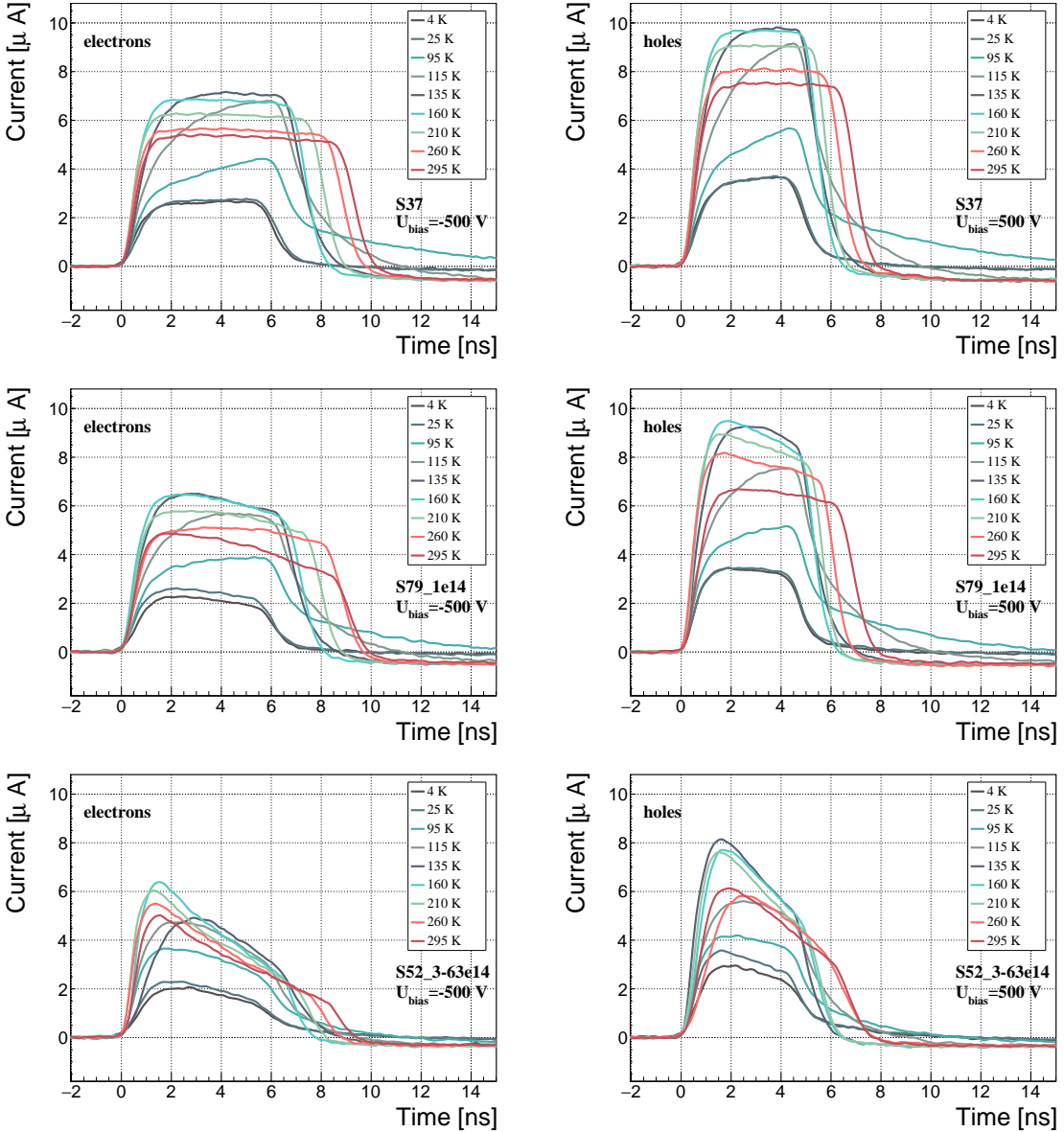


Figure 3.16: After irradiation: several data points between 4 K and 295 K at a bias voltage of  $\pm 500$  V

1573 the drop in charge below 150 K. The new contribution are the data points for the  
 1574 irradiated samples. The values for them are lower than the those of non-irradiated  
 1575 samples, which is expected.

1576 The values for all samples are fairly stable in the range between 4 K and 75 K  
 1577 and between 150 K and 295 K. However, in the values for the irradiated S52 some  
 1578 excursions can be observed. This is due to the sequence of the measurement steps,  
 1579 which introduced a hysteresis effect and is explained in the preceding text.

1580 The collected charge drops significantly from 150 K down to 75 K. In the non-  
 1581 irradiated samples the values in the lower temperature range are approximately 0.30

### 3.4. TEMPERATURE LIMITATIONS

---

of the values at the high range. For the irradiated ones this difference is lower – a factor of 0.35 for S79 and 0.5 for S52. An interesting detail is that the ratio between the values for non-irradiated samples and their irradiated counterparts at the lower range is different than at the higher range. Looking at the values for the electron collection in figure 3.17a: for S52 the lower ratio is equal to 1.28 and the higher equal to 1.7. For S79 these ratios are 1.00 and 1.09, which means that the difference in charge collection between 4 K and 75 K before and after irradiation is negligible.

#### 3.4.2.2 Charge trapping

The carriers drifting through the bulk get stopped by the charge traps with a certain probability. This trapping happens uniformly throughout the diamond, decreasing the number of carriers in the charge cloud. Therefore the absolute number of trapped carriers decreases. At the same time the absolute number of trapped carriers per unit of length decreases. The resulting function for the number of drifting carriers per unit of length is a decaying exponential function:

$$I(t) = I(0) \cdot e^{-\frac{t-t_0}{\tau}} + I_0, \quad (3.6)$$

where  $I(0)$  is the initial induced current,  $I_0$  is the end current,  $t$  is time,  $t_0$  is temporal displacement of the pulse and  $\tau$  is the decay time constant. This value tells how long it takes before the amplitude of the pulse decreases to 63 % of its initial height.

The decaying exponential function has been fitted to the decaying top of the averaged pulses at bias voltages of  $\pm 400$  V and  $\pm 500$  V across all temperatures excluding the transitional range between 75 K and 150 K. The resulting decay time constants  $\tau$  for an individual temperature point are not equal, which stems from the fact that the pulses change with time due to “polarisation”. This counts as a systematic error. Therefore the fitted  $\tau$  for  $\pm 400$  V and  $\pm 500$  V are averaged into one value representing the measurement at that temperature point. Figure 3.18a shows the fitted  $\tau$  for the five samples between 4 K and 295 K. In principle, the time constants should be infinite for a perfect and non-irradiated sample. Here a slightly tilted top of the pulse due to space charge is already successfully fitted with an exponential function, resulting in a  $\tau$  of the order of  $(200 \pm 20)$  ns<sup>-1</sup>. Consequently the fitting method is not adequate for non-irradiated samples. For the irradiated samples, the fit becomes increasingly more meaningful. As seen in figure 3.18a, the fitted values of the irradiated samples are fairly stable across all temperatures. There is a slight increase in the decay time constant of the S52 from  $(6.0 \pm 0.5)$  ns<sup>-1</sup> above 150 K to  $(8.5 \pm 0.9)$  ns<sup>-1</sup> below 75 K. On the other hand, this step is not observable in the S79 data. With only one sample exhibiting this behaviour, the effect is not significant enough. Judging by the data acquired, the samples would need to be irradiated to doses above  $1 \times 10^{14} \pi \text{ cm}^{-2}$  to quantify this effect in detail. So far this effect will not be regarded as significant for the scope of this thesis. Building on this assumption, the conclusion is that the signal decay time constant for irradiated sCVD diamond is constant across the temperature range between 4 K and 195 K, excluding the transitional range between 75 K and 150 K.

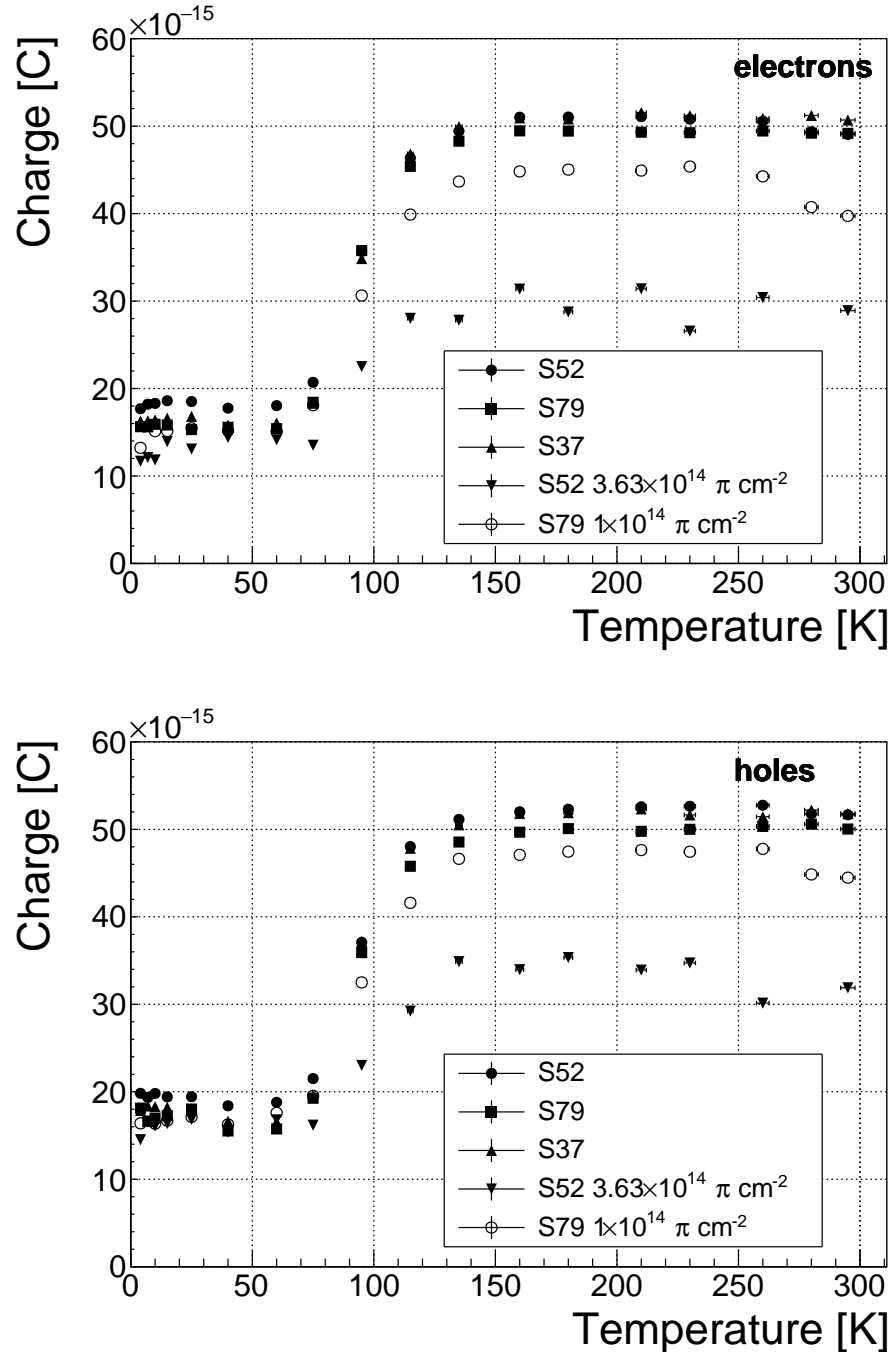


Figure 3.17: Collected charge as a function of temperature

1622 Taking into account the conclusions above, all the values can be averaged into one  
 1623 decay constant. Figure 3.18b shows these values for all samples as a function of the  
 1624 received  $\pi_{300 \text{ MeV}}$  radiation dose. To estimate the carrier lifetime with respect to the  
 1625 radiation dose received, a similar model is used than that in section 3.5. This model  
 1626 states that the inverse of the carrier lifetime is linearly decreasing with increasing

### 3.4. TEMPERATURE LIMITATIONS

1627 radiation dose:

$$\frac{1}{\tau} = \frac{1}{\tau_0} + \kappa_\tau \cdot \Phi \quad (3.7)$$

1628

$$\tau = \frac{\tau_0}{\kappa_\tau \tau_0 \Phi + 1} \quad (3.8)$$

1629 where  $\tau_0$  is the lifetime for a non-irradiated sample (real lifetime, therefore of the order  
1630 of  $400 \text{ ns}^{-1}$ ),  $\tau$  is the lifetime of an irradiated sample,  $\Phi$  is the received radiation dose  
1631 and  $\kappa_\tau$  the lifetime degradation factor. For these data the fitted factor is equal to  
1632  $\kappa_\tau = (3.6 \pm 0.8) \times 10^{-16} \text{ s cm}^2 \pi_{300 \text{ MeV}}^{-1}$ . Using this factor, the steepness of the decay  
1633 in the pulse shape with respect to radiation dose can be estimated. This can help  
1634 when designing a system where current pulse shape is an important factor.

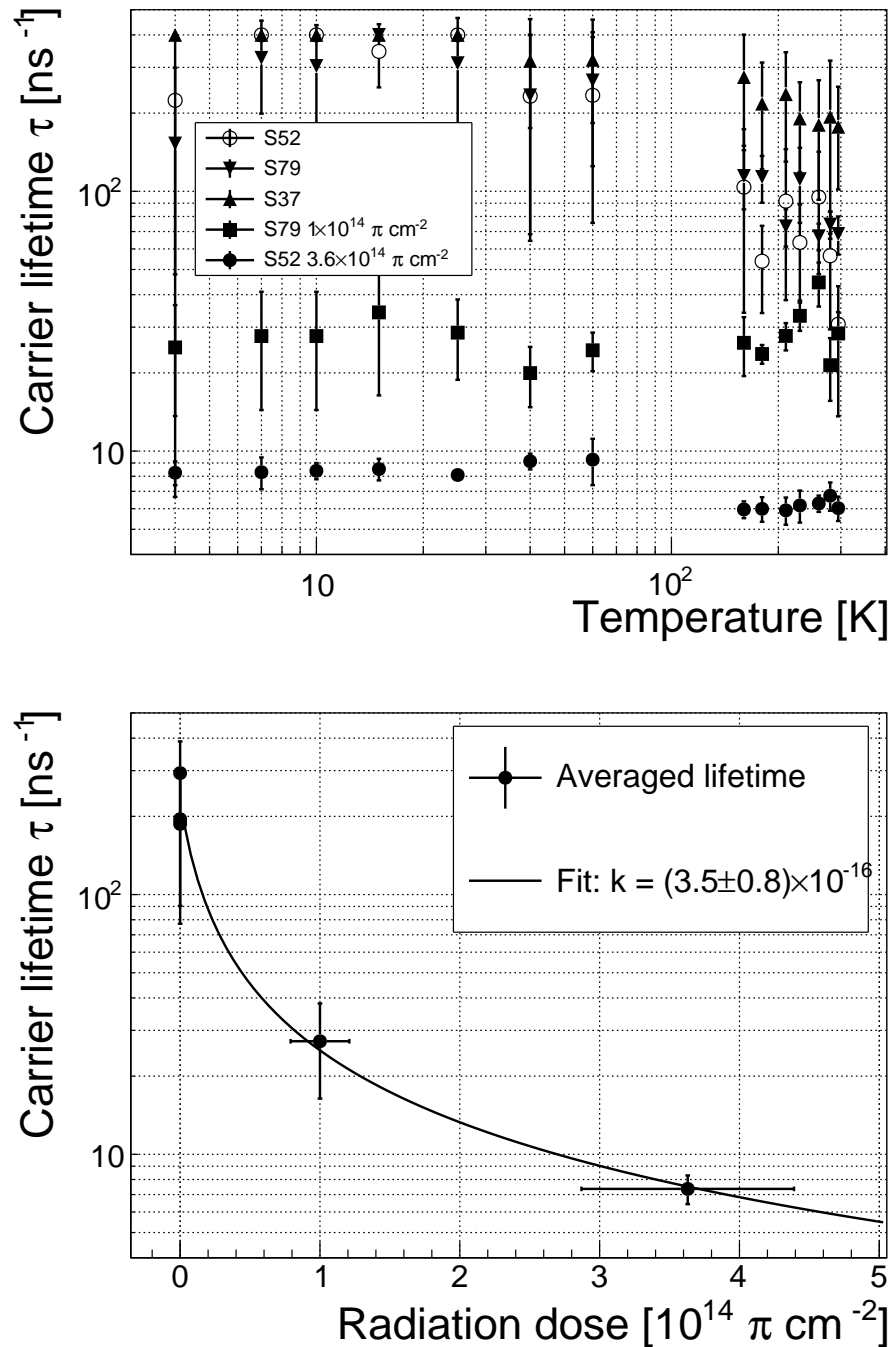


Figure 3.18: Charge carrier lifetime decreases with irradiation, but is stable across the range of temperatures between 4 K – 75 K and 150 K – 295 K. The first figure shows the carrier lifetime as a function of temperature whereas the second figure depicts the carrier lifetime averaged over all temperatures and plotted against the  $\pi$  irradiation dose

### **3.5. CONCLUSION**

---

## **3.5 Conclusion**

1636 This chapter gives an overview of the capabilities and limitations of diamond as  
1637 a particle detector. Three effects on diamond were studied – noise, radiation and  
1638 temperature, the focus being on the latter two.

1639 Two sCVD diamond detectors were irradiated with 300 MeV pions. They were  
1640 tested alongside a non-irradiated sample to observe the changes in the ability to detect  
1641  $\alpha$ ,  $\beta$  and  $\gamma$  radiation. Their charge collection efficiency was measured in a test beam  
1642 facility using . The results were compared to the results from the RD42 collaboration  
1643 and a DPA model. A radiation damage factor  $k_\lambda = (3.0 \pm 1.0) \times 10^{-18} \mu\text{m}^{-1} \text{cm}^{-2}$  was  
1644 obtained for  $\pi_{300 \text{ MeV}}$  particles. The data point was not in agreement with the data  
1645 provided by RD42 nor with the model. However, the irradiation process and the low  
1646 number of tested samples hold a relatively high statistical uncertainty. In addition,  
1647 there was no diamond surface treatment done in between the measurements, as is the  
1648 case in the study conducted by RD42. The results obtained in the course of these  
1649 measurements will also be fed into the existing pool of data in the RD42 collaboration.

1650 The next step was to test the long-term capabilities for  $\alpha$  detection. The shape  
1651 of the ionisation profile was investigated to determine the behaviour of the charge  
1652 carriers in the irradiated diamond. An exponential decay was observed in the pulses  
1653 of irradiated samples, proving that there are charge traps in the bulk that were created  
1654 during irradiation. Then a long-term stability test was carried out. The results show  
1655 that the irradiated diamond detectors do not provide a stable and reliable long-term  
1656 measurement of  $\alpha$  particles. This might be due to a space-charge build-up in the  
1657 bulk, which changes the electric field, affecting the charge carriers. A procedure to  
1658 improve the pulse shape using  $\beta$  and  $\gamma$  radiation was proposed.

1659 Finally, the diamond sensors were cooled down to temperatures between 4 K and  
1660 295 K. Their response to  $\alpha$  particles was observed. The results of the non-irradiated  
1661 and irradiated samples were compared. The effect of reduction for the number of  
1662 drifting charges due to exciton recombination was observed in both sets of data.  
1663 The second set had a superimposed effect of charge trapping during the drift, which  
1664 was represented by an exponential decay in the signal. The decay time constant  
1665 did not change with temperature. Therefore all temperature points for individual  
1666 samples were averaged and the decay time constants were plotted against the received  
1667 radiation dose. A damage factor equal to  $\kappa_\tau = (3.5 \pm 0.8) \times 10^{-16} \text{ s cm}^2 \pi_{300 \text{ MeV}}^{-1}$  for  
1668 non-primed diamonds was defined.

1669

# Chapter 4

1670

## Charge monitoring

1671

### *The ATLAS Diamond Beam Monitor*

1672 Particle detectors in high energy physics experiments need to meet very stringent  
1673 specifications, depending on the functionality and their position in the experiment.  
1674 In particular, the detectors close to the collision point are subject to high levels of  
1675 radiation. Then, they need to operate with a high spatial and temporal segmentation  
1676 to be able to precisely measure trajectories of hundreds of particles in very short  
1677 time. In addition, they need to be highly efficient. In terms of the structure, their  
1678 active sensing material has to be thin so as not to cause the particles to scatter  
1679 or get stopped, which would worsen the measurements. This also means that they  
1680 have to have a low heat dissipation so that the cooling system dimensions can be  
1681 minimised. Finally, they need to be able to operate stably for several years without  
1682 an intervention, because they are buried deep under tonnes of material and electronics.

1683 The material of choice for the inner detector layers in the HEP experiments is  
1684 silicon. It can withstand relatively high doses of radiation, it is highly efficient (of the  
1685 order of  $\sim 99.9\%$ ) and relatively low cost due to using existing industrial processes  
1686 for its production. Its downside is that, with increasing irradiation levels, it needs to  
1687 be cooled to increasingly low temperatures to ensure a stable operation. This is not  
1688 the case with diamond. In addition, diamond has a lower radiation damage factor,  
1689 which means it can operate in a radiation-heavy environment for a longer period.

1690 The ATLAS Diamond Beam Monitor (DBM) [] is a novel high energy charged  
1691 particle detector. Its function is to measure luminosity and beam background in the  
1692 ATLAS experiment. Given its position in a region with a high radiation dose, di-  
1693 amond was chosen as the sensing material. The monitor's pCVD diamond sensors  
1694 are instrumented with pixellated FE-I4 front-end chips. The pCVD diamond sensor  
1695 material was chosen to ensure the durability of the sensors in a radiation-hard envi-  
1696 ronment and the size of its active area. The DBM is not the first diamond detector  
1697 used in HEP, but it is the largest pixellated detector installed so far (see figure 4.1).  
1698 It was designed as an upgrade to the existing luminosity monitor called the Beam  
1699 Conditions Monitor (BCM) [] consisting of eight diamond pad detectors, which is

#### 4.1. LUMINOSITY MEASUREMENTS

---

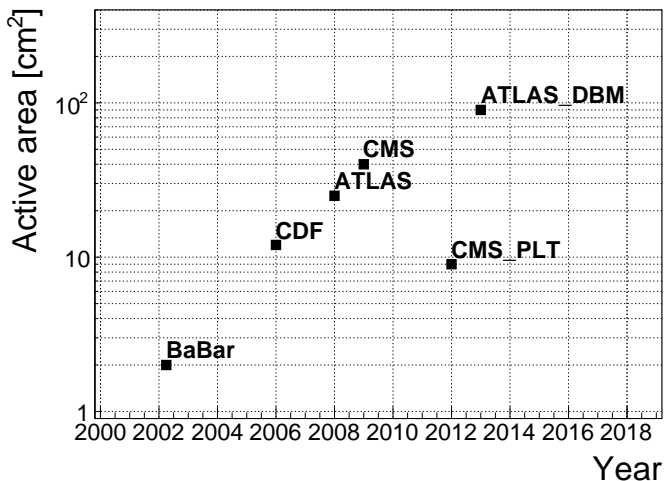


Figure 4.1: Diamond detectors installed in high-energy physics experiments in the last decade, sorted by the active sensor area. The first four detectors from the left are radiation monitors whereas the right two are pixel trackers.

able to perform precise time-of-flight (ToF) measurements. The DBM complements the BCM's features by implementing tracking capability. Its pixelated front-end electronics significantly increase the spatial resolution of the system. Furthermore, the DBM is able to distinguish particle tracks originating in the collision region from the background hits. This capability is a result of its projective geometry pointing towards the interaction region. This chapter first describes the principles of luminosity measurements. It then explains how the DBM will carry out this task. Finally, some results from tests and from the real collisions are presented.

When a particle traverses a sensor plane, a hit is recorded in the corresponding pixel. Thus, a precise spatial and timing information of the hit is extracted. With three or more sensors stacked one behind the other, it is also possible to define the particle's trajectory. This is the case with the DBM. Its projective geometry allows the particles to be tracked if they traverse the sensor planes. The DBM relates the luminosity to the number of particle tracks that originate from the collision region of the ATLAS experiment. Particles that hit the DBM from other directions are rejected as background radiation.

## 4.1 Luminosity measurements

Luminosity is one of the most important parameters of a particle collider. It is a measurement of the rate of particle collisions that are produced by two particle beams. It can be described as a function of beam parameters, such as: the number of colliding bunch pairs, the revolution frequency, the number of particles in each bunch and the transverse bunch dimensions. The first four parameters are well defined. However, the transverse bunch dimensions have to be determined experimentally

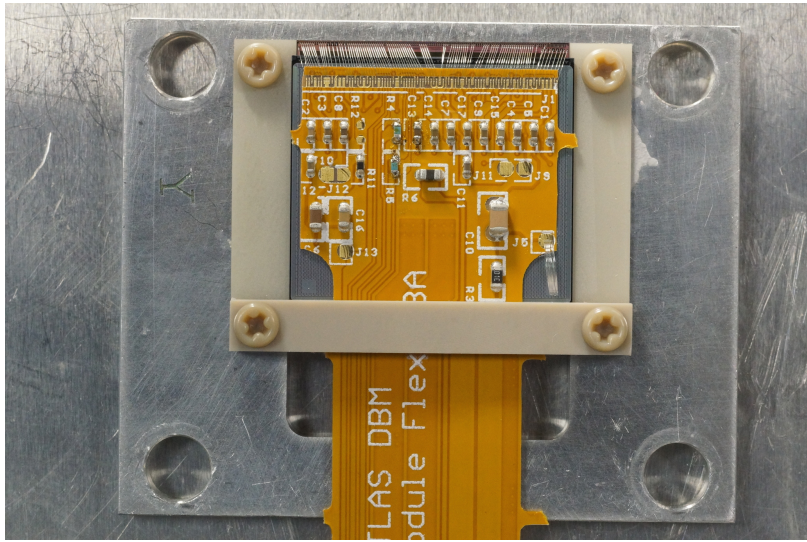


Figure 4.2: DBM module, top-down view. Visible is the flexible PCB with signal and power connections, the silicon sensor and a part of the FE-I4. Wire bonds from the PCB to the FE-I4 and to the sensor are also visible.

1723 during calibration. The ATLAS experiment uses the *van der Meer scan* [] during  
1724 low-luminosity runs to calibrate the luminosity detectors. This scan is performed  
1725 by displacing one beam in a given direction and measuring the rate of interactions  
1726 as a function of the displacement. Transverse charge density of the bunches can be  
1727 estimated on the basis of the interaction rate. The calibrated luminosity detectors  
1728 can then operate during high-luminosity runs.

1729 One approach to luminosity monitoring is to count the number of particles pro-  
1730 duced by the collisions. The luminosity is then proportional to the number of detected  
1731 particles. A detector has to be capable of distinguishing individual particles that fly  
1732 from the interaction point through the active sensor area. If the detector has at least  
1733 three layers, it can reconstruct the particles' tracks, which in turn yields more infor-  
1734 mation on the their trajectory. This is one reason why detectors with a high timing-  
1735 and spatial segmentation are more suitable for these applications. The second reason  
1736 is that, with a high spatial segmentation, the detector will not saturate even at high  
1737 particle fluencies.

## 1738 4.2 Diamond pixel module

1739 The two most important parts of the diamond pixel module (seen in figure 4.2) are  
1740 the sensor, which detects ionising radiation, and the pixellated front-end chip, which  
1741 collects the ionised charge with a high spatial segmentation, processes the recorded  
1742 data and sends them to the readout system. This section describes these two main  
1743 parts of the module and their interconnection.

## 4.2. DIAMOND PIXEL MODULE

---



Figure 4.3: A pCVD wafer. The golden dots on the surface are the electrodes that are applied during the qualification test. The wafer is measured across the surface to find the regions with the highest efficiency.

### 1744 4.2.1 Sensors

1745 The DBM modules are instrumented with two types of sensors – pCVD diamond and  
1746 silicon. The silicon sensors are used as a fallback solution because there were simply  
1747 not enough high-quality diamond sensors available. In addition, a comparative study  
1748 of irradiation damage between silicon and diamond can be made with such a hybrid  
1749 system.

1750 **Diamond sensors** The target material for this application is pVCD diamond. The  
1751 reason for this is that the active area of an individual sensor must be approximately  
1752  $4 \text{ cm}^2$ , which is too large for the sCVD diamond. pCVD material is also a bit  
1753 cheaper, which makes a detector with a large active area more feasible to build. The  
1754 material is provided by three companies: DDL, E6 and II-IV and it is grown in  
1755 15 cm wafers, as seen in figure 4.3. The target thickness of the wafers is 500  $\mu\text{m}$  and  
1756 the minimum required charge collection efficiency is 40 % ( $\text{CCD} \geq 200 \mu\text{m}$ ). They  
1757 need to be operated at bias voltages between 600–1000 V. On one side there is a  
1758 single gold electrode applied across the whole surface. On the other side a pixellated  
1759 metallisation is added.

1760 **Silicon sensors** are standard  $n^+ - in - n$  planar sensors with a 200  $\mu\text{m}$  thickness  
1761 and were mostly fabricated at CiS [], a company from Ertfurt, Germany. They are  
1762 designed to have nearly a 100 % efficiency when non-irradiated. Their bulk resistivity  
1763 is between 2–5  $\text{k}\Omega\text{cm}$  and they were diffusion oxygenated at 1150 °C for 24 hours to

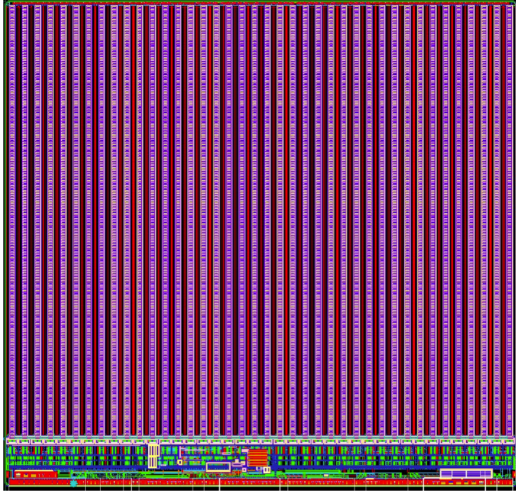


Figure 4.4: FE-I4 layout, top-down view. The pink area are pixels grouped into columns, the green area below is the common logic and the red strip at the bottom are the wire bond pads.

1764 increase their radiation hardness. One side is segmented into pixels. Guard rings at  
1765 the edges of the sensor provide a controlled drop in potential, reducing the possibility  
1766 of shorts at maximum design bias voltages of the order of 1000 V.

### 1767 4.2.2 Front-end electronics

1768 The FE-I4 (front-end version four) [] is an ASIC pixel chip designed specifically for  
1769 the ATLAS pixel detector upgrade. It is built as a successor to the current pixel chip  
1770 FE-I3, surpassing it in size of the active area ( $4\times$  larger) as well as the number of  
1771 channels/pixels ( $10\times$  more). 336 such FE-I4 modules are used in the newly installed  
1772 pixel layer called the Insertable B-Layer (IBL) []. The DBM is also instrumented  
1773 with these chips. The FE-I4's integrated circuit contains readout circuitry for 26880  
1774 pixels arranged in 80 columns on a  $250\text{ }\mu\text{m}$  pitch and 336 rows on a  $50\text{ }\mu\text{m}$  pitch. The  
1775 size of the active area is therefore  $20.0\times16.8\text{ mm}^2$ . This fine granularity allows for a  
1776 high-precision particle tracking. The chip operates at 40 MHz with a 25 ns acquisition  
1777 window, which corresponds to the spacing of the particle bunches in the LHC. It is  
1778 hence able to correlate hits/tracks to their corresponding bunch. Furthermore, each  
1779 pixel is capable of measuring the deposited charge of a detected particle by using  
1780 the Time-over-Threshold (ToT) method. Finally, the FEI4 has been designed to  
1781 withstand a radiation dose up to 300 MGy. This ensures a longterm stability in the  
1782 radiation hard forward region of the ATLAS experiment.

1783 Each pixel is designed as a separate entity. Its electrical chain is shown in figure  
1784 4.5. The bump-bond pad – the connection to the outside of the chip – is the  
1785 input of the electrical chain, connected to a free-running amplification stage with ad-  
1786 justable shaping using a 4-bit register at the feedback branch. The analog amplifier is  
1787 designed to collect negative charge, therefore electrons. The output is routed through

## 4.2. DIAMOND PIXEL MODULE

---

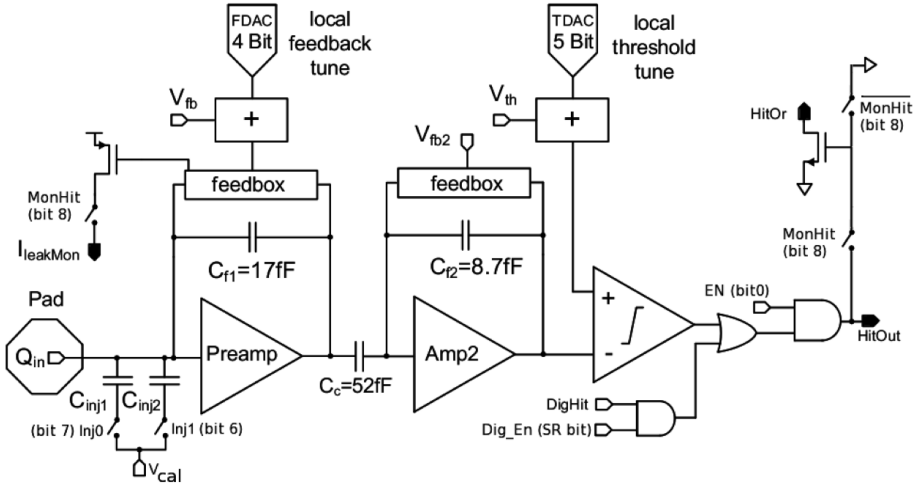


Figure 4.5: Schematic of an analog pixel. Courtesy of the FE-I4 collaboration.

a discriminator with an adjustable threshold. This value in effect defines the level at which the circuit will detect a hit. In addition, there is a counter of the clock cycles (25 ns sampling) during which the signal is above the discriminator threshold. The value of the counter is proportional to the collected charge. The logic gates at the end of the chain are used to enable/disable the pixel and to issue a so-called HitOr flag – this signal is set whenever at least one of the pixels was hit and is used as a trigger for the readout. The output of the chain – HitOut – is routed into the logic of the chip where it is buffered and eventually sent out to the readout system. The module receives all its commands from the system via a 40 MHz LVDS line. The commands are either settings for the pixel registers or triggers that start the data readout. The data are sent via an LVDS line at up to 320 Mbit/s, but by default at 160 Mbit/s, four times faster than the clock of the device. This allows the chip to clear out its buffers before new data are recorded, thus avoiding dead time and data pile-up. The FE-I4 has been successfully tested for trigger rates of up to 300 kHz.

The DBM uses pCVD diamond with  $d_C = 500 \mu\text{m}$  thickness and silicon with  $d_{Si} = 200 \mu\text{m}$  thickness as a sensor material. The resulting most probable value (MPV) of the deposited charge for a minimum ionising particle (MIP) is calculated with the formula  $Q_s = d \cdot E_{e-h}$  and equals 18000 electrons and 17800 electrons, respectively, at a full charge collection efficiency. Unfortunately this is not the case with the pCVD material, whereby the expected charge collection efficiency is of the order of 50 % – around 9000 e. This value further decreases with received irradiation dose. Therefore in order to detect the particles depositing energy on the far left side of the landau spectrum, the threshold has to be set to a significantly lower value. On the other hand, if the threshold set too low, it also detects the electronic noise and stores a false noisy hit. With the typical noise amplitudes being in the range of 120–200 e, a safe threshold range would be between  $Th = 1000\text{--}3000$  e. The target for the DBM is to lower the threshold down to 800 e.

The analog amplifier is implemented in two stages to get a fast rise time at a low noise and a low power consumption. The output signal of the analog amplifier has a triangular shape with a fast rise time and a long decay. The shape can be adjusted by tuning the amplifier feedback loop. Its length is proportional to the collected charge, but it needs to be calibrated first. This is done by means of two injection capacitors,  $C_{\text{inj}1}$  and  $C_{\text{inj}2}$ , seen in figure 4.5 with well defined capacitances. First, the charge  $Q_{\text{cal}} = V_{\text{cal}} \cdot (C_{\text{inj}1} + C_{\text{inj}2})$  is injected into the analog chain. Then the length of the output pulse is measured and finally the feedback value is changed to either lengthen or shorten the pulse in order to get to the required duration  $t_{\text{cal}}$ . The typical values are  $Q_{\text{cal}} = 5000 - 16000$  e at the time  $t_{\text{cal}} = 5 - 10$  ToT. The target values depend on the sensor, the type of a radioactive source and the application. Therefore the initial threshold  $Th$  at 1 ToT and the calibrated value  $Q_{\text{cal}}$  at  $t_{\text{cal}}$  ToT give us a linear scale of collected charge with respect to time over threshold. However, in practice this relation is nonlinear for lower thresholds, but since the goal of the measurements is to track the particles rather than to measure their deposited energy precisely, this is sufficient.

## 4.3 Module assembly and quality control

Parts for the detector arrived separately and were assembled into modules at CERN’s DSF lab after being checked for production faults. The assembled modules underwent a series of quality control (QC) and burn-in tests to determine their quality, efficiency and long-term stability.

### 4.3.1 Assembly

A single-chip module consists of a pixel module, a flexible PCB and the supporting mechanics (a ceramic plate and an aluminium plate). The chip arrives already bump-bonded to the sensor, be it diamond or silicon. First it is glued to the ceramic plate on one side and to the PCB on the other using either Araldite 2011 or Staystik 672/472. The choice of glue was a topic of a lengthy discussion. Staystik is re-workable and has a very high thermal conductivity. The latter is important because the FE-I4 chips tend to heat up significantly and need a good heat sink. The problem is that it has a curing temperature of 160/170 °C. This temperature may cause some unwanted stress build-up between the FE-I4 and the diamond sensor due to different coefficients of thermal expansion, pulling them apart. This would disconnect the pixels, yielding large regions of the module insensitive to radiation. To avoid this, an alternative glue was tried. Araldite 2011 can be cured at lower temperatures – down to RT – but it has a lower heat conductivity. In the end Araldite is used as the safer option. However, due to the longer curing, the whole assembly process using Araldite is extended to two working days. After curing, the module is wire-bonded and attached to the aluminium plate using screws made up of a radiation-resistant PEEK plastic. They have to be tightened with a great care, because their screw head is only 0.2–0.6 mm

#### 4.3. MODULE ASSEMBLY AND QUALITY CONTROL

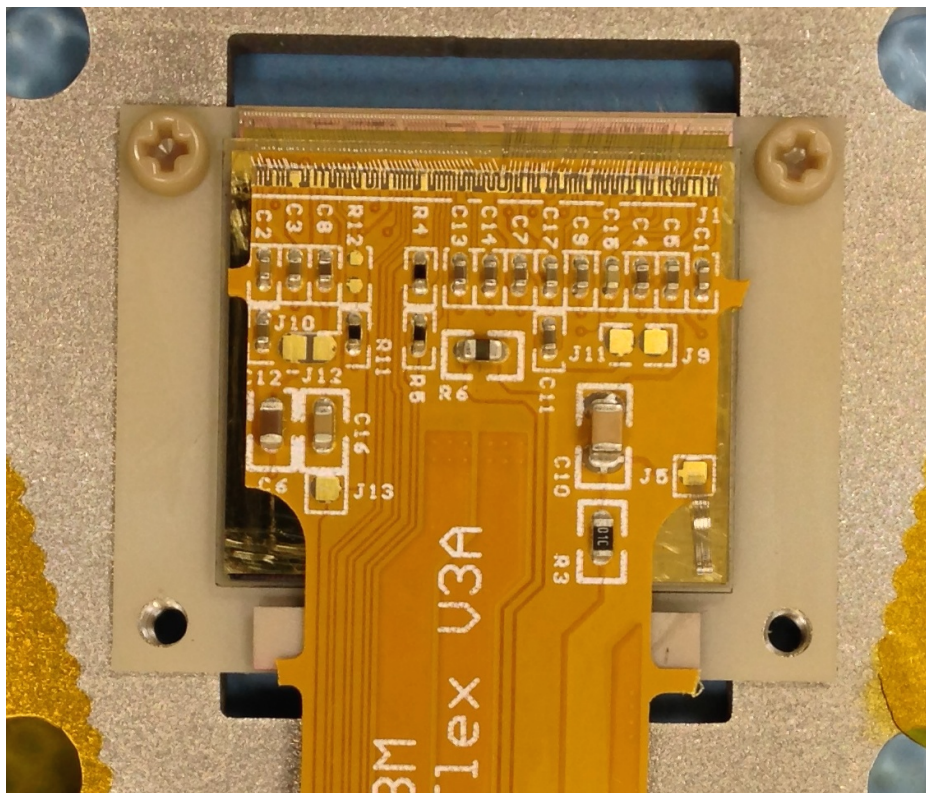


Figure 4.6: An assembled DBM module

away from the sensor edge – the sensor displacement tolerance during gluing is of the order of 0.5 mm. Finally, the module is put in an aluminium carrier which protects it from mechanical damage or electrostatic discharges. Figure ?? shows an assembled module.

### 1858 4.3.2 Testing

1859 The modules are tested in the lab using an RCE readout system and a moving stage  
1860 with two degrees of freedom. They are placed onto the stage and connected to the  
1861 readout system and the power supplies. After ensuring the low- and high voltage  
1862 connectivity they are checked for the signal connectivity. If everything is operational,  
1863 a series of automated tests is run. Each of these tests calibrates a certain value within  
1864 a pixel, whether it is the signal threshold or the value for integrated charge. These  
1865 are tuned in a way that the response to a predefined calibration signal is uniform for  
1866 all pixels across the sensor. This procedure is referred to as *tuning*.

When the modules are tuned, they are tested using a  $^{90}\text{Sr}$  radioactive source. Two things are checked: 1) operation of all pixels and 2) sensor efficiency. The first test is carried out by moving the module slowly under the source while taking data so that the whole surface is scanned uniformly. The resulting occupancy map reveals any pixels that are not electrically coupled to the sensor via bump bonds. This is an important step in the DBM QC procedure, because it turned out that a significant

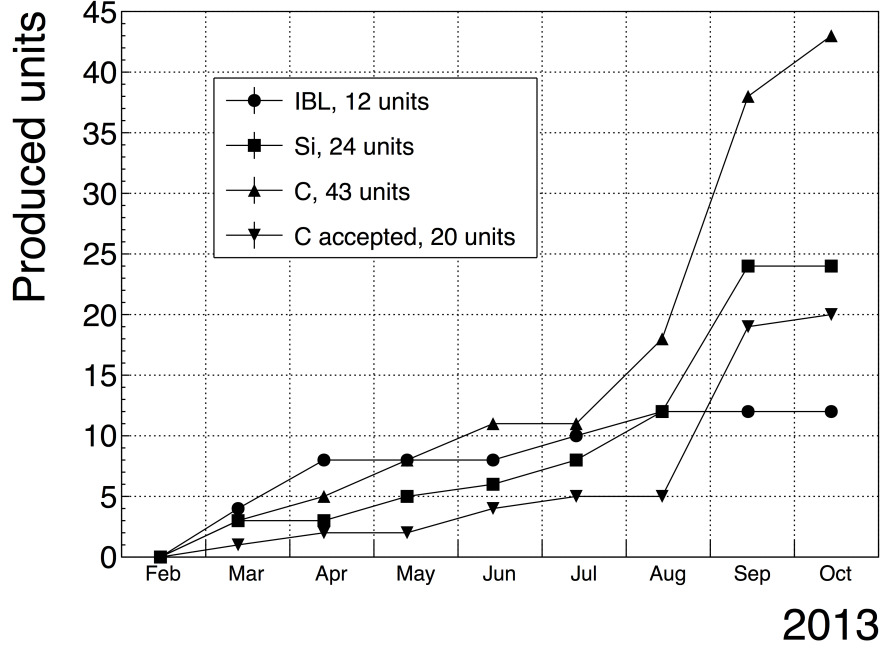


Figure 4.7: Module production with time

portion of the flip-chipped diamond sensors exhibited very poor connectivity. The disconnected regions on the faulty modules ranged anywhere from 0.5–80 % of the overall active surface. In two cases the sensor was even completely detached from the chip. Therefore the pixel connectivity turns out to be the most important qualification factor in the QC procedure. Unfortunately the only way to check it at the moment is to fully assemble a module and test it using a radioactive source. If the module turns out to be of poor quality, it is disassembled and sent for rework. The turnover time of this operation is of the order of one month, which affected the DBM installation schedule significantly.

Only the modules that passed the pixel connectivity test undergo the second test stage in which the sensor’s efficiency was estimated. A scintillator is placed underneath the module and is used as a trigger. A particle that crosses the DBM module and hits the scintillator, triggers the module readout. In the end, the number of triggers is compared to the number of hits/clusters recorded by the module. The resulting ratio gives an estimate of the sensor’s detection efficiency. The real sensor efficiency can only be measured in a particle beam and using a beam telescope as a reference detector. Nonetheless, the *pseudo-efficiency* gives a rough estimate of the sensor’s quality.

The results for the DBM QC are shown in section 4.4. All in all, 79 modules went through the QC procedure – 43 diamond modules and 36 silicon modules, 12 of the latter only for testing purposes. Figure 4.6 shows their production with time. 18 diamond modules and 6 silicon modules were in the end chosen to be made up into DBM telescopes and installed into ATLAS.

### **4.3. MODULE ASSEMBLY AND QUALITY CONTROL**

---

A very important issue is the so called erratic current. This term describes the leakage current in a pCVD diamond that becomes unstable. It can develop gradually or can be triggered with a  $\beta$  source. Spikes appear in the otherwise stable leakage current. They can be up to three orders of magnitude higher than the base current. Sometimes the current also suddenly increases for a few orders of magnitude and stays at that level (e.g. from the initial 1 nA to 3  $\mu$ A). The amplitude differs in magnitude from sensor to sensor. This effect is still not fully explained, but the hypothesis is that the charges find a conductive channel along the grain boundaries, causing discharges. These discharges are picked up by the pixel amplifiers in the FE-I4. A single discharge can trigger a group of up to  $\sim$ 500 pixels, resulting in a *blob* on the detector occupancy map. Sometimes the conductive channel stays in a conductive state, making one or more pixels always to fire. These pixels only use the bandwidth of the readout channel, so they have to be masked out during measurements.

#### **4.3.3 Installation and commissioning**

The DBM modules that passed the QC tests were assembled into telescopes – sets of three modules one behind the other with a spacing of 50 mm. Of the 18 diamond and 6 silicon modules, 6 diamond and 2 silicon modules were built. A special care was taken when choosing the sets of three diamonds. The modules with a similar pseudo-efficiency, leakage current, maximum stable high voltage and shape of disconnected regions were grouped together. After assembly into telescopes, the modules were tested for their connectivity. Then the high voltage was applied and the leakage current was observed. This was an important point to check because all three modules shared the same high voltage channel. Any instabilities on one of the modules would cause problems on the other two. This would for instance happen if one of the modules had a much lower breakdown voltage.

Due to time constraints, the telescopes were not built at the same time but instead the production was pipelined. As soon as two telescopes were ready, they were transported to Point 1 – the site where parts of the ATLAS detector were being put together. There they were prepared for installation onto the pixel detector structure that had been extracted from ATLAS due to pixel detector commissioning. The commissioning was nearing completion, so the technicians were preparing the detector for re-insertion. The cylindrical structure was being closed off by four new service quarter-panels (nSQPs). This meant that with every day the access to the place of installation of the DBM was more difficult. The first two telescopes were still put into place when only one nSQP was in place. This allowed the installation process to be carried out from both sides. This proved to be helpful, because the process was lengthy and had to be done with great precision. It involved tightening several screws on both sides of the telescopes, adding thermal paste on the aluminium joints and removing the protective covers, revealing the fragile wire bonds. At the same time the surrounding electronics and cables had to be left untouched. The lessons learnt with the first part of the installation were helpful when installing the other tele-

scopes. The last two were fitted onto the structure when three nSQPs were already in place, leaving only a narrow opening for access. The whole procedure was carried out blind. After every installation, the telescopes were tested again. First, the low voltage connectivity was checked and a set of tests was run on the FE-I4 front-end chips. An eye diagram was made to estimate the quality of the signal transmission. Then a  $^{90}\text{Sr}$  source was used to perform a source test on three modules at the same time. Leakage current was observed during the source test. The final test included running four telescopes (all on one side) at a time. All the tests were successful and the DBM was signed off.

## 4.4 Performance results

This section gives an overview of the performance results of the DBM modules achieved during the QC and the test beam campaign. The source tests were performed to check for disconnected regions in the sensors and to measure the diamond's pseudo-efficiency. Only the modules with minimal disconnected regions and maximum pseudo-efficiency were chosen for installation.

### 4.4.1 Source tests

All modules went through the same procedure when tested using a  $^{90}\text{Sr}$  source – to check for disconnected regions and to measure the pseudo-efficiency.

The setup consisted of a placeholder for the  $^{90}\text{Sr}$  source, an X-Y moving stage with a holder for the module and a scintillator with a photomultiplier placed below the source and the module. The scintillator was used as a trigger – when it detected a particle, it triggered the readout of the module. If the module was placed in between the source and the scintillator, the particle had to traverse the module to hit the scintillator. Therefore, in the case of a module with a 100 % efficiency the triggered data read out by the module would need to contain at least one hit in the module. In reality the  $\beta$  particles scatter around the setup and sometimes hit the scintillator from other directions, without incident the module. This produces empty triggers. The phenomenon sets the limitation of measuring with a radioactive source as compared to the measurements in a test beam, in which the particles in principle always travel in one direction and their scattering is minimal.

The test for disconnected regions was carried out by moving the module under the source in X and Y direction so that the exposure over the whole plane was uniform. This resulted in an occupancy scan seen in figures 4.7a and 4.7b. The silicon module had a very uniform occupancy plot. So much so that the features of the overlaying flexible PCB can be observed. The rectangular shadows are the passive components whereas the lines are the traces in the PCB. Furthermore, a circular-shaped edge of the PCB can be seen on the bottom right side of the plot. These darker areas are such because fewer electrons can penetrate the material with a high density. In the case of the diamond, the features of the PCB can be observed as well, but are much

#### 4.4. PERFORMANCE RESULTS

---

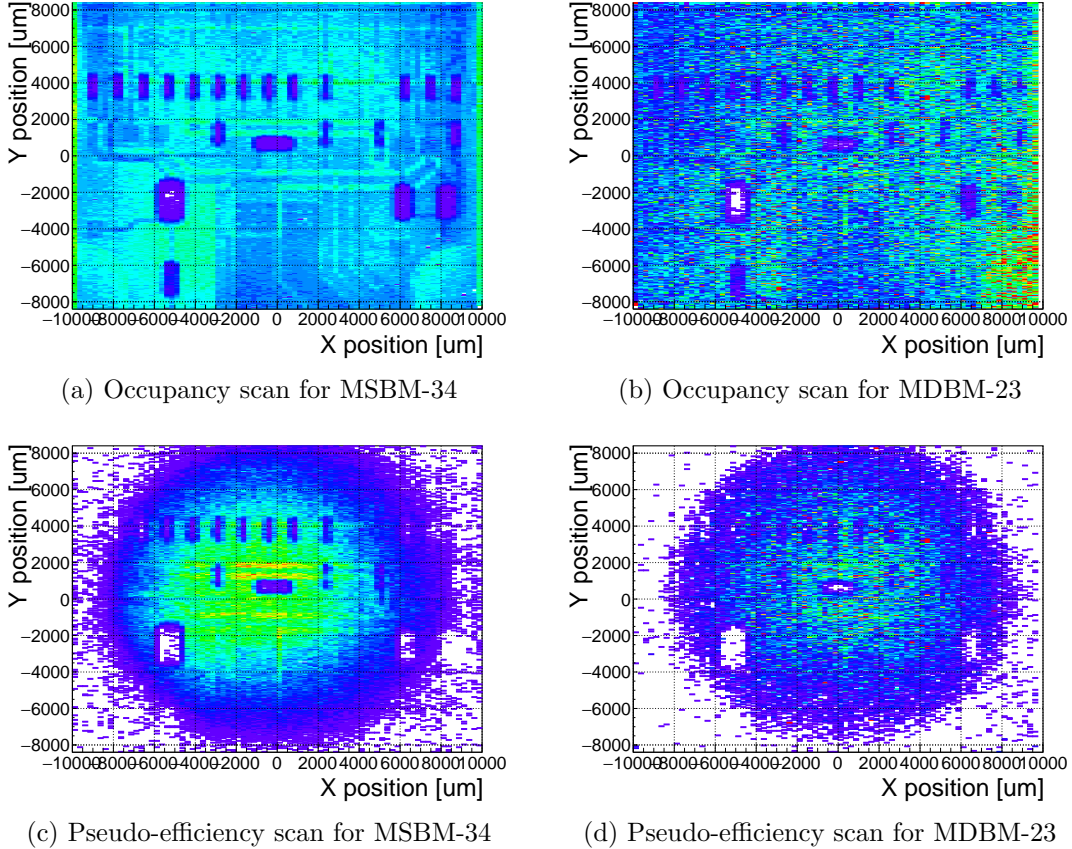
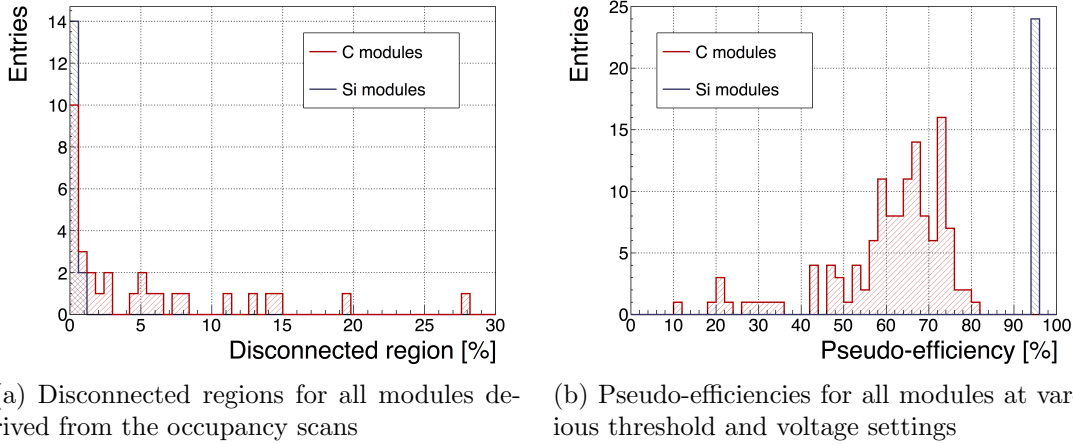


Figure 4.8: Occupancy and pseudo-efficiency scans for the silicon (left) and diamond sensor (right) to check for disconnected regions and estimate the sensor’s efficiency. Shadows of the electronic components are clearly visible because fewer electrons were able to traverse through such a higher amount of material.

less distinguishable. In principle, the plot is much more granulated – less uniform. This high variance in the diamond’s detection ability is due to the grain boundaries in the pCVD material which trap the drifting charges, rendering some regions much less efficient.

The pseudo-efficiency test was carried out by placing the module directly below the source and collimating the particles so that their trajectory was incident the module in the middle. For every trigger by the scintillator, a script checked whether there was a hit recorded in the module or not. The resulting ratio between the number of triggers and number of hits recorded in the module is a pseudo-efficiency – an estimation of the sensor’s efficiency. It cannot give a precise value due to the triggers produced by scattered particles, but at least gives a rough estimate.

Figure 4.8a shows the distribution of disconnected regions across all tested modules. Silicon modules were performing as expected, with a minimum number of disconnected pixels. The majority of the silicon modules yielded the pseudo-efficiency of  $(94.3 \pm 0.2)\%$ . Silicon sensors being 99.99 % efficient, this value was underesti-



(a) Disconnected regions for all modules derived from the occupancy scans      (b) Pseudo-efficiencies for all modules at various threshold and voltage settings

Figure 4.9: Measurements of pseudo-efficiency and disconnected regions for all modules that went through the QC procedure

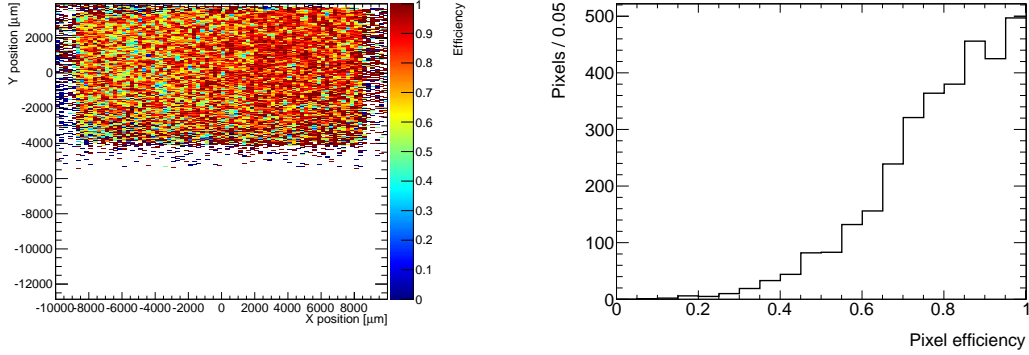
mated by about 5 %. The measured pseudo-efficiency of the diamond modules was  $(65 \pm 7)$  %, with outliers down to 10 %. The value depended on the diamond quality, the set threshold and the applied bias voltage. The latter two settings were varied to check the behaviour of the modules under various conditions.

#### 4.4.2 Test beam results

The first two assembled prototype DBM modules, MDBM-01 and MDBM-03, were tested at DESY, Hamburg, in a test beam facility. The aim of the measurements was to measure their efficiency, the spatial distribution of the efficiency and the effect of the beam on the disconnected regions. A silicon module MSBM-02 was measured to crosscheck the measurements. Since the silicon module is almost 100 % efficient, it was used as an “anchor” – the efficiency of the diamond module was measured relative to that of the silicon module. Two beam telescopes were used as reference systems: Kartel [], built by JSI institute from Ljubljana, and EUDET Aconite []. Both are instrumented with six Mimosa26 pixel planes and capable of tracking particles with a 2  $\mu\text{m}$  pointing resolution.

The test beam prototypes did not meet the acceptance criteria for production DBM modules in the following areas: first, the stated CCDs were slightly below 200  $\mu\text{m}$ , which would be the DBM minimum. Secondly, the applied bias voltages ranged from 1–2 V/ $\mu\text{m}$ . In addition, the threshold cut could only be set to 1500 electrons, which is higher than the DBM minimum (1000 e). Nonetheless, the resulting module efficiencies were still in the range between 70–85 %.

To analyse the test beam data, Judith [] software framework was used. Judith is capable of synchronising data streams from several detector systems only connected via a trigger system, reconstructing tracks and calculating efficiency for the DUTs. It was also used to reconstruct and analyse the acquired Kartel test beam data together



(a) This is an efficiency distribution. Each bin corresponds to a single pixel. The triggering scintillator of the Kartel telescope was smaller than the DUT. Hence, the recorded hits can only be seen in the top half of the sensor.

(b) Pseudo-efficiencies for all modules at various threshold and voltage settings

Figure 4.10: An efficiency study of a prototype DBM diamond module in a test beam. The statistics are low ( $\sim 10$  hits/pixel) as the data was collected during a short run.

2016 with the silicon and diamond module as DUTs. A sample of the analysed data is  
2017 shown in figures 4.9a and 4.9b.

## 2018 4.5 Operation

### 2019 4.5.1 Positioning

2020 The DBM is placed in the forward region of the ATLAS detector, very close to the  
2021 beam pipe (see figure 4.11). The mechanical structure that holds the sensor planes is,  
2022 due to its shape, referred to as a DBM telescope. A telescope is a system that consists  
2023 of several pixel sensors placed in series one behind the other. Each DBM telescope  
2024 houses three diamond pixel modules. Eight DBM telescopes reside approximately  
2025 1 m away from the collision region, four on each side. They are tilted with respect  
2026 to the beam pipe for 10°. This is due to a specific phenomenon connected to erratic  
2027 (dark) currents in diamond. Studies have shown [] that the erratic leakage currents  
2028 that gradually develop in diamond can be suppressed under certain conditions. For  
2029 instance, if a strong magnetic field is applied perpendicular to the electric field lines  
2030 in the diamond bulk, the leakage current stabilises []. The DBM was designed to  
2031 exploit this phenomenon. The magnetic field lines in the ATLAS experiment are  
2032 parallel to the beam. Hence, an angular displacement of the sensor with respect to  
2033 the beam allows for the leakage current suppression. However, the DBM telescopes  
2034 still need to be directed towards the interaction region. Taking these considerations  
2035 into account, a 10° angle with respect to the beam pipe was chosen. The influence  
2036 of the magnetic field on the particle tracks at this angle is very low as the field lines  
2037 are almost parallel to the tracks. The tracks are therefore straight, which reduces the



Figure 4.11: This photo highlights four telescopes installed onto the nSQPs and around the pipe

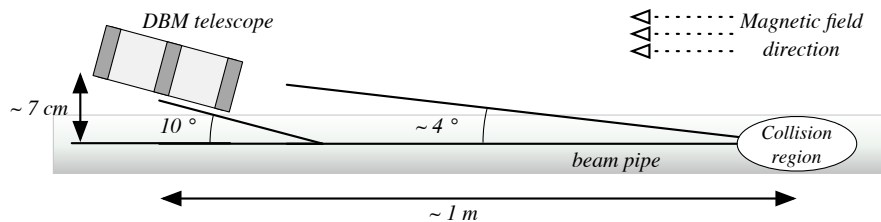


Figure 4.12: Position of the DBM in the ATLAS experiment

2038 track reconstruction complexity.

### 2039 4.5.2 Data taking during collisions

2040 The DBM has been commissioned in ATLAS and is now taking data. Several issues  
 2041 still need to be resolved regarding the readout systems. Unfortunately, due to issues  
 2042 with the low voltage power supply regulators, six out of 24 modules were damaged  
 2043 during operation: four silicon and two diamond modules. The system configured  
 2044 the modules into an unsteady state whereby they drew twice as much current as the  
 2045 allowed maximum. This current most probably fused the wire bonds within minutes.

## 4.5. OPERATION

---

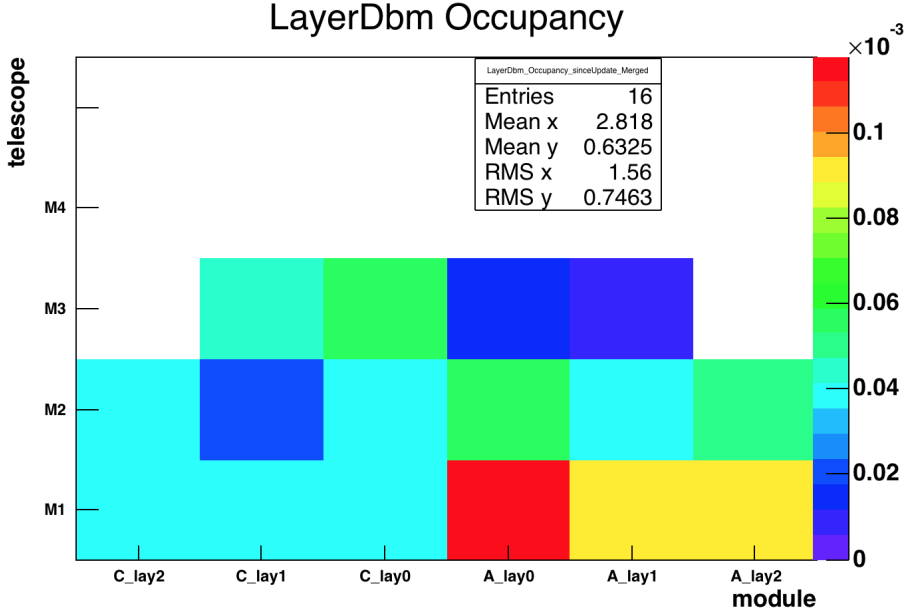


Figure 4.13: Occupancy of individual modules during collisions. Only 16 modules were taking data.

2046 This has left only five diamond telescopes fully operational. The preliminary data  
 2047 obtained using the remaining telescopes show that the background rejection could  
 2048 indeed work.

2049 The first step of the system test was to take data during collisions and check  
 2050 the occupancy in the individual modules. The occupancies were plotted side by side  
 2051 for comparison. Figure 4.12 shows some of the occupancy values. At the time, the  
 2052 readout system was not yet configured to read out all telescopes in parallel.

2053 The second step was to test the detector's capability of particle tracking. Only one  
 2054 telescope was used to take data with the beam. If all three planes of the telescope  
 2055 were hit during a bunch crossing, a linear line was fitted to the hits. This line  
 2056 represented the particle's trajectory. It was projected towards the interaction point.  
 2057 Two parameters were calculated where the line is the closest to the interaction point:  
 2058 the radial distance and the longitudinal distance between the line and the interaction  
 2059 point (see figure 4.13). This was done for the events with two colliding bunches as  
 2060 well as for events with only one, non-colliding bunch. The tracks recorded during  
 2061 the events with two colliding bunches could either come from the collisions or could  
 2062 be background scattering. Tracks recorded during a non-colliding bunch, on the  
 2063 other hand, are definitely background particles since, in principle, there should be no  
 2064 collisions taking place.

2065 A comparison of the data acquired (see figures 4.14a and 4.14b) showed that, for  
 2066 the colliding bunches, the majority of the reconstructed tracks had the origin in the  
 2067 interaction point, with an expected spread in  $Z$  and  $R$ . For non-colliding bunches,  
 2068 the distribution is more spread out. In the  $Z_0$  plot the distribution has one peak in

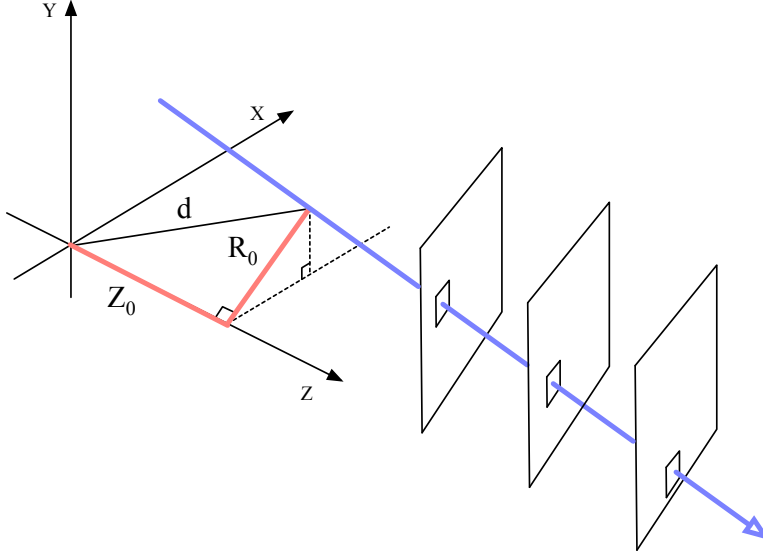


Figure 4.14: A diagram showing the radial distance  $R_0$  and longitudinal distance  $Z_0$  of the trajectory from the interaction point at the minimal distance  $d$ .  $Z$  is the axis along the beam line. Three module planes intercept a particle and reconstruct its trajectory.

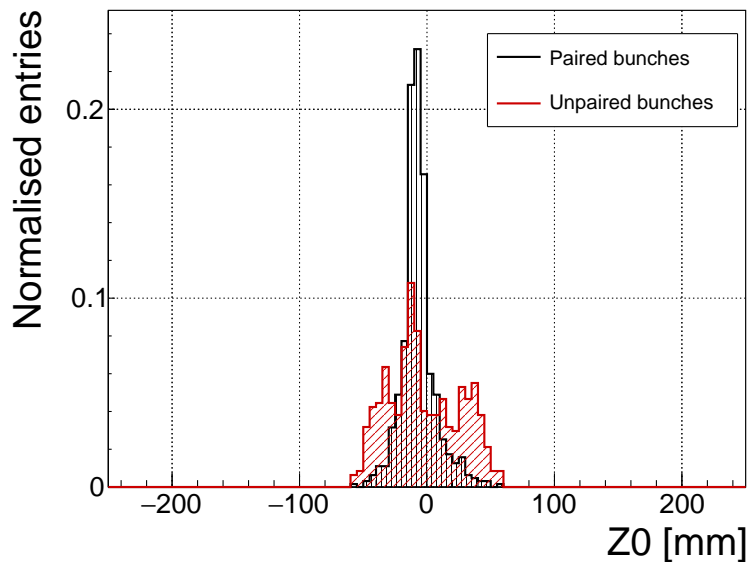
2069 the middle, which means that the empty RF buckets still held some particles. The  
 2070 two peaks on the sides, however, show that a significant number of tracks had their  
 2071 origin at the radius of the beam pipe. Therefore these tracks were made by stray  
 2072 protons colliding with the beam pipe. These collisions are unwanted as they do not  
 2073 produce any meaningful physics while still damaging the ATLAS detector by means  
 2074 of the scattered radiation.

## 2075 4.6 Conclusion

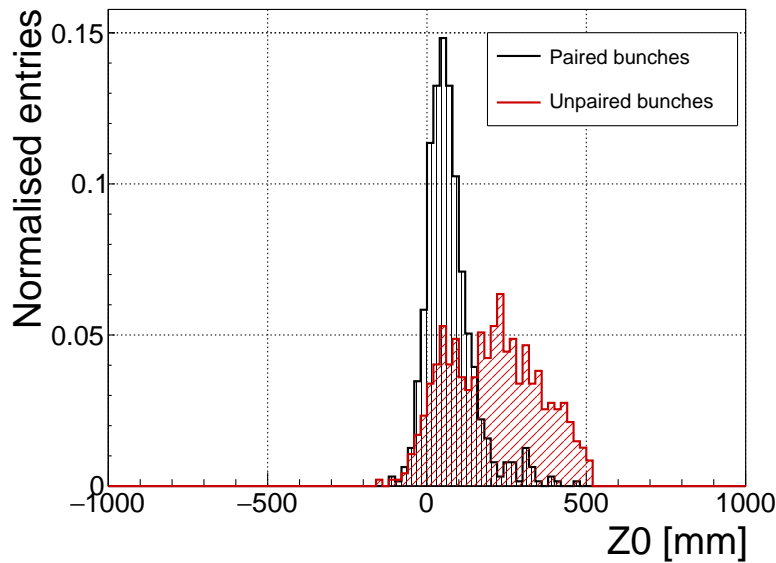
2076 The Diamond Beam Monitor has been designed as an upgrade to the existing lu-  
 2077 minosity detectors in the ATLAS experiment. It is the first diamond pixel tracking  
 2078 detector installed in a high-energy physics experiment. The pixelated front-end elec-  
 2079 tronic chips ensure precise spatial detection of the charged high-energy particles.  
 2080 The projective geometry allows for particle tracking and background rejection. The  
 2081 detector is placed in a high-radiation forward region of the experiment. Therefore,  
 2082 radiation hardness of the chosen pCVD diamond sensors is an important requirement.  
 2083 The tests carried out in the test beam and in the laboratory confirmed that enough  
 2084 detector-grade DBM modules have been built to be installed in the experiment. The  
 2085 DBM is now running in ATLAS during collisions. Further improvements have to be  
 2086 made on the readout firmware before it is included in the main readout stream.

#### 4.6. CONCLUSION

---



(a) Radial distance of the particle trajectories from the interaction point



(b) Longitudinal distance of the particle trajectories (along the beam path) from the interaction point

Figure 4.15: These two plots show two parameters of particle tracks recorded by one of the DBM telescopes: radial and longitudinal distance of the projected tracks from the interaction point.

2087

# Chapter 5

2088

## Current monitoring

2089

### *Real-time particle identification*

2090 Diamond sensors have a very fast signal response due to their low capacitance. The  
2091 electrical signal created by drifting charge carriers retains its shape without significant  
2092 distortion. When the sensor is used together with a fast current amplifier with a high  
2093 broadband limit ( $\sim 2$  GHz) and a readout device with a similar limit, the information  
2094 about the drifting charges is retained. For instance, a proton creates the free e-h pairs  
2095 along its trajectory. The electrons and holes start drifting immediately. Those closest  
2096 to the electrodes recombine quickly whereas those at the opposite side contribute to  
2097 the induced signal for longer. The resulting signal is therefore a triangular pulse  
2098 with a steep rising edge and a gentle falling edge. It is possible to determine the  
2099 drift velocity of the charge carriers by measuring the width of the pulse, as was done  
2100 in chapter 3. Furthermore, it is possible to determine with a certain probability  
2101 what is the type of incident radiation, judging by the shape of the induced pulse.  
2102 This, however, only applies to sCVD diamond material. Its uniform carbon lattice  
2103 allows the ionisation profiles to retain their shape, unlike in pCVD material, laden  
2104 with grain boundaries, or in even in silicon where the shape is deformed due to p-n  
2105 junction non-uniformities.

2106 This chapter describes an application that carries out particle identification by  
2107 means of the pulse shape analysis. It was developed for measuring activity of a  
2108 neutron reactor. In this case the device has to be able to filter out the photon  
2109 background with a rate several orders of magnitude higher than the neutron rate.  
2110 Overall detected rate in a neutron reactor can easily exceed  $10^8$  particles  $\text{cm}^{-2}\text{s}^{-1}$ ,  
2111 depending on the distance of the detector from the reactor core. The device has to  
2112 be able to cope with such high rates. It also needs to be dead time free or at least  
2113 close to that, to minimise the counting error. At these rates, it still has to be able to  
2114 identify the types of pulse. This type of online analysis cannot be done in software.  
2115 It has to be implemented in an FPGA.

## 5.1 MOTIVATION

---

### 2116 5.1 Motivation

2117 Pulse shape analysis (PSA) is a common software tool for analysing sensor response  
2118 to incident particles. It is usually done by means of software that runs over big  
2119 amounts of data that have been acquired and saved to storage. This offline analysis  
2120 can be repeated and improved. However, the saved data take up a lot of storage  
2121 space. In addition, saving raw waveform data requires a system capable of a high  
2122 data throughput and fast data storing. For instance, an oscilloscope can save up  
2123 to 100 signal waveforms per second. This means that there is a high measurement  
2124 dead time. To avoid the high dead times, the software algorithms can be ported  
2125 to the FPGA where they analyse the incoming signal in real time. The signal is  
2126 then discarded and only the analysis results are saved, decreasing the storage space  
2127 significantly.

2128 The offline pulse shape analysis has already been used for particle identification  
2129 with a diamond sensor [29, 24]. An effort has been made to implement an online and  
2130 real time application for this analysis by porting the algorithms into an FPGA. This  
2131 section first describes the device specifications Then it describes in detail the PSA  
2132 algorithms and the structure of the code. Afterwards it discusses the performance  
2133 results, which showcase the limitations of the device. Finally it describes the data  
2134 acquired with radioactive sources and in neutron reactors.

### 2135 5.2 Requirements

2136 Chapter 3 shows that the shape is heavily dependent on several factors, such as  
2137 environmental temperature and received irradiation dose. At temperatures lower  
2138 than 150 K the signal from an  $\alpha$  starts deteriorating due to recombination of charges  
2139 in the charge cloud. Sensor irradiation, on the other hand, introduces charge traps,  
2140 which cause the signal to decay exponentially. These two factors are a significant  
2141 limitation for particle identification. Priming can improve the charge collection and  
2142 longterm stability of the pulse shapes. To improve the measurement further, a high  
2143 bias voltage has to be applied, increasing the measurement SNR.

Factor	Operating range
Sensor material	sCVD diamond
Sensor thickness	500 $\mu\text{m}$
Temperature	150 K – 400 K
Radiation dose	$1 \times 10^{13} \text{ neq cm}^{-2}\text{s}^{-1}$
Charge carriers	holes
Bias voltage	$\sim 1 \text{ V } \mu\text{m}^{-1}$
Signal-to-noise	5

2145 Table 5.1: Limitations to particle identification

2146 **5.3 Device specifications**

2147 The ROSY box has a single BNC input with the termination  $50\ \Omega$  or  $1\ M\Omega$  with a  
2148 DC or AC coupling. The analog chain has a 250 MHz bandwidth limit. The input  
2149 range can be set from  $\pm 50\text{ mV}$  up to  $\pm 5\text{ V}$ . The signal offset can be set to any value  
2150 within this range. The ADC samples this signal with an 8-bit precision at a rate of  
2151 up to 5 GSPS. The PSA uses the highest sampling to achieve width measurement  
2152 resolution of 0.2 ns. The spectroscopic application does not need such a fine timing  
2153 resolution and therefore operates at a reduced sampling rate of 0.8 ns. The amplitude  
2154 resolution depends on the chosen input range, but at 256 ADC counts per sample, it  
2155 can be as low as  $0.39\text{ mV s}^{-1}$  at the range of  $\pm 50\text{ mV}$  and as high as  $39\text{ mV s}^{-1}$  at  
2156 the range of  $\pm 5\text{ V}$ .

2157 The logic structure of the PSA is designed using VHDL and runs on Xilinx Virtex 5. The PSA is capable of a maximum counting rate of  $1.56 \times 10^8$  pulses per second,  
2158 yielding a 6.4 ns double pulse resolution. The analysis is more time consuming; the  
2159 maximum throughput rate of the pulse shape analysis is  $\sim 5 \times 10^6$  pulses per sec-  
2160 ond. This means that after every pulse, the device has a dead time of approximately  
2161  $(200 \pm 15)$  ns, depending on the width of the pulse being analysed. Any pulse arriving  
2162 during the analysis of the previous one will be counted, but not analysed. Any two  
2163 pulses with the distance between the rising edges lower than 6.4 ns will be counted  
2164 as a single pulse.

2165 The device is very sensitive to noise pick-up. Therefore the setup must be designed  
2166 to minimise the pick-up by means of proper shielding, use of high-quality cables etc.  
2167 The relatively low bandwidth limit filters out some high-frequency noise, but not the  
2168 ringing or higher noise spikes. That is the task for the PSA.

2170 **5.4 Pulse parameters**

2171 A signal pulse on the input is parametrised during the analysis process. The PSA  
2172 measures its amplitude, area, width and the slope of its falling edge (see figure 5.1).  
2173 The amplitude is the difference between the baseline and the highest sample in the  
2174 pulse and is given in ADC counts as an 8-bit value. The area is defined as the sum  
2175 of amplitudes of all samples between two defined boundaries within the pulse. The  
2176 width is defined as the number of samples with a value higher than a set amplitude  
2177 threshold. If the threshold is at half the maximum amplitude, the resulting width  
2178 is *full width at half maximum* (FWHM). The falling slope is the maximum negative  
2179 difference between values of two samples and is given in ADC counts per sample.  
2180 These parameters can also be used as *qualifiers* for accepting or discarding a pulse.  
2181 All four parameters limited by the low and high limit are called a *qualifier set*. For  
2182 instance, a rectangular pulse by an  $\alpha$  particle will always have the same FWHM and  
2183 a very steep slope. In comparison, a photon will have a lower falling slope value and  
2184 a narrower FWHM. Therefore the low and high cut on these two qualifiers will make  
2185 it possible to discriminate between the two pulses. Another qualifier is a *form factor*

## 5.5. APPLICATIONS

---

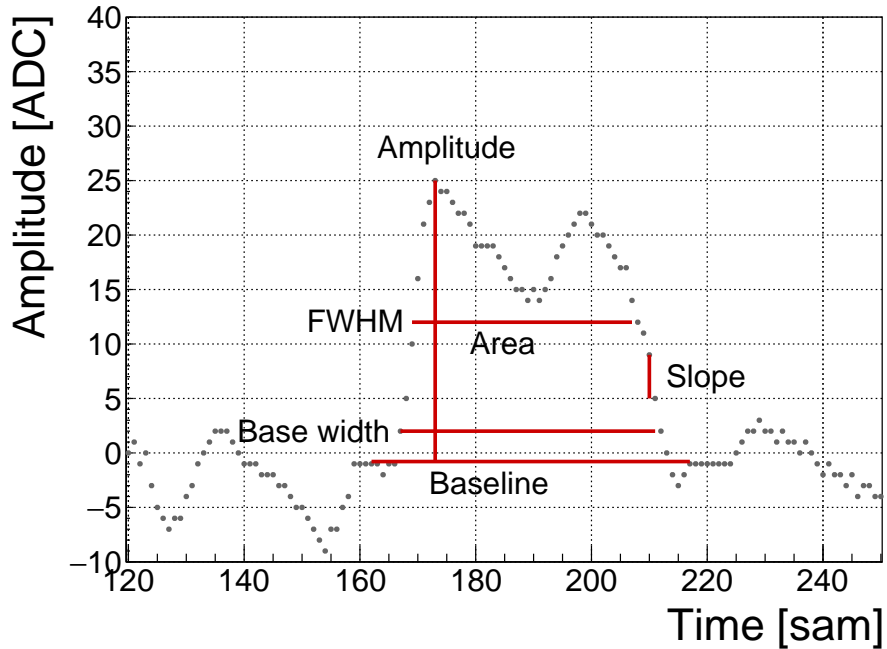


Figure 5.1: A pulse and its parameters

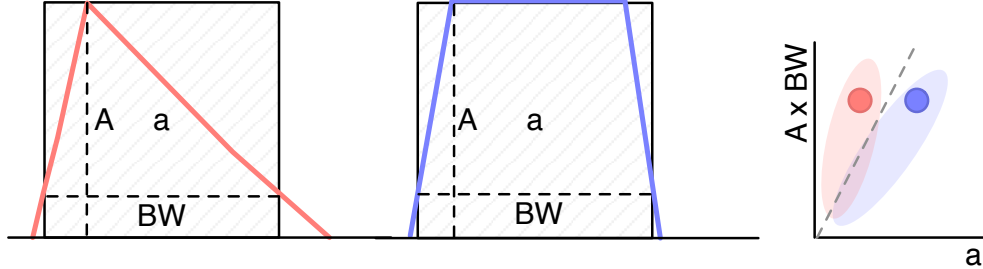


Figure 5.2: Form Factor is the ratio between the measured area ( $a$ ) and the calculated area ( $A \times BW$ ) of the pulse. The calculated area is significantly larger than the measured area for a triangular triangular pulse, but less so for the rectangular one. The red and blue dot in the right plot are the value entries of the two pulses shown. The red and blue oval shapes depict the regions for the values expected from triangular and rectangular pulses. By carefully choosing the linear qualifier (dashed line) and taking only the entries below the cut rectangular pulses can be identified.

and is defined as the ratio between the measured area and the amplitude multiplied by the width. By comparing the measured and the calculated area the difference between a triangular and a rectangular pulse can be inferred (see figure 5.2).

2189 **5.5 Applications**

2190 The FPGA firmware is designed for systems instrumented with CIVIDEC amplifiers  
2191 and CIVIDEC sVCD diamond detectors. Three applications are available: *Spectroscopy*,  
2192 *Pulse Shape Analysis* and *Counter*, each optimised for a specific task. Their  
2193 capabilities are described below. The firmware runs in ROSY, a readout system  
2194 produced by CIVIDEC.

2195 **Spectroscopy** is a tool for measuring energy spectra of radioactive sources. It is  
2196 used in combination with the CIVIDEC Cx spectroscopic charge amplifier. The  
2197 signal from the charge amplifier is analysed in real time. The FPGA measures the  
2198 maximum amplitude of the signal. The amplitude value is ready at the end of the  
2199 pulse and is stored in the amplitude histogram. Immediately after, the analysis is  
2200 reset and the system is ready for a new acquisition. Upon request from the software,  
2201 the histogram is read out, during which the analysis is paused. In addition to the  
2202 histogram building, the firmware can also store raw pulse waveforms, which can be  
2203 then read out by the software. The maximum allowed throughput is 1 million counts  
2204 per second.

2205 **Pulse Shape Analysis** is a tool for measuring energy spectra of radioactive sources,  
2206 with an additional feature. It can identify the type of radiation detected by the  
2207 diamond detector. By means of the pulse analysis it can subtract the background  
2208 radiation and only measure the signals from the defined radiation source. It is used  
2209 in combination with the CIVIDEC C2 fast current amplifier. The firmware receives  
2210 a current pulse from the detector and digitises it. The pulse is then analysed and  
2211 parametrised. The analysis module measures its maximum amplitude, full width  
2212 at half maximum (FWHM), baseline amplitude, falling slope and its area. Then  
2213 it compares the obtained pulse parameters with the qualifiers set by the software  
2214 and determines what type of radiation hit the diamond detector. Depending on the  
2215 qualifiers, the pulse can either be *accepted* or *rejected*. The firmware then stores the  
2216 parameters of the analysed pulse into histograms. Two histograms exist for each  
2217 parameter: one for all pulses and one for accepted pulses. In addition, there is one  
2218 2D histogram (a scatter plot), which can plot two parameters one with respect to the  
2219 other. Upon request from the software, all histograms are read out, during which the  
2220 analysis is paused. The maximum allowed throughput is 1 million counts per second.

2221 **Counter** is a tool that measures the count rate and the mean time during counts.  
2222 It is used in combination with the CIVIDEC Cx, C6 or C2 amplifier. It contains  
2223 one histogram which holds the information about the mean time during counts. The  
2224 counter is operational also during the readout of the histogram. The highest counting  
2225 rate with enabled histogram writing is  $3 \times 10^7 \text{ s}^{-1}$ .

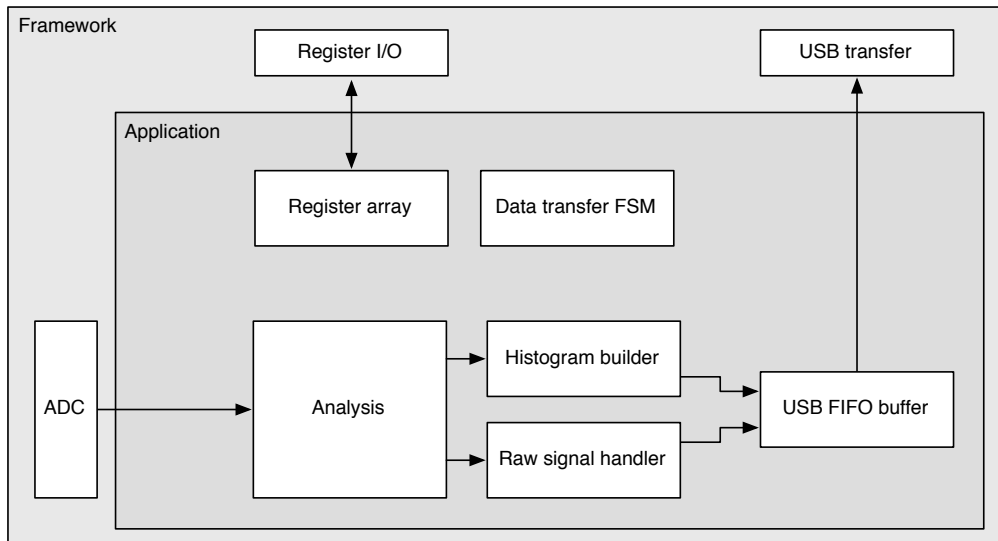


Figure 5.3: Firmware design structure

## 5.6 Description of the firmware

The applications are built on top of the Picotech platform. The base code handles the communication between the software and the hardware. Furthermore, it provides the interface to the ADC data, the input/output registers and the USB data transfer. The applications have a set of modules that handle the data input and output and a module for signal analysis (see figure 5.3).. The data handling modules are very similar in all the applications to ensure compatibility of the communication between software and firmware and the readout data format. The analysis module, however, is different from one application to the other. The data handling layer is the same for all applications and consists of the final state machine (FSM), the histogram builder, the raw signal handler, the USB FIFO buffer and the register array.

The firmware is written entirely in VHDL. The diagram in figure 5.3 shows the module architecture. The ADC provides the module with 32 digitised signal samples every clock cycle (6.4 ns). The signal is routed directly to the pulse analyser and into the raw signal handler. The analyser outputs are connected to the I/O registers and to histogram buffers. Both the histogram buffers and raw signal buffers are connected to the USB FIFO through a multiplexor. The firmware communication to the controller is done via input/output (I/O) registers (control and status registers, counters) and serially via USB (histogram data, waveforms).

### 5.6.1 Design constraints

**Speed** The ADC provides 32 8-bit samples on every 6.4 ns clock cycle. It is not possible to e.g. sum all 32 values in a single cycle, because the summation takes too long to complete. This is why the summation has to be pipelined and carried out

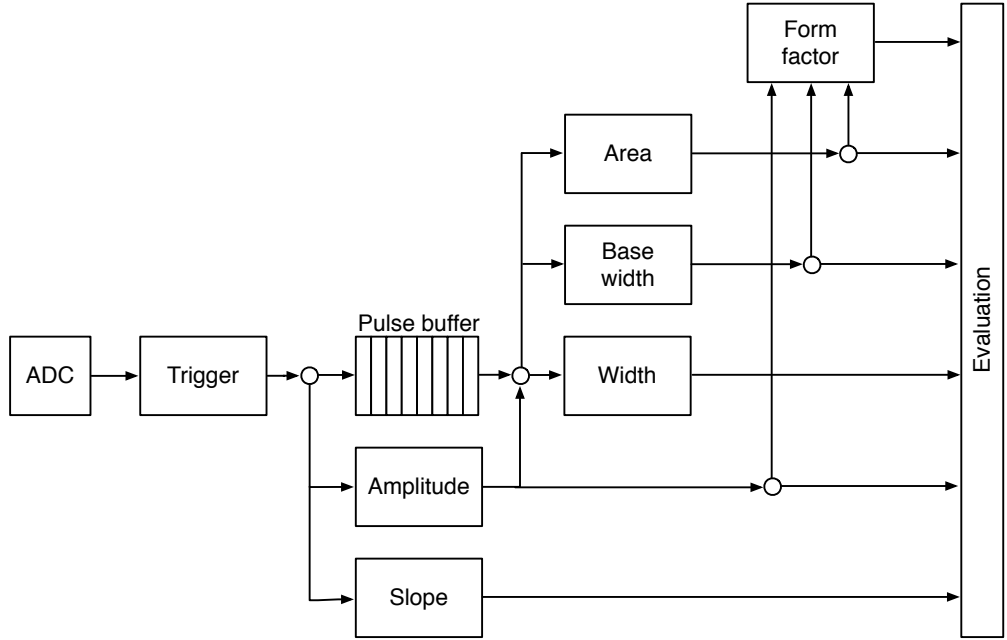


Figure 5.4: Code design plan

in three cycles. This adds up to the analysis duration, which in turn decreases the maximum pulse rate.

**Firmware size** The PSA application makes use of a number of FIFO and RAM buffers to store the pulse waveforms and histograms. 48 32k block RAM modules have been used for the implementation, maxing out the available block RAM memory space on this FPGA. The analysis algorithm also takes up a significant portion of the FPGA. Many of the operations are carried out on 256-bit long numbers received from the ADC, which quickly fills up the available logic. This is also why the place and route procedure takes a long time.

**Power consumption** The reduction of the power consumption is not crucial for the intended applications.

## 5.6.2 Analysis module

This module is different for different applications. The Pulse Shape Analysis (PSA) application has the most complex module design. The spectroscopy application only uses a small part of that design and the Counter application an even smaller one.

The analysis (or parametrisation) is carried out in several steps, as shown in figure 5.4. The triggering block starts the readout upon signal threshold crossing. The maximum slope of the falling edge is observed. The Amplitude block calculates the pulse height and retains the maximum amplitude while pushing the signal into the pulse buffer. Then the whole pulse is clocked out of the buffer while its FWHM,

## 5.6. DESCRIPTION OF THE FIRMWARE

---

2269 baseline width and area are measured. Finally, the Form factor is calculated. At the  
2270 end the Evaluation block takes in all the parametrised information and classifies the  
2271 pulse according to user-defined cuts.

2272 **Triggering** module handles signal polarity swapping, triggering on threshold and  
2273 defining the trigger window. The real-time processing algorithm allows for a pos-  
2274 itive or an inverted input signal. However, the PSA only handles positive-polarity  
2275 pulses. Therefore a negative signal is swapped in the *triggering* block. Signal analysis  
2276 and readout are then triggered when the signal crosses a user-defined threshold. In  
2277 addition, the signal has to be over the threshold for a defined number of samples.  
2278 This is to avoid triggering on noise spikes. A double clock cycle delay is used on the  
2279 signal to make sure that the recorded signal window will include the rising edge of  
2280 the pulse as well as some baseline before it. A *trigger active* signal marks a window  
2281 that contains the whole pulse including some baseline signal before and after it. The  
2282 trigger can be vetoed by three signals: if the pulse analysis is still taking place, if  
2283 the input signal exceeds the maximum voltage range or if the data transfer FSM is  
2284 pausing the analysis due to data transfer to the controller.

2285 **Amplitude** block calculates the pulse height from the difference between the pulse  
2286 and the baseline. It also finds the position of the maximum amplitude within the  
2287 clock cycle. It receives 32 8-bit samples from the triggering block every clock cycle.  
2288 Time delays in the logic prevent it to find the maximum value of the 32 samples  
2289 within one clock cycle (6.4 ns). Therefore the decision logic has been pipelined in  
2290 three stages, which means that the final maximum value is ready three clock cycles  
2291 after the end of the pulse.

2292 **Pulse buffer** is a FIFO that stores the signal while its amplitude is being measured.  
2293 At the end of the pulse the FIFO is read out so that the remaining measurements  
2294 can take place.

2295 **Width** block uses the maximum amplitude to determine the *half-maximum* and to  
2296 measure the FWHM. To do so, it counts the samples that are above the half-maximum  
2297 amplitude. However, this method might also count high enough noise spikes before  
2298 or after the pulse. Hence an improved method, which “cleans” the measurement of  
2299 unintentional additional noise, has been implemented. It is described in section 5.6.3.

2300 **Baseline width** block is the same as the Width block, but it measures the width  
2301 either at 50 %, 25 %, 12.5 % or 6.25 %, depending on the setting in the register. It  
2302 also makes use of the special method described in 5.6.3 to avoid overestimations due  
2303 to including noise in the measurement.

2304 **Area** block measures the pulse area by summing up the amplitude values of the sam-  
2305 ples in the pulse. The boundaries of the summation are defined with the crossing of  
2306 the amplitude above a certain threshold. Only the samples between those boundaries  
2307 are summed up. The boundaries can be set at 50 %, 25 %, 12.5 % or 6.25 % of

2308 the maximum amplitude of the pulse. The area measurement makes use of the same  
2309 routine as the FWHM and Baseline width block to remove the potential outlying  
2310 samples.

2311 **Falling slope** block measures the highest negative difference between amplitudes of  
2312 two adjacent samples, thus getting the maximum negative slope of the pulse. It is an  
2313 experimental routine, only used for academic purposes.

2314 **Form factor** block is used as a special qualifier for particle identification. It com-  
2315 pares the weighted measured area of the pulse with its weighted calculated “form”,  
2316 which is defined as the multiplication of the measured amplitude and baseline width.  
2317 The equation is as follows:

$$x \cdot a - y \cdot A \cdot BW \geq 0, \quad (5.1)$$

2318 where  $a$  is the measured area,  $A$  is the amplitude,  $BW$  is the baseline width and  $x$   
2319 and  $y$  the weighting factors for the measured and calculated area, respectively. The  
2320 output of the block is the boolean result of this equation.

2321 **Evaluation** block takes in all the parameters from the analysis blocks and compares  
2322 them against the user-defined qualifiers. If the parameters are within the bounds,  
2323 the pulse is accepted, otherwise it is rejected. The corresponding counters within the  
2324 block are incremented.

### 2325 5.6.3 Area and width measurement

2326 The routine for measuring pulse area and width must have a specific algorithm imple-  
2327 mented to carry out the measurements correctly. The core point is that the routine  
2328 precisely defines the edges of a pulse. It does so by means of *vector cleaning*, pre-  
2329 sented in figure 5.5. An important input, beside the ADC data and the measurement  
2330 threshold, is the position of the sample with the highest amplitude.

2331 The signal arrives from the ADC as a set of 32 8-bit samples every every clock cycle  
2332 with a period of 6.4 ns. All 32 samples are compared against the width measurement  
2333 threshold. If a sample value is equal or higher than this threshold, a binary 1 is set  
2334 in a 32-bit *vector* on the position corresponding to the position of the sample in the  
2335 incoming ADC data set. The resulting vector might also include some noise at the  
2336 edges of the pulse, depending on the height of the width measurement threshold. The  
2337 old routine simply counts the binary ones in this vector to get the pulse width. This  
2338 works well for measuring the FWHM because the threshold was high. However, for  
2339 width measurements at 25 %, 12.5 % or 6.25 % of the pulse height this might already  
2340 become a problem, because the noise might be counted in as well. This is why the  
2341 new routine cleans the outliers in this vector before counting the remaining ones in  
2342 the clean vector.

2343 The routine starts from the position of the maximum height. It follows the vector  
2344 in both ways and finds the first falling edge (0 at this position and 1 at the previous

## 5.6. DESCRIPTION OF THE FIRMWARE

---

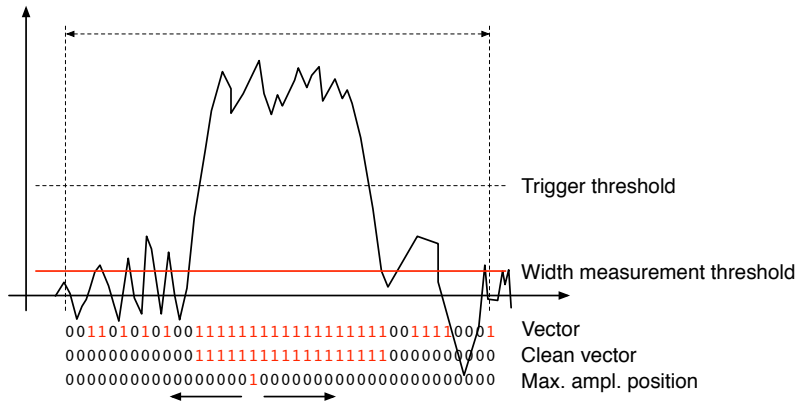


Figure 5.5: A sample pulse. The first vector shows which samples are above the width measurement height. The second vector is a clean vector. The third line shows the position of the maximum amplitude. The vector cleaning algorithm starts from the maximum amplitude and continues in both ways along the vector.

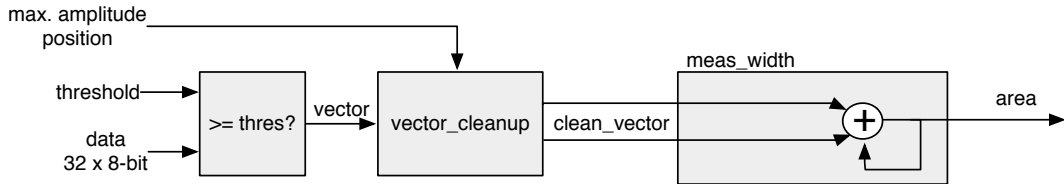


Figure 5.6: This block counts the remaining binary ones in the clean vectors and outputs this value as the pulse width.

2345 one). From there on it rewrites any binary 1 with a binary 0. The resulting clean  
 2346 vector only has one bunched set of binary ones which are summed, yielding a precise  
 2347 pulse width. The area measurement is similar - it only integrates over the samples  
 2348 marked in the clean vector. Both measurement routines, for area and for width, are  
 2349 implemented separately so that the area routine can have a different threshold set.

2350 This section explains how the algorithm is designed. First, the idea for it was  
 2351 tested using Excel and was only afterwards ported to the VHDL. The underlying  
 2352 algorithm first cleans the vector. Then it passes the cleaned vector either to the  
 2353 width or area measurement (see figures ?? and ??). The width measurement module  
 2354 only sums the ones in the vector whereas the area measurement module sums the  
 2355 data samples marked by the cleaned vector. Both modules issue a *valid* signal when  
 2356 they finish the measurement.

### 2357 5.6.3.1 Vector cleaning

2358 This is the most important block. Its inputs are: *vector*, *parsing active*, *position of the*  
 2359 *max. amplitude (PA)* and its delay (*DA*). *PA* is a 32-bit binary number that shows the  
 2360 position of the sample with the maximum amplitude within the data block whereas

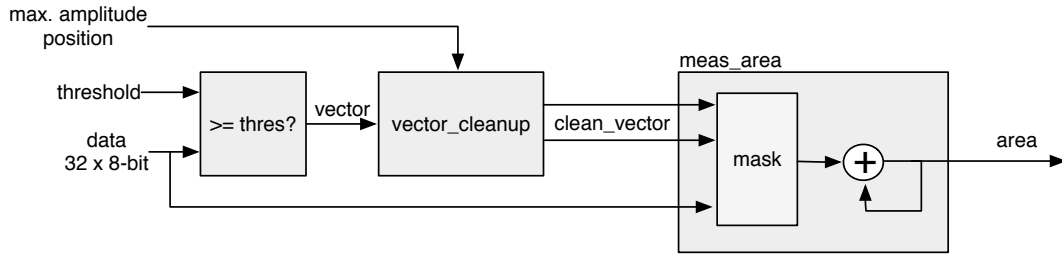


Figure 5.7: This block masks the input data with the clean vector and sums the remaining samples.

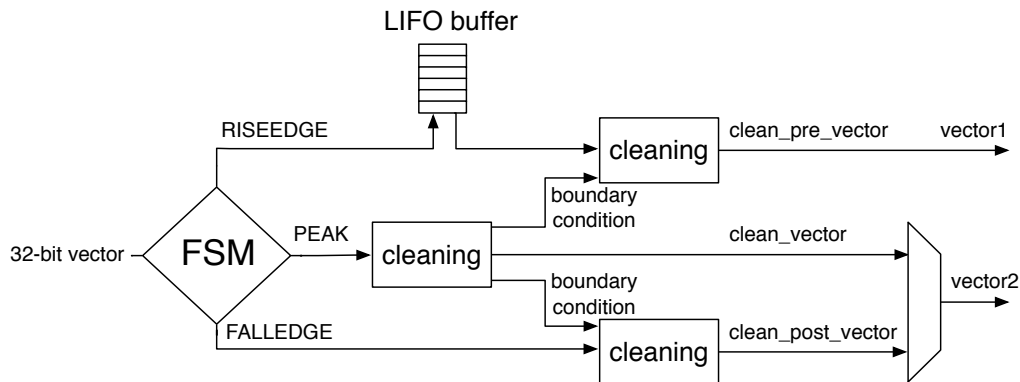


Figure 5.8: Vector cleaning routine outputs two vectors - one forward in time and one back in time from the peak of the pulse.

2361 the DA tells us how many clock cycles after the start of the parsing this PA block  
 2362 is. The vector cleaning module is designed as a final state machine (FSM) with the  
 2363 states IDLE, RISEEDGE, PEAK, FALLEDGE and READY. The FSM is idle until it  
 2364 receives the *active* signal from the external module, marking that the vector parsing  
 2365 has commenced. It switches to RISEEDGE, which starts two procedures: 1) it fills  
 2366 the vector of the pulse's rising edge into a last-in-first-out (LIFO) buffer and 2) counts  
 2367 down from the DA value. When this counter reaches 0, the FSM changes its state to  
 2368 PEAK because the current vector on the input is the one containing the maximum  
 2369 amplitude. This data block is sent through the *peak algorithm*, which cleans the  
 2370 vector. The FSM switches to FALLEDGE state. Now both the previously buffered  
 2371 vector of the rising edge and current vector of the falling edge go through the *pre-*  
 2372 *and post- algorithm* where they are cleaned, but they get their boundary conditions  
 2373 from the *peak algorithm*. The output of this module is therefore two cleaned vectors  
 2374 in parallel – one forward in time and the other backwards.

### 2375 5.6.3.2 Algorithm

2376 The underlying algorithm is sequential - it carries out a logic operation on vector bit  
 2377 on position 0, uses the output of this operation for the operation on bit on position

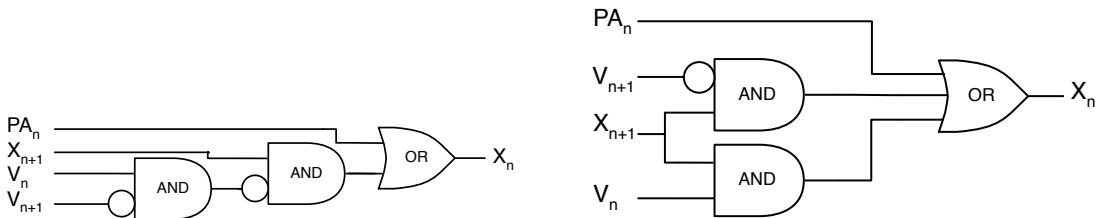


Figure 5.9: One logic step in the algorithm chain before and after Karnaugh minimisation.

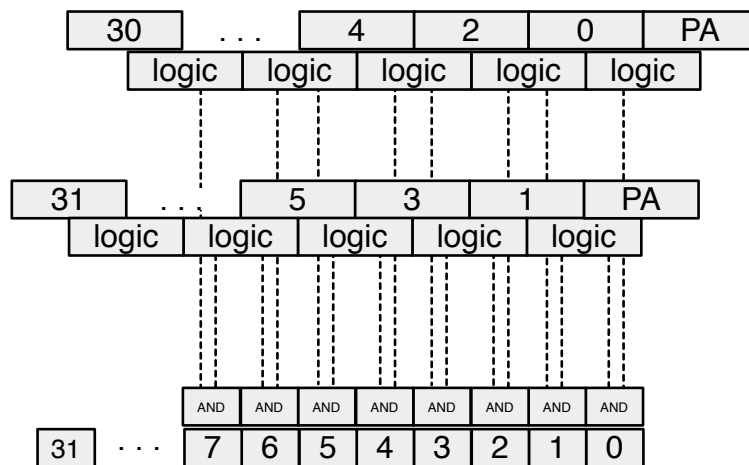


Figure 5.10: Vector is divided into two 16-bit logic chains. The algorithm logic is then run on the two chains separately. The results are then merged into one 32-bit clean vector by using a set of AND gates.

2378 1 and so on. This means that it has to carry out 32 logic operations per clock  
 2379 cycle. With each operation taking approximately 0.3 ns, the whole logic chain takes  
 2380 approximately 10 ns to complete. With only 6.4 ns per clock cycle, this means timing  
 2381 errors would occur. To fix the problem, a more complicated *decimated algorithm* has  
 2382 been designed. It consists of two parallel logic chains. Each of the two only takes  
 2383 every second bit into account (chain one: 0, 2, 4 ..., 30. Chain two: 1, 3, 5 ..., 31).  
 2384 This makes the chains effectively 16 bits long. The algorithm is run on the two chains  
 2385 and the results are merged together at the end as shown in figure 5.10. This effectively  
 2386 reduces the number of sequential logic operations to around 18, which is within the  
 2387 timing constraints.

## 2388 5.7 Control and data interface

2389 Communication between the device and the controller PC is done via the API func-  
 2390 tions provided by the producer. In addition, the API used by CIVIDEC has access

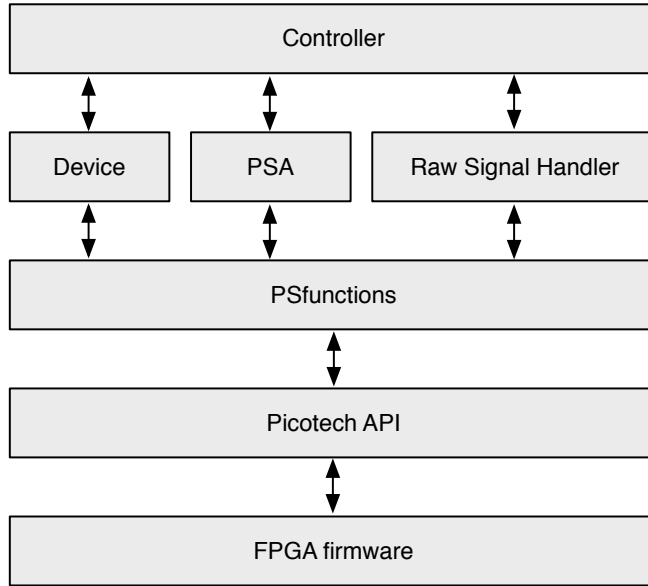


Figure 5.11: Abstraction levels of the controller software

2391 to several extra functions. These allow the user to download a customised bitfile to  
2392 the FPGA, access the I/O registers and use the USB data transfer.

### 2393 5.7.1 Software

2394 The software has been designed in C++ in several levels of abstraction. Figure 5.11  
2395 shows the structure of the classes. The classes Device, PSA and RawSignalHandler  
2396 are there to make it easier to read and understand the controller code. In principle the  
2397 PSfunctions can also be accessed directly by the controller, but for this the instruction  
2398 sequences must be well known and understood.

### 2399 5.7.2 Data readout

2400 The device records the data in two forms - as signal waveforms and as histograms  
2401 of analysed pulse parameters. Both are available upon request from the controller.  
2402 Only one of the two can be transferred via the USB line at a time.

2403 The waveforms are saved into a FIFO buffer, which can hold up to 64 pulses of the  
2404 length of  $\sim 500$  samples. The data format for each pulse is such that it starts with a  
2405 header containing the pulse timestamp and the sequential number, continues with the  
2406 data samples and ends with a header containing all the measured parameters (width,  
2407 amplitude, area, falling slope and form factor). When the FIFO is full, it issues a  
2408 flag, which tells the controller that the data buffer is ready for readout.

2409 The histograms are implemented into the FPGA's Block RAM. Their size ranges  
2410 from 256 to 4096 bins (an 8-bit or a 12-bit histogram, respectively), depending on the  
2411 required histogram resolution. For instance, the width parameter is measured with a

## 5.8. PERFORMANCE RESULTS

---

2412 0.2 ns resolution; the expected maximum pulse width is less than 20 ns. This yields  
2413 the maximum range of 100 bins, making an 8-bit histogram sufficiently large. The  
2414 same reasoning is applied to the amplitude measurement. In this case the maximum  
2415 range is defined by the 8-bit resolution of the ADC. The area measurement, however,  
2416 yields higher values and can therefore have a more refined binning (12-bit). Finally,  
2417 a single 12-bit 2D histogram is included, with 6 bits for every axis. It is used as an  
2418 online scatter plot for comparing one measured parameter to another. An example  
2419 for it is a comparison of the width against the area, which can help the user determine  
2420 the cuts that need to be applied to the measurement.

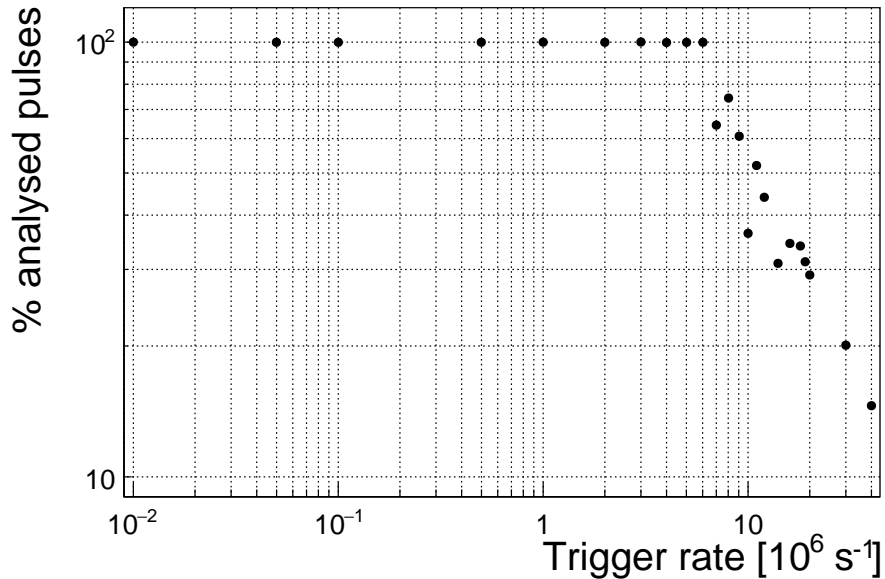
## 2421 5.8 Performance results

2422 The device has been tested in the lab using a pulse generator as well as several radioac-  
2423 tive sources. The results show that: 1) the amplitude, area and width measurement  
2424 are linear across all input ranges, 2) the highest rate of the PSA algorithm is  $\sim 5 \times 10^6$   
2425 pulses per second and 3) the lowest SNR where the algorithm still functions is  $\sim 5$ .

2426 **Trigger rate** A pulse generator was used to verify the highest achievable rate at  
2427 which the PSA still analyses every incoming pulse. The final state machine imple-  
2428 mented in the pulse analysis module prevents the triggering block from issuing a  
2429 trigger due to an incoming pulse if the previous analysis is still in ongoing. Given  
2430 that all the pulses were of the same length, the analysis duration was always the  
2431 same. When the time between the incoming pulses was shorter than the time of the  
2432 analysis, the pulses were not analysed. Figure 5.12 shows the sharp decline in the  
2433 percentage of the analysed pulses when reaching the rate of 5 MHz. Therefore the  
2434 overall analysis duration for a 10 ns pulse is approximately 200 ns.

2435 **Linearity** A pulse generator was used to verify the linearity of the measurements  
2436 across all input ranges. Pulse width and amplitude were varied and measured both  
2437 with the oscilloscope and the PSA to check for non-linearities or inconsistencies in the  
2438 PSA measurements. The resulting plots in figures ?? and 5.13c show that the PSA  
2439 measurements agree well with those from the oscilloscope. The major inconsistency  
2440 is observed in the lower range of the plots. It stems from the fact that the bandwidth  
2441 limit of the PSA is lower than that of the oscilloscope, which affects the pulse shape.  
2442 Effectively, the PSA cannot measure the rectangular pulses of the width smaller than  
2443 2 ns.

2444 **Stability** The input pulse signal was superimposed with white noise generated by  
2445 a noise generator with a variable gain. The mixed signal yielded pulses with an  
2446 SNR ranging from 5 (very noisy) to 100 (noise negligible). The PSA then performed  
2447 the pulse parametrisation at different SNRs. The resulting plots in figures 5.13b,  
2448 5.13d and 5.13e show that the pulse width measurement is stable even for low SNR  
2449 whereas the amplitude measurement is affected significantly. This stems from the  
2450 analysis taking the highest sample as the pulse's amplitude. The area measurement,



## 5.8. PERFORMANCE RESULTS

---

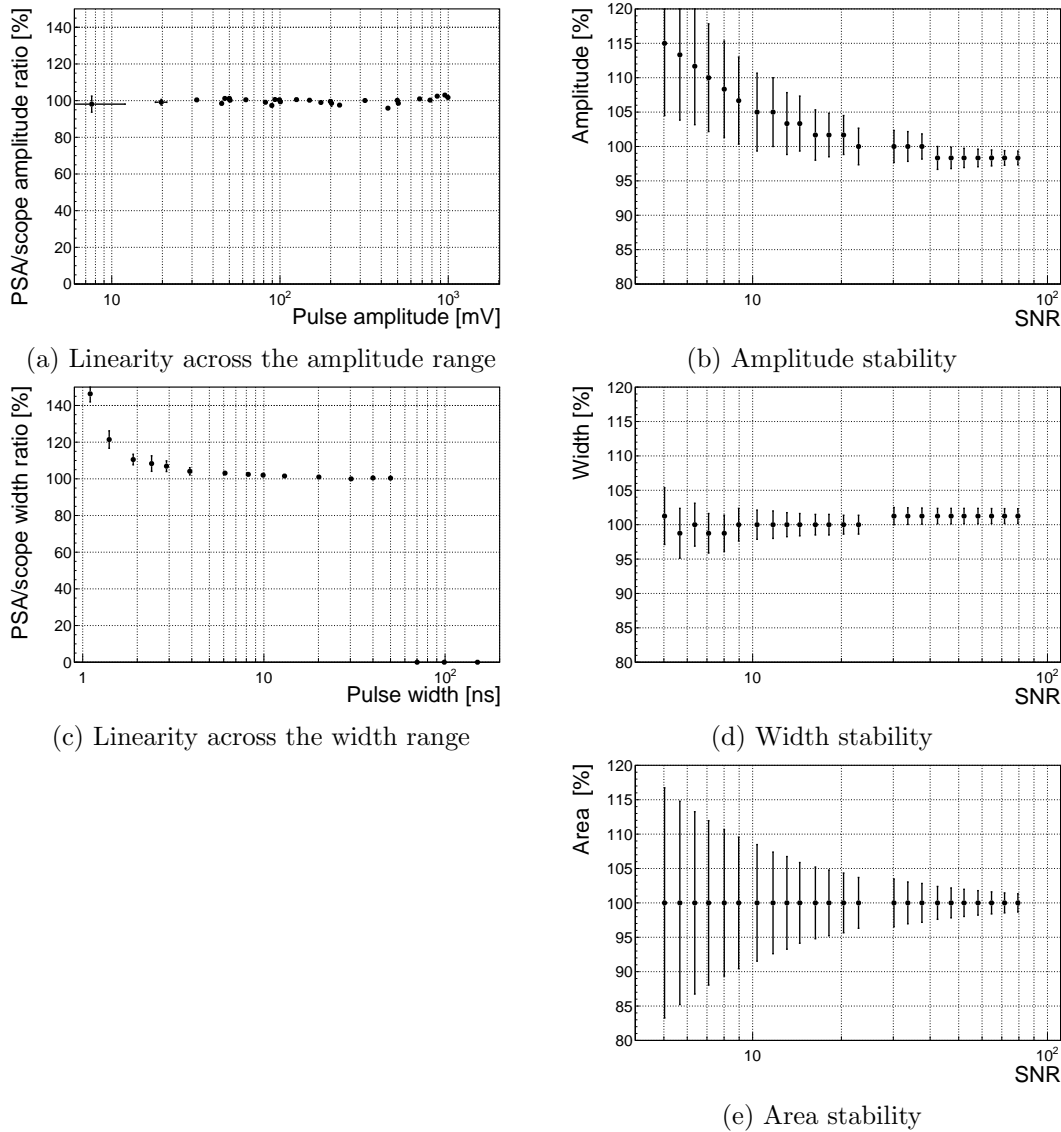


Figure 5.13: These diagrams show the linearity of the measurements and their stability with respect to analog noise.

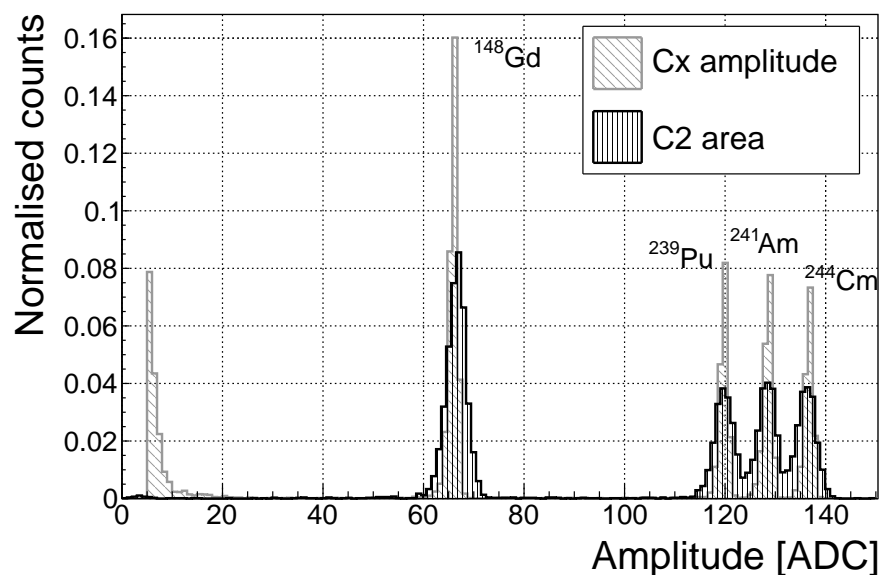


Figure 5.14: Spectrum of a  $^{148}\text{Gd}^{239}\text{Pu}^{241}\text{Am}^{244}\text{Cm}$  source using a Cx and a C2 amplifier

## 5.9. SOURCE CALIBRATION

---

### 2466 5.9 Source calibration

2467 The operation of the pulse shape analysis has been tested using several radioactive  
 2468 sources. In particular, an  $\alpha$ , a  $\beta$  and a  $\gamma$  source have been used. Each source has  
 2469 been placed on top of the diamond detector and left for a predefined time depending  
 2470 on its activity. Table 5.2 shows the sources used, the time of exposure and their rate  
 2471 during this time. The data for the  $\alpha$  source have been taken for both polarities. In  
 2472 addition, a long run with an  $\alpha$  source with a sheet of paper in between the source  
 2473 and the diamond has been taken. The paper stops the  $\alpha$  particles but lets through  
 2474 the photons, which helps to estimate the background photon radiation of the source.

Run	Source	Radiation	Energy [MeV]	Time [h]	Triggers	Rate [ $s^{-1}$ ]	Bias [V]
2475	1 $^{241}\text{Am}^*$	$\alpha$	5.5	60	958	4.4e-3	500
	2 $^{241}\text{Am}$	$\alpha$	5.5	17	10558	0.17	500
	3 $^{241}\text{Am}$	$\alpha$	5.5	18	11454	0.18	-500
	4 $^{90}\text{Sr}$	$\beta$	2.3	0.42	1.07e6	1000	500
	5 $^{60}\text{Co}$	$\gamma$	1.3	0.28	1.34e6	3300	500
	6 $^{239}\text{Pu Be}$	$n$	1-10	2.5	1.5e6	230	500

2476 Table 5.2: Measurements carried out at Atominstitut

2477 The pulses acquired during the data taking are shown in persistence plots in  
 2478 figures 5.15. Figure 5.15a showing the  $^{241}\text{Am}$  source background reveals that the  
 2479 diamond detector had been contaminated, probably with chipped-off grains of the  
 2480 unsealed source. This stems from the fact that  $\alpha$  pulses are recorded despite having  
 2481 a sheet of paper, which stops all the particles emitted by the source. However, the  
 2482 number of  $\alpha$  hits due to contamination is negligible - an estimated  $1 \text{ h}^{-1}$ . Another  
 2483 point worth noting is the falling slope of the rectangular pulse in figure 5.15c. This  
 2484 stems from the space charge that had built up during the neutron irradiation and is  
 2485 discussed in section ???. Finally, figure 5.15f shows that the neutron source causes  
 2486 the widest variety of pulse shapes - triangular and rectangular as well as those in  
 2487 between. Pulse shapes caused by neutrons are described in detail in [44, 43].

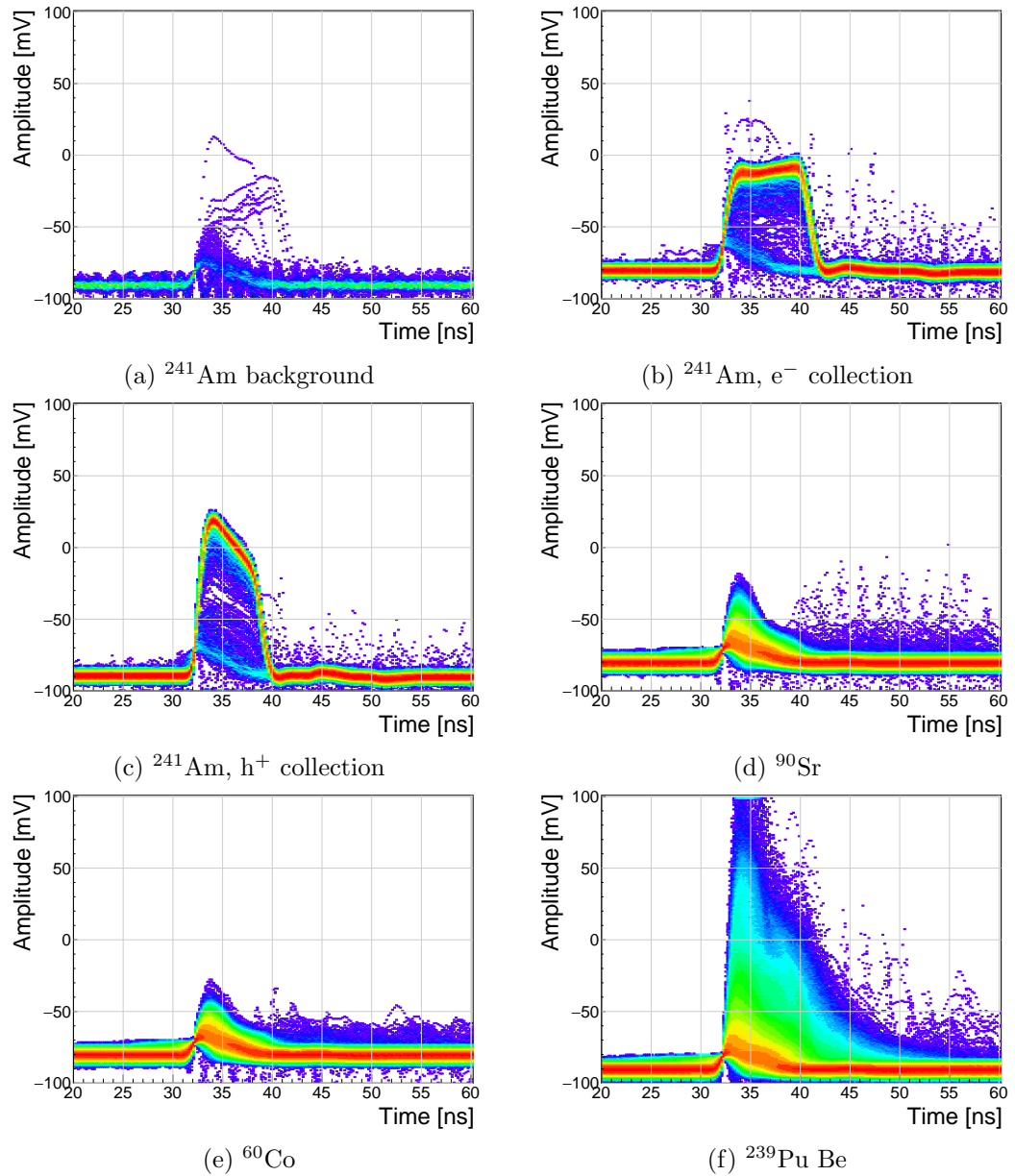


Figure 5.15: Accumulated pulses for all runs

## 5.9. SOURCE CALIBRATION

---

### 5.9.1 Source measurements – scatter plots

An online pulse shape analysis has been run on all the above mentioned data sets. The parameters of the pulses are plotted in 2D histograms - in form of scatter plots. The aim is to find a way to distinguish between the various types of radiation in order to only select the spectrum of a single type of particles from a spectrum of a mixed source. The energy spectrum is directly proportional to the measured area of the current pulses, therefore all the parameters are plotted against the pulse area. The parameters used are:

- FWHM
- Base width
- Amplitude
- Amplitude × Base width
- Base width – FWHM
- Falling slope

Every individual parameter can be attributed a set of qualifiers with which a certain part of the distribution can be rejected. There are two ways to apply the qualifiers. One is to set the minimum and maximum value for a specific parameter. The accepted pulses are those in between these two values. The minimum and the maximum qualifier are marked with a blue and a red line in the subsequent scatter plots. The second way is to apply a linear cut to the distribution in the scatter plot. The user can choose the slope of the line and to accept either the pulses above or below the line. The colour of the line is blue if the part above the line is accepted and red if opposite. Currently two scatter plots have this option implemented: area vs amplitude and area vs amplitude×base width. The latter represents the Form Factor, which is discussed in section 5.6.2.

The sets of plots in figures 5.16, 5.17, 5.19 and 5.20 show the above listed parameters plotted against the pulse area for  $^{241}\text{Am}$  background, electrons and holes,  $^{90}\text{Sr}$  and  $^{64}\text{Co}$  source, respectively. Any distinguishable difference between the plots of two sources would suggest that that particular parameter can be used to distinguish one type radiation from the other. For the most part the photons are considered the rejected pulses (greyscale colour palette) whereas  $\alpha$  particles or neutrons are accepted (yellow colour palette). In special cases only a certain types of neutron interactions are accepted (see section 5.10).

#### 5.9.1.1 $^{241}\text{Am}$ source

The source emits  $\alpha$  particles at  $\sim 5.5$  MeV and photons with a range of energies. Due to the losses in the air and the electrode the measured  $\alpha$  energy varies – between  $\sim 5$  MeV down to 1 MeV.

Figures 5.16 and 5.17 show the pulse area distribution with respect to the aforementioned parameters, for electrons and holes respectively. Focusing on the top left plot in figure 5.16, a distinctive horizontal stripe appears at a width of 9 ns, ranging from 100 up to 630 pVs. This is the aforementioned spread of  $\alpha$  energies. The shape of the pulse from this type of radiation retains the width even at smaller energies. Only its amplitude is decreased. This is because the free charge carriers in the diamond are traveling with the same speed in all cases, inducing rectangular pulses of the same widths.

The other cluster in the [area, FWHM] phase space comes from the background photons. The two clusters are far apart from one another with no overlap. It is therefore straightforward to define a cut in the FWHM to distinguish between the  $\alpha$  and  $\gamma$  entries. This is done by means of the minimum and maximum FWHM constant qualifier, which marked red and blue in the [area, FWHM] subfigure.

The [area, amplitude] subfigure also reveals two distinguishable clusters, which can be segregated using a linear qualifier. The angle of the  $\alpha$  stripes in the [area, amplitude] subplots is significantly smaller than that of the photon stripe. The separation is much less pronounced in the other subfigures.

There is a third barely distinguishable island visible in the top two plots, both area and width values close to zero. This island is formed by noise, which triggered the analysis.

The situation is similar when inverting the bias voltage and collecting holes (see figure 5.17). Here, however, the two clusters are much closer together even in the [area, FWHM] subfigure. This makes it more difficult to define a clear border between the two. The other five qualifiers are in this case less important than the FWHM. Nevertheless, it can be deduced from the plots that the difference BW-FWHM must be below 4 ns.

The slope is dependent of the amplitude, which can be seen in the bottom right plot, making it an unreliable qualifier in the lower area range. The amplitude, scaling with area, makes a distinguishable straight line in the middle left subfigure.

The amplitude increase with area in the [area, amplitude] subfigure is similar for photons and  $\alpha$  particles. Therefore a linear qualifier can not be used to distinguish  $\alpha$  radiation from  $\gamma$  radiation when measuring holes.

Figures 5.18a and 5.18b show a one-dimensional area distribution of the acquired data for electron and hole collection. The blue histogram represents all collected data whereas the red one marks the data whereby the pulse parameters are within the qualifiers. In both figures the  $\alpha$  peak at 600 pVs is clearly visible, followed by a  $\gamma$  quasi-Landau distribution with an MPV of  $\sim$ 70 pVs and a noise peak at the very left of the area distribution. These two contributions have been rejected by the FWHM qualifier.

## 5.9. SOURCE CALIBRATION

---

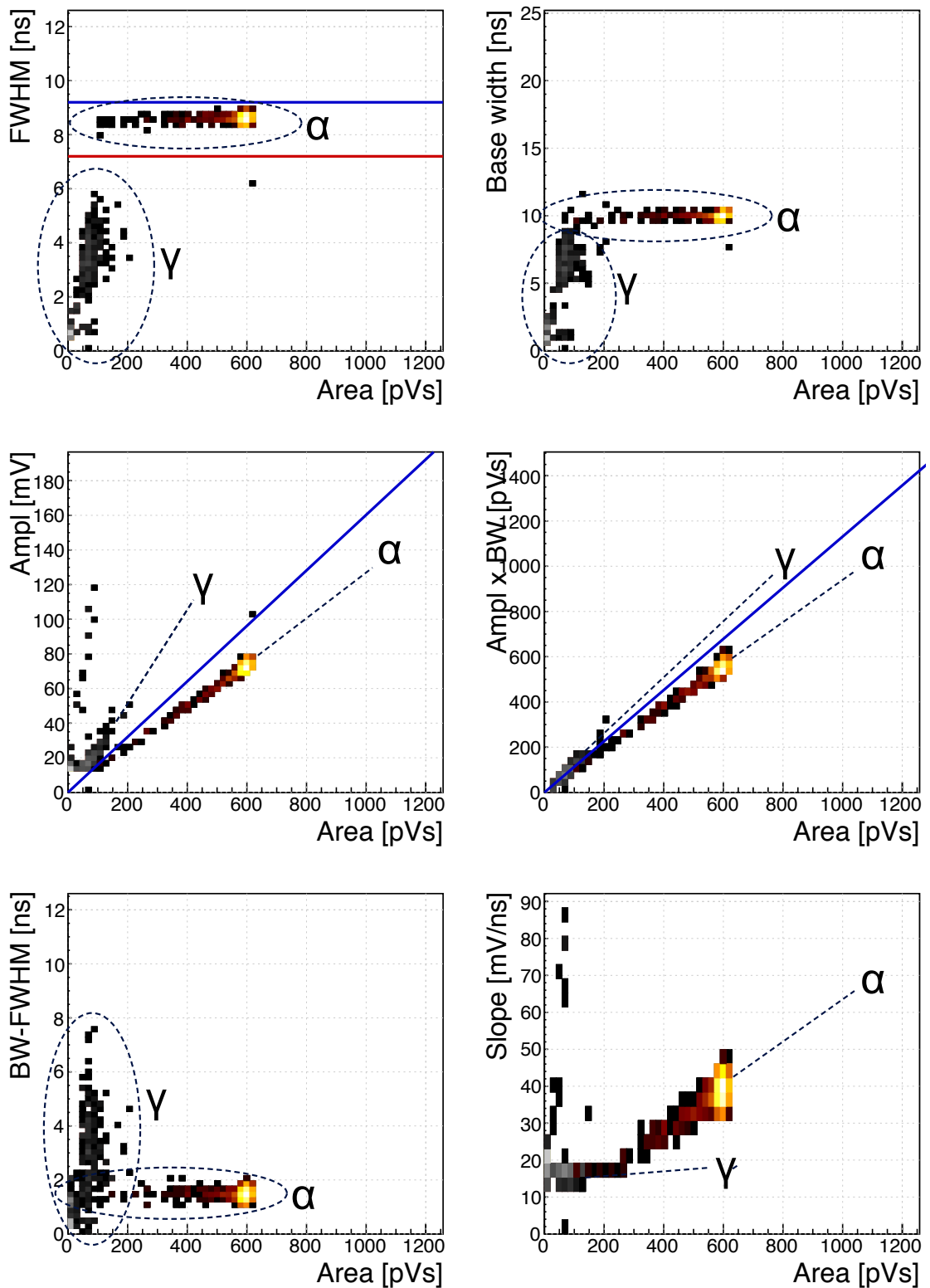


Figure 5.16:  $^{241}\text{Am}$ ,  $e^-$  collection. Qualifier: FWHM. Optional qualifiers: Amplitude, Form Factor.

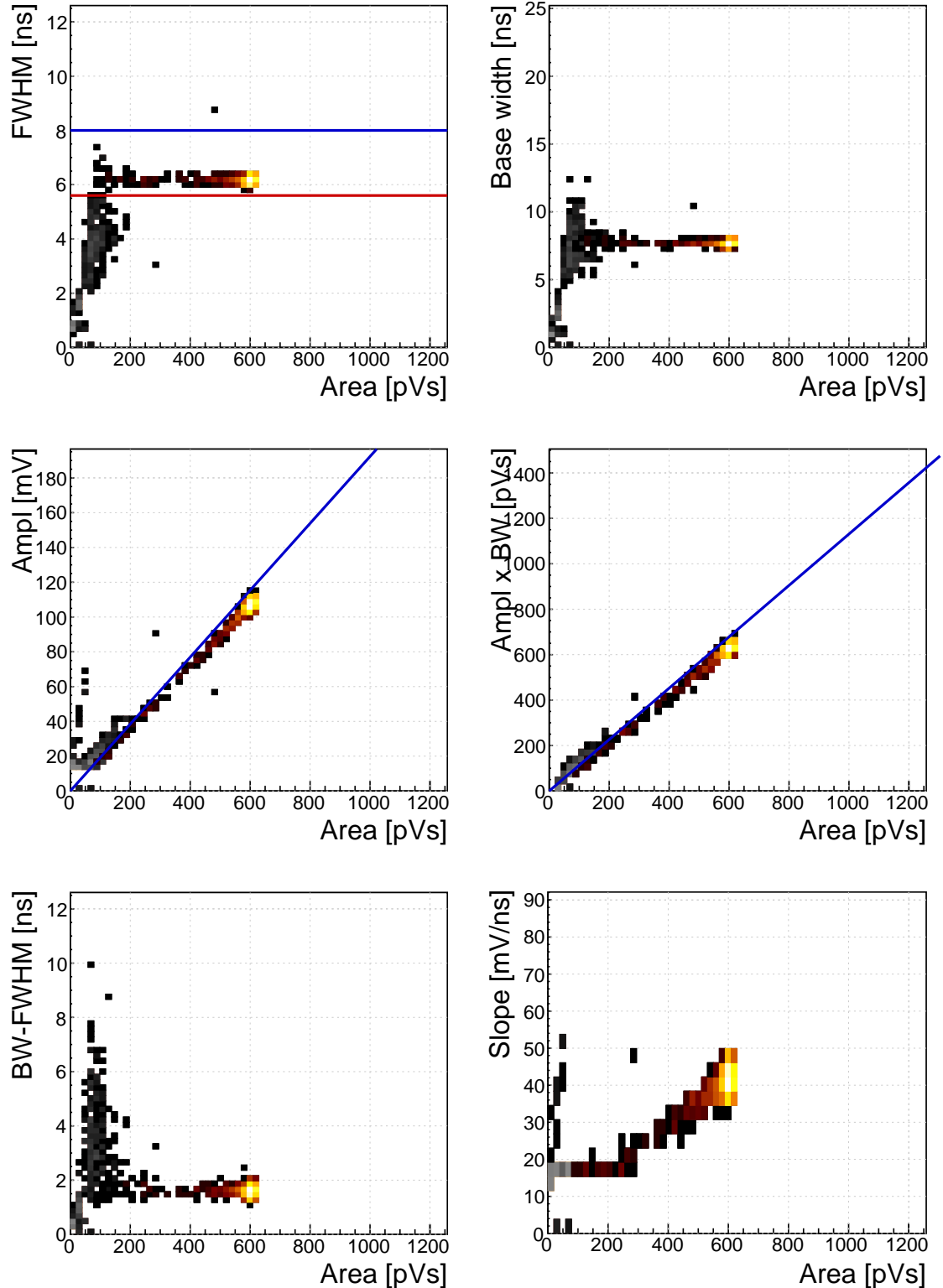
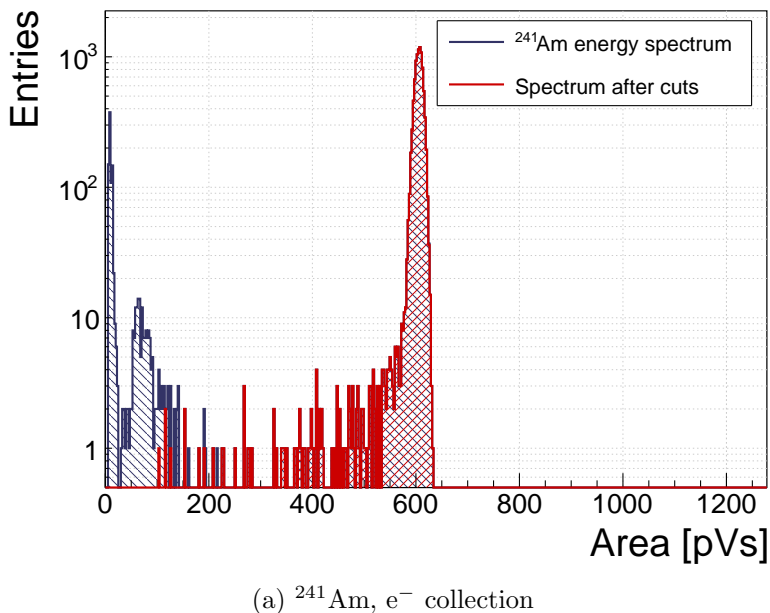


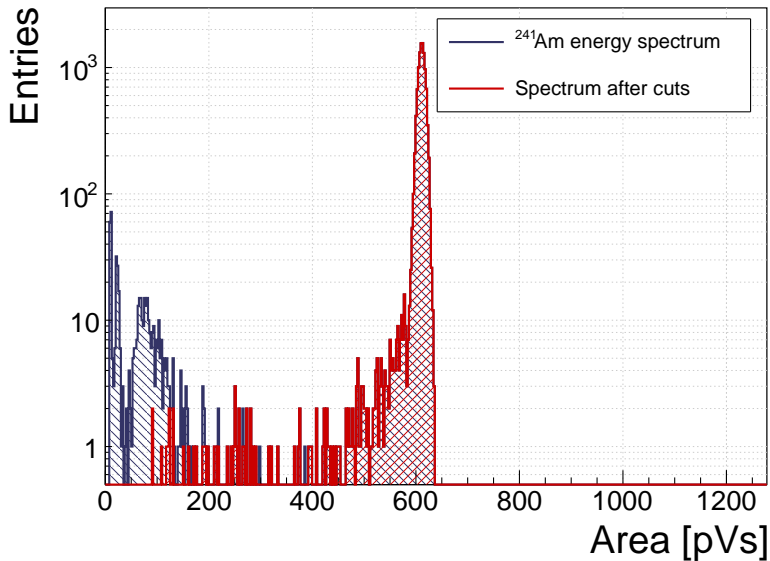
Figure 5.17:  $^{241}\text{Am}$ ,  $\text{h}^+$  collection. Qualifier: FWHM.

## 5.9. SOURCE CALIBRATION

---



(a)  $^{241}\text{Am}, e^-$  collection



(b)  $^{241}\text{Am}, h^+$  collection

Figure 5.18:  $^{241}\text{Am}$  area histograms for electron and hole collection.

2564 **5.9.1.2  $^{90}\text{Sr}$  and  $^{60}\text{Co}$  source**

2565 The phase space of the  $^{90}\text{Sr}$  source overlaps entirely with that of the  $^{60}\text{Co}$  source (see  
2566 figures 5.19 and 5.20). This renders it virtually impossible to distinguish between  
2567 photons and electrons (MIPs). Comparing the [area, FWHM] phase space of the  
2568 photons and alphas and the high reach of the former, the electron collection of the  
2569 alphas would need to be used to distinguish between the two types of particles.

2570 The one-dimensional histograms in figure 5.21 show a quasi-Landau distribution  
2571 with the MPV at  $\sim 70$  pVs, which is in agreement with the background  $\gamma$  radiation  
2572 emitted by the  $^{241}\text{Am}$  source (see figure 5.18 in the previous subsection). This is  
2573 however not a pure Landau distribution. Relative to the 600 pVs  $\alpha$  peak, the expected  
2574 MPV of MIPs would be  $\sim 30$  pVs, which is not the case in these distributions. This  
2575 is because the PSA device is a self-triggering system, which cuts the lower energetic  
2576 particles with the trigger threshold. The resulting distribution is therefore only the  
2577 top portion of the real Landau distribution. Unfortunately this is the limitation of  
2578 the device, governed by the analog noise of the current pre-amplifier.

## 5.9. SOURCE CALIBRATION

---

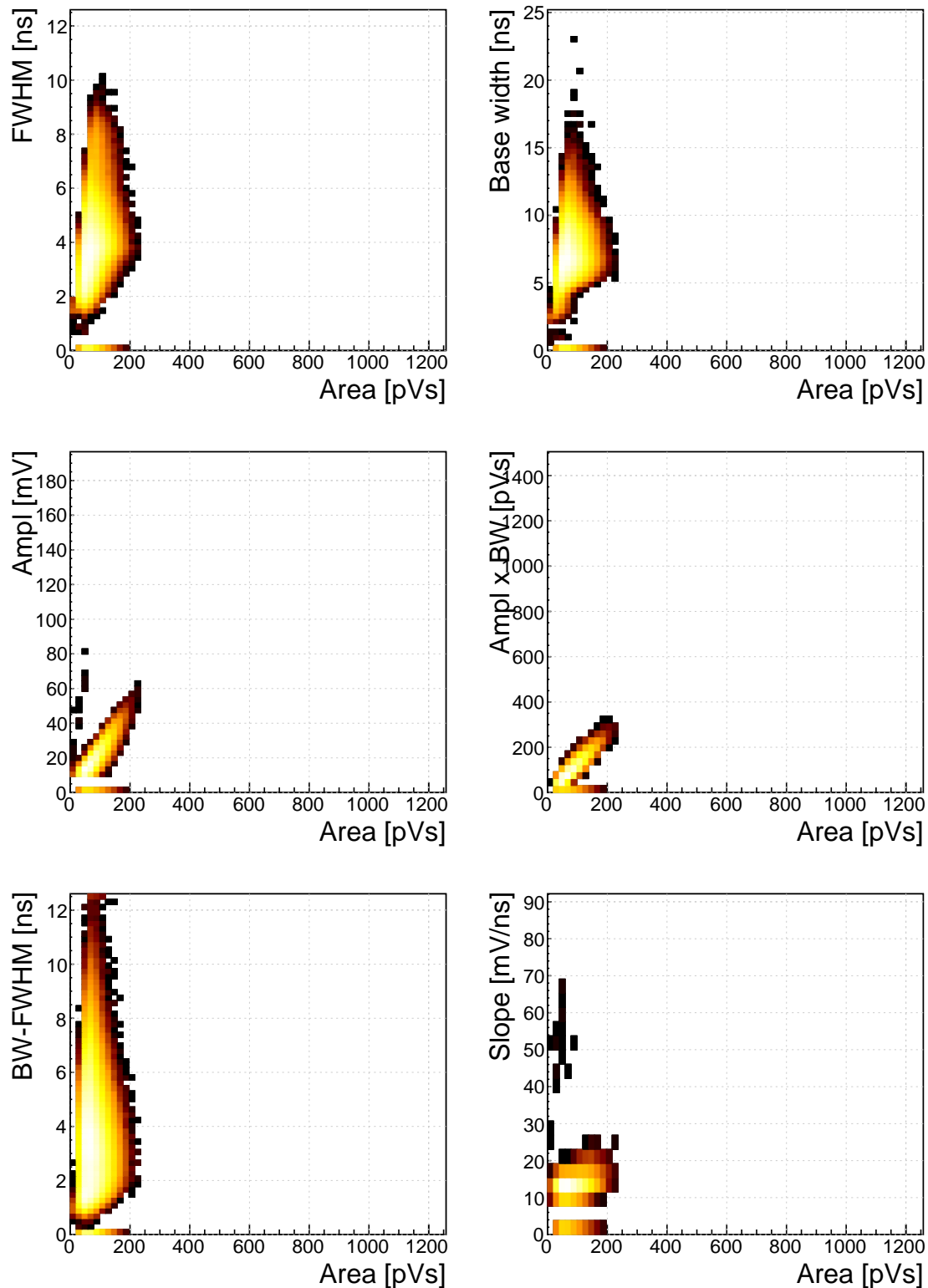


Figure 5.19:  $^{90}\text{Sr}$  scatter plots

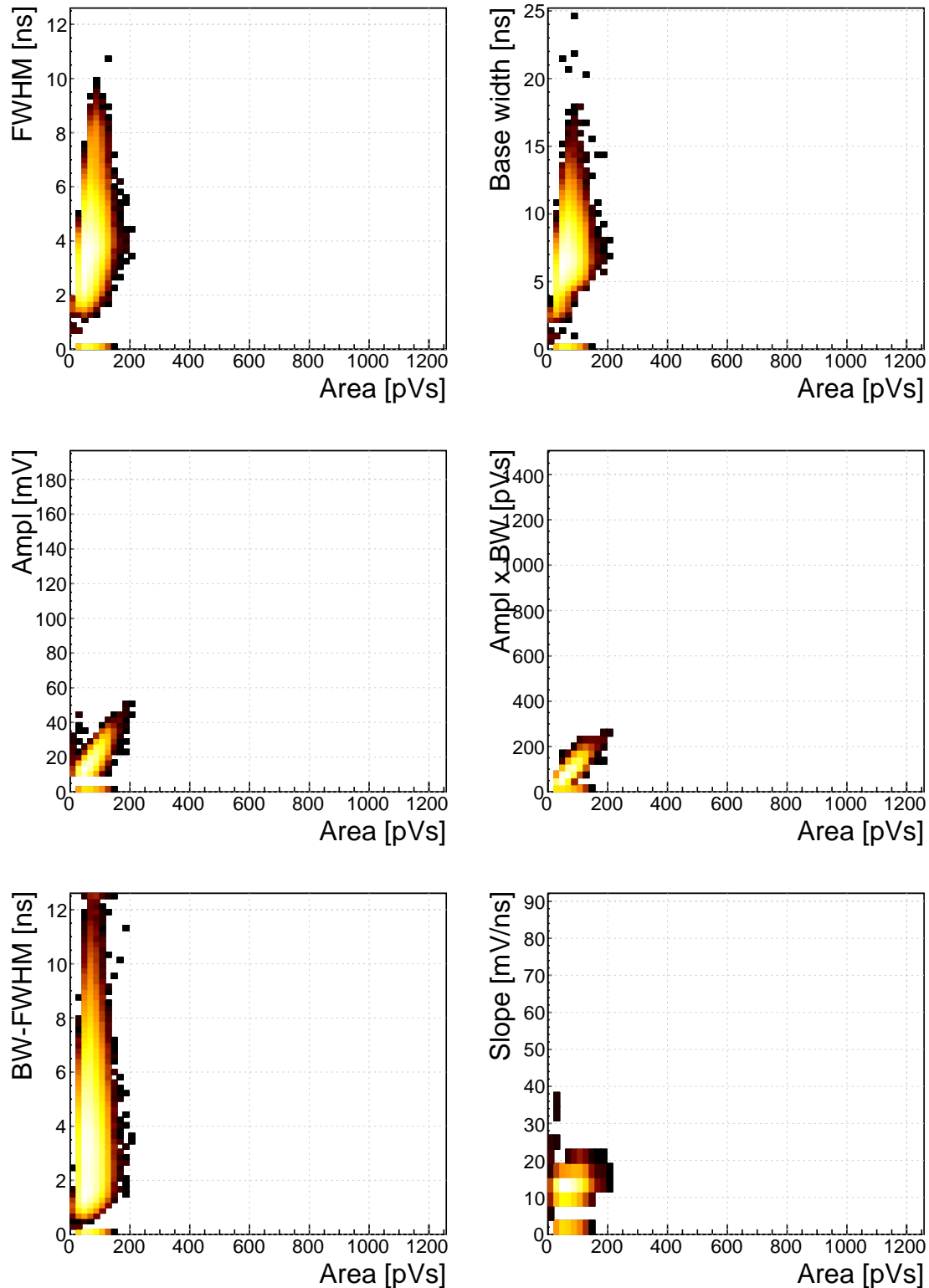


Figure 5.20:  $^{60}\text{Co}$  scatter plots

## 5.9. SOURCE CALIBRATION

---

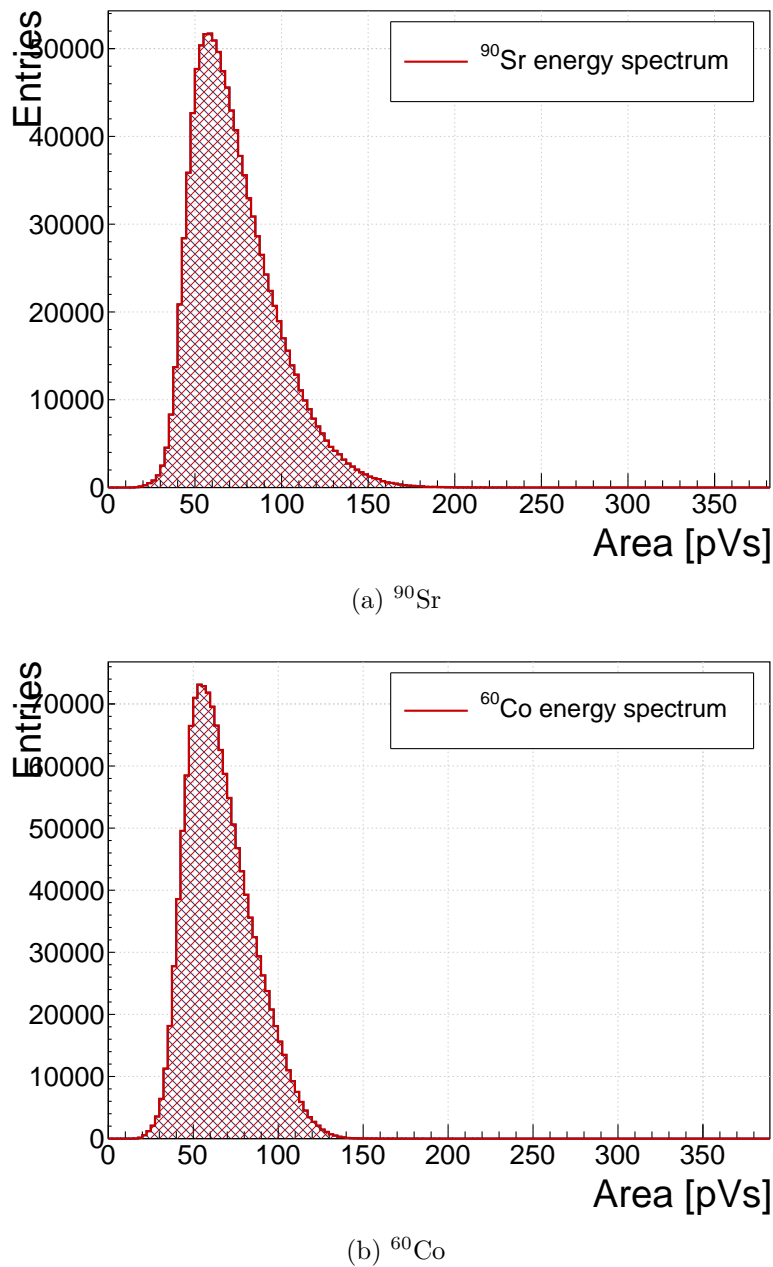


Figure 5.21: Energy distributions for  $\gamma$  and  $\beta$  particles.

## 2579 5.10 Applications in neutron instrumentation

2580 The real-time pulse shape analysis procedure can be applied to more complex systems.  
2581 This section includes three applications where the PSA has been applied.

2582 Semiconductor-based neutron detectors provide a compact technology for neutron  
2583 detection. However, the cross section of a neutron with the diamond bulk is very low,  
2584 since it only interacts with the core of the atom. Diamond is mainly used to detect  
2585 charged particles and photons.

2586 Research neutron reactors radiate a mix of particles, apart from neutrons also  
2587 photons. The photons are considered a background radiation, concealing the neutron  
2588 spectrum. When measured with diamond, the signal from neutrons is difficult to  
2589 distinguish from the photon spectrum. In addition, low energy neutrons do not cause  
2590 nuclear reactions in the bulk. All in all, the neutron measurements in a reactor present  
2591 a challenge with diamond. However, by means of the PSA, the neutron signal can be  
2592 discriminated from the photon background to some extent. The following two cases  
2593 show how measurements of fast ( $n^+$ ) and thermal ( $n^-$ ) neutrons have been carried  
2594 out by making use of the PSA.

2595 Note the changing scale on the X axis in the figures.

### 2596 5.10.1 Thermal neutron flux monitoring

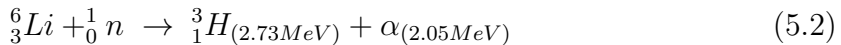
2597 Research neutron reactors like TRIGA MARK II [?] at Atominstitut [?] in Vienna  
2598 are capable of emitting neutrons at a wide range of energies. The neutron flux is  
2599 proportional to the current power of the reactor. It is therefore instrumental to  
2600 monitor the neutron flux to make sure that the reactor operation is within the specified  
2601 limits. However, the byproduct of the radioactive decays in the core is  $\gamma$  radiation,  
2602 which has an energy range that overlaps with that of neutrons, making it difficult to  
2603 measure the neutron flux. This is where PSA and diamond detectors come into play.  
2604 This section describes the application of thermal neutron flux monitoring by means  
2605 of the PSA.

2606 Thermal neutrons do not interact with the diamond bulk due to their low ki-  
2607 netic energy (of the order of 0.012 eV). Hence a converter foil has to be added to  
2608 produce second order effects. Incoming neutrons interact with the foil, producing  
2609 a set of secondary particles. These can then be detected upon hitting the detector  
2610 bulk. Common neutron interactions that are used in thermal neutron detection are  
2611  $^{10}\text{B}(\text{n},\alpha)^7\text{Li}$  reaction and  $^6\text{Li}(\text{n},\alpha)^3\text{H}$  reaction ( $\alpha$  stands for  $^4_2\text{He}$ , see equation 5.2).  
2612 The focus in this section is on the latter. With a foil installed, there are several  
2613 possibilities for neutrons to interact with the detector system. Each of these inter-  
2614 actions ionises the diamond bulk in its own way, resulting in a specific shape of the  
2615 current pulse. A neutron can: 1) interact with the foil, producing an  $\alpha$  and a  $^3\text{H}$ , 2)  
2616 interact with a carbon atom in the lattice, producing an  $\alpha$  and a  $\gamma$  or even three  $\alpha$ .  
2617 The thermal neutrons do not have enough kinetic energy to interact with the lattice,

## 5.10. APPLICATIONS IN NEUTRON INSTRUMENTATION

---

2618 therefore the focus will be on case (1), the equation for this reaction is the following:



2619 The particles in the first case are produced outside the diamond and get stopped  
2620 immediately upon hitting the sensor. The resulting pulses for both particles have a  
2621 rectangular shape of the same width, because the carriers drift with the same speed  
2622 in both cases. The difference is in the number of free carriers produced - the tritium  
2623 creates more (proportional to the deposited energy), which in turn induces a higher  
2624 pulse.

2625 TRIGA MARK II neutron reactor emits large amounts of  $\gamma$  radiation in the  
2626 energy range up to 3 MeV. This already affects the measurements of  $\alpha$  particles, the  
2627 energy of which peaks at 2.05 MeV in the case of  ${}^6Li$  converter foil. However,  $\gamma$   
2628 background radiation can be suppressed by discriminating current pulses of photons  
2629 from those induced by  $\alpha$  particles. This idea has already been implemented in offline  
2630 analysis in [29, 24]. The results show that the background photons can be subtracted  
2631 successfully. In order to make sure that every single incident thermal neutron has  
2632 been accounted for, the algorithm has been ported to FPGA where it detects and  
2633 analyses particles in real time.

### 2634 5.10.1.1 Measurements

2635 ROSY readout device with the implemented Pulse Shape Analysis was put to a test  
2636 at Atominstut in Vienna. Their TRIGA neutron reactor is capable of delivering  
2637 thermal neutrons with the energy 0.012 eV at a rate of  $10^3 n \text{ cm}^{-2} s^{-1}$ , with a  
2638 considerable  $\gamma$  background.

2639 First, the device was calibrated using an unsealed monochromatic  ${}^{241}Am$  source  
2640 with the emitted particle energy  $E_\alpha = 5.12MeV$  (taking into account the losses in  
2641 the air). Then the diamond detector was exposed to the beam. Secondary reaction  
2642 products ( $\alpha$  and  ${}^3H$  particles), created by neutrons hitting the converter foil, were  
2643 detected by the diamond sensor, together with a significant photon background. Then  
2644 the pulse identification algorithm was applied to discriminate between the reaction  
2645 products and the photons.

2646 The main parts of the detector are an sCVD diamond sensor sized  $4.7 \times 4.7 \text{ cm}^2$   
2647 and a  $1.8 \mu\text{m}$  thick LiF converter foil, both embedded in an RF-tight PCB. The  
2648 diamond sensor is biased with a bias voltage of  $1 \text{ V}/\mu\text{m}$  and capacitively coupled to  
2649 CIVIDEC's C2 40 dB wide bandwidth current preamplifier. A 5 m long BNC cable  
2650 connects the preamplifier to CIVIDEC ROSY box. The detector assembly together  
2651 with the preamplifier has to be placed in front of an exit hole of the reactor.

2652 Note: this data set has been taken with an older version of the firmware, which  
2653 only measured a limited number of pulse parameters.

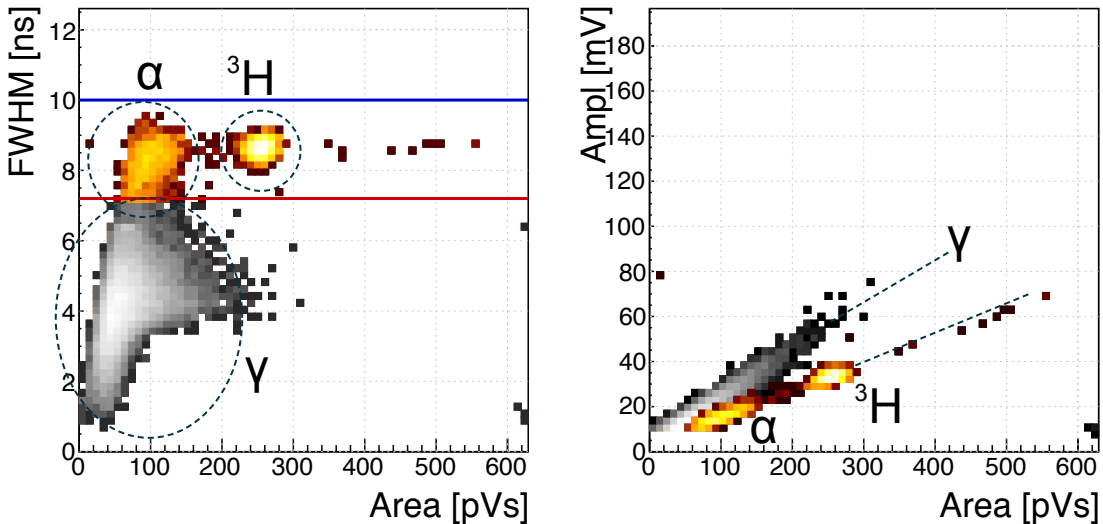


Figure 5.22: Thermal neutrons, photons. Qualifier: FWHM.

#### 2654 5.10.1.2 Results and discussion

2655 The data collected by the PSA show a high flux of photons, which covers a wide area  
 2656 range. The  ${}^3\text{He}$  peak is clearly visible and has almost no overlap with the photon  
 2657 cluster. The  $\alpha$  cluster has a much lower energy and is in the same energy range  
 2658 as the photons. However, if a FWHM parameter is observed, a distinction between  
 2659 the photons and the  $\alpha$  can be seen. By setting a qualifier to the right value, the  
 2660 photon background is cut away, leaving only the thermal neutron decay products in  
 2661 the data set (see figure 5.22). The resulting one-dimensional area histogram before  
 2662 and after applied cuts is shown in figure 5.23. The blue distribution is the mixed field  
 2663 of background photons, tritium and  $\alpha$  particles. The latter are completely hidden in  
 2664 the  $\gamma$  energy distribution. After applied qualifiers the  $\alpha$  peak suddenly appears.

#### 2665 5.10.1.3 Conclusion

2666 By applying the FWHM qualifier to the acquired data from the TRIGA neutron reactor,  
 2667 the  $\alpha$  and tritium particles can be identified and separated from the  $\gamma$  background.  
 2668 The resulting cleaned data can be used to correctly count the thermal neutrons de-  
 2669 tected by the diamond sensor.

#### 2670 5.10.2 Fusion power monitoring

2671 Many research collaborations around the world are trying to develop a functional  
 2672 fusion reactor, which could provide a cleaner energy source. One of them is ITER [8],  
 2673 a research fusion reactor being built in France. The idea behind it is to harvest  
 2674 energy from the fusion of light atoms into a heavier one. For ITER the fuel chosen

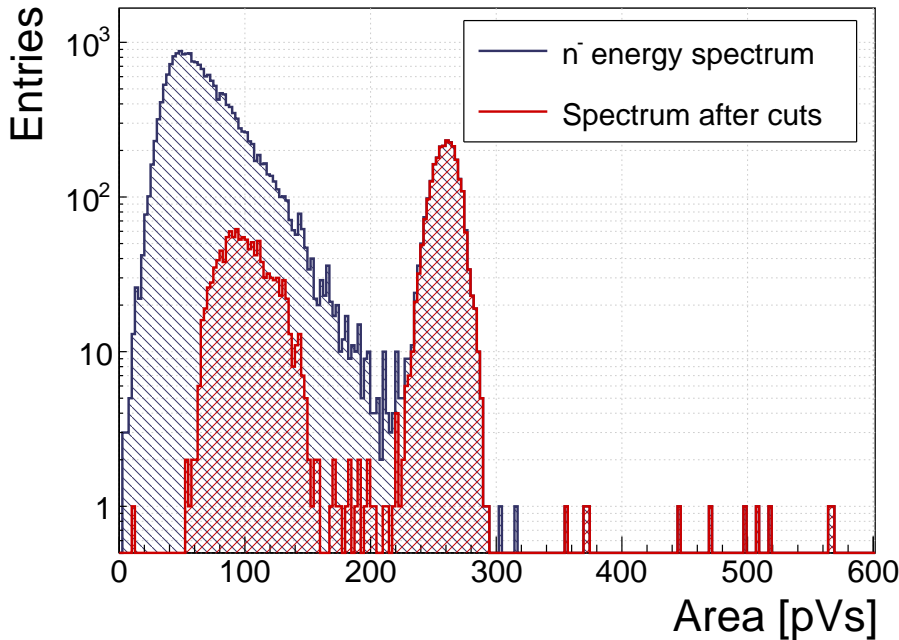


Figure 5.23: Energy spectrum after applied qualifiers reveals the tritium and  $\alpha$  peak

2675 is a mixture of deuterium and tritium, which fuse into a helium atom at extremely  
 2676 high temperatures (plasma), emitting a highly energetic neutron as a byproduct. The  
 2677 equation is the following:



2678 The  $\alpha$  particle immediately deposits its energy within the plasma. The neutron, due  
 2679 to its neutral charge, continues its way out of the system where it is stopped. The  
 2680 stopping power is converted into energy, which heats the water into steam, which in  
 2681 turn spins the turbines, generating electricity.

2682 It is possible to monitor the activity of the reactor by measuring the flux of neu-  
 2683 trons emitted. Neutron diagnostics such as neutron cameras, neutron spectrometers  
 2684 and neutron flux monitors therefore provide robust measurements of fusion power. A  
 2685 high  $\gamma$  background makes it difficult to accurately measure the neutron flux. This is  
 2686 a motivation to use a diamond based detector with a real-time PSA algorithm.

2687 The neutrons emitted are 14 MeV mono-energetic fast neutrons. The most ac-  
 2688 curate and efficient way to detect them with a diamond detector is by means of a  
 2689  $C_{12}(n,\alpha)$  reaction with a carbon atom in the ballistic centre [30]. In this region the  
 2690 positive and negative charge carriers created by  $\alpha$  that start drifting in the opposite  
 2691 directions need the same time to reach the opposite electrodes.

2692 **5.10.2.1 Measurements**

2693 The  ${}^{239}\text{Pu Be}$  neutron source has been used to simulate the fusion reactor. It emits a  
 2694 mixed field of neutrons and photons with a wide range of energies. The neutrons are

2695 rarely detected with diamond – the interactions happen mostly in the electrodes on  
2696 either side of the detector. The  $\alpha$  particles created by the interactions are detected  
2697 by the diamond. Depending on the side of the interaction, the created pulse is either  
2698 due to hole– or electron collection. These two interactions make the two distinct lines  
2699 in the [area, FWHM] phase space (see figure 5.24, top left plot) at 9 ns and 6 ns.

2700 A very interesting interaction point is the ballistic centre [?] of the diamond. A  
2701 ballistic centre is the position from which it takes the holes and the electrons the  
2702 same amount of time to drift to the opposite electrodes. In this case the shortest  
2703 possible pulse is created. Conversely, to conserve the collected charge and thus the  
2704 pulse area, the pulse amplitude must be the highest at the ballistic centre. The entries  
2705 in between are created by neutron interactions at random positions in the diamond,  
2706 which produce pulses of various shapes.

### 2707 5.10.2.2 Results and discussion

2708 Coming back to the motivation, the most efficient way of counting the 14 MeV neu-  
2709 trons is through the measurement of the neutrons interacting in the ballistic centre [?].  
2710 To extract this type of interaction several qualifiers must be used. The first possibility  
2711 is the FWHM set to 3–5 ns. However, this time the cuts on the [area, amplitude]  
2712 and the [area, amplitude  $\times$  base value] phase space are preferred. First, a minimum  
2713 constant amplitude qualifier is set to 22 mV (see figure 5.24, middle left plot). Then a  
2714 linear amplitude qualifier is set such that only the pulses with the highest amplitude  
2715 for every area value are taken. This ensures that the high pulses from the ballistic  
2716 centre are chosen. Second, a maximum linear amplitude  $\times$  base value qualifier is set  
2717 such that only the pulses bearing the closest resemblance to a rectangle are chosen  
2718 (see figure 5.24, middle right plot). In this phase space the entries at the bottom of  
2719 the distribution are bearing more resemblance to a rectangle whereas those at the top  
2720 are more akin to triangles.

2721 The resulting [area, FWHM] subfigure after applied qualifiers highlights the entries  
2722 with a FWHM of 4 ns, which is the width of the pulses induced by neutrons interacting  
2723 in the ballistic centre. This proves that these combined qualifiers indeed pinpoint  
2724 these neutron interactions. The final one-dimensional area/energy distribution of the  
2725 neutrons interacting in the ballistic centre is shown in figure 5.25.

2726 The result could be further improved by further constraining the identification,  
2727 e.g to define the minimum FWHM constant qualifier and the minimum slope constant  
2728 qualifier.

### 2729 5.10.2.3 Conclusion

2730 By applying the appropriate qualifiers to the data, the neutron interactions in the  
2731 ballistic centre can be identified.

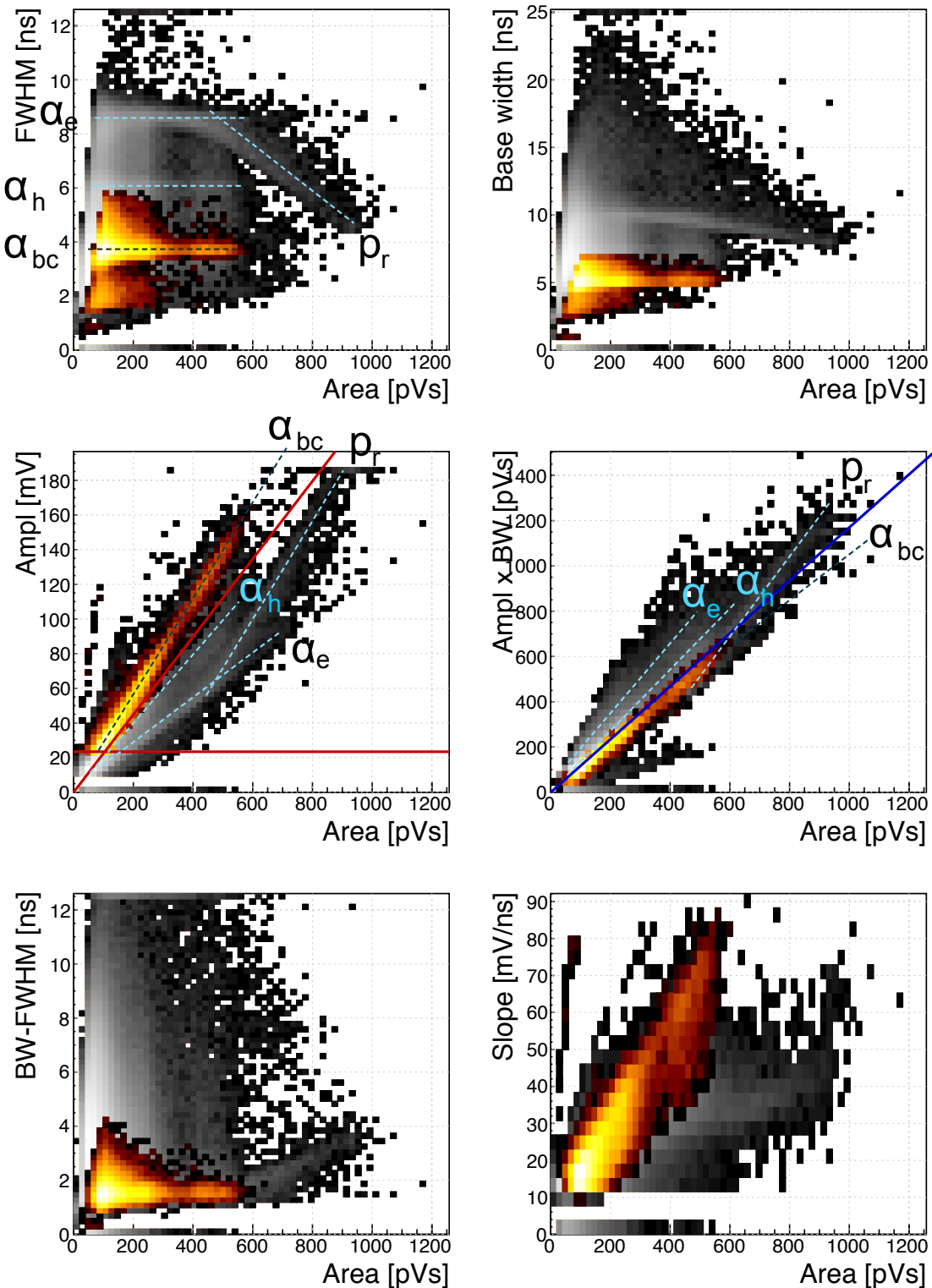


Figure 5.24:  $^{239}\text{Pu Be}$ . Qualifiers: BW-FWHM, FWHM, Form Factor

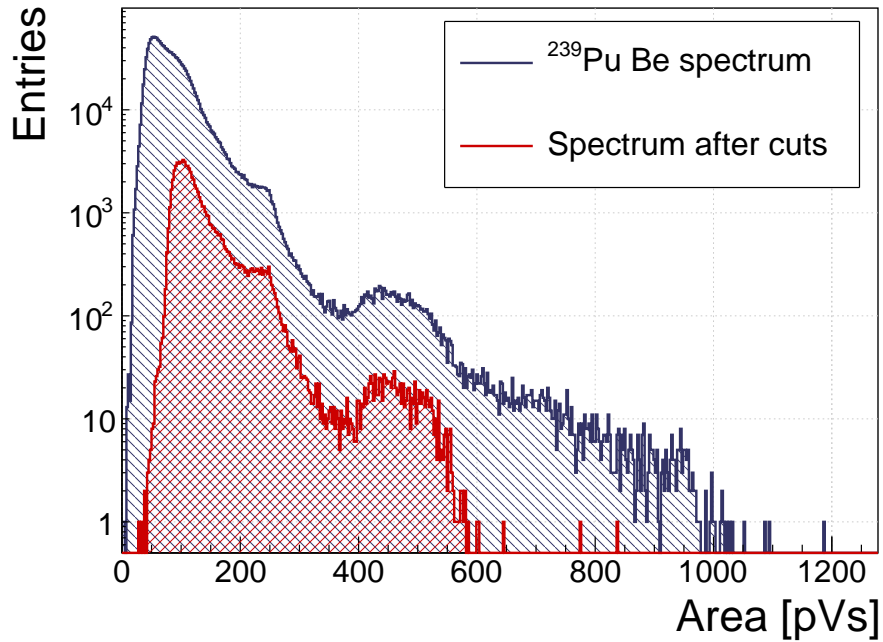


Figure 5.25:  $^{239}\text{Pu}$  Be, energy distribution of the neutrons interacting in the ballistic centre.

### 5.10.3 Fast and thermal neutron monitoring

The CROCUS reactor at EPFL [3] is a research neutron reactor. The research group working on the reactor is interested in measuring neutrons with energies between 1–2 MeV, which is overlapping with the  $\gamma$  background energy range.

The highest output power of the CROCUS reactor is 100 W. Currently there are fission chambers that carry out the neutron counting, which is a measure of the activity of the reactor. The new goal is to measure both neutrons and photons, but separately. The pulse shape analysis is a good solution for this task. For this, a 400  $\mu\text{m}$  thick diamond detector with a specially designed casing was added to measure the activity. The LiF foil was added for conversion of thermal neutrons. The ROSY box with the integrated PSA routine was used for signal analysis.

#### 5.10.3.1 Measurements

At the highest reactor activity the system counts particles at a rate of  $\sim 1.5 \times 10^5 \text{ s}^{-1}$ . The results from a test run at 10 W output power are shown in figure 5.26. The data include a mixed field consisting of fast neutrons, photons and of  $\alpha$  and  $^3\text{H}$  particles as products of thermal neutron decay in the LiF foil in front of the detector. The energy deposited in the diamond is not as high as that from the  $^{239}\text{Pu}$  Be source. In addition, the analog noise during this measurement is higher than in the previous application. These conditions combined make particle identification at CROCUS a challenging task.

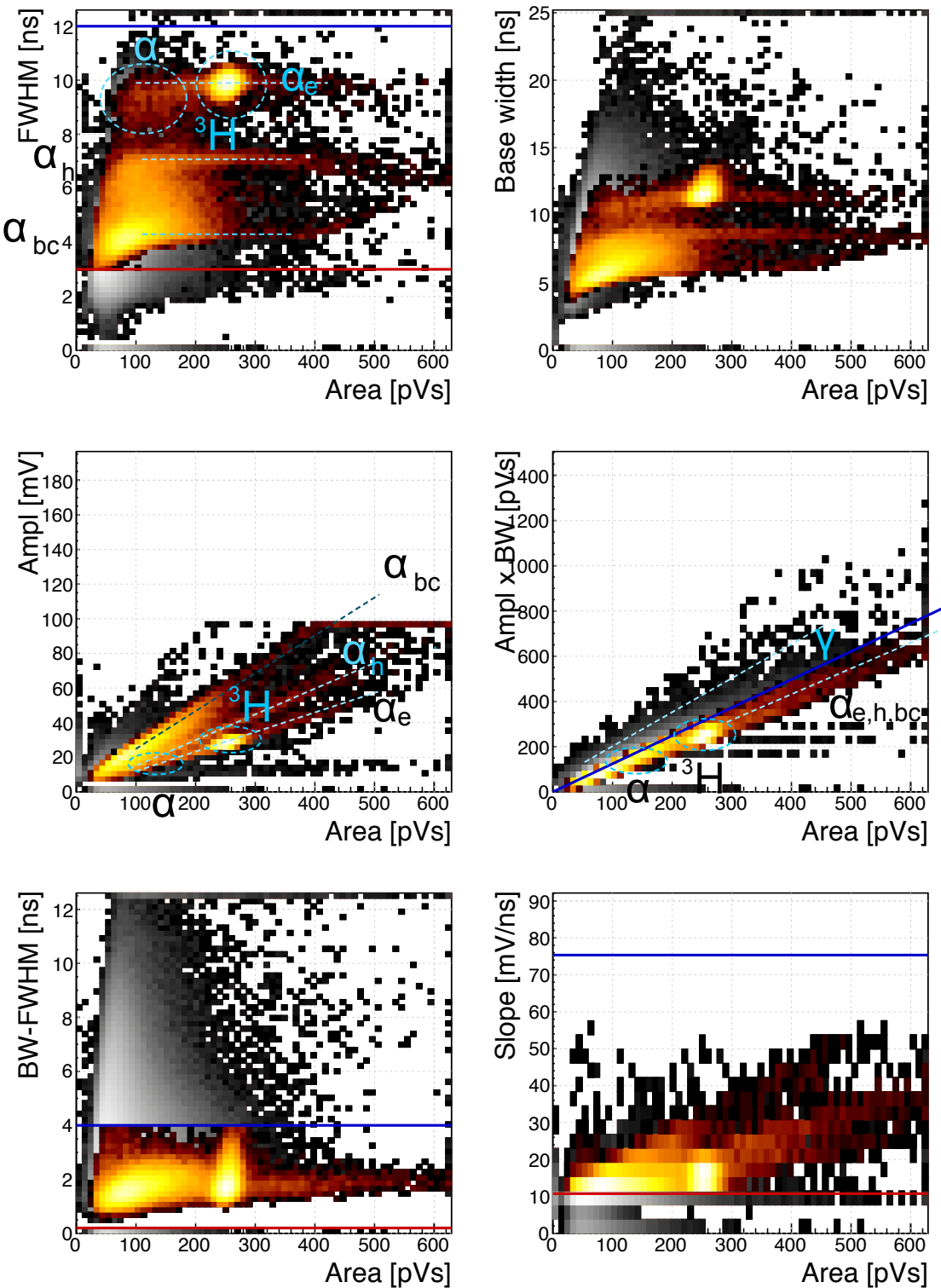


Figure 5.26: Fast neutrons, thermal neutrons, photons. Qualifiers: BW-FWHM, FWHM, Form factor, Slope.

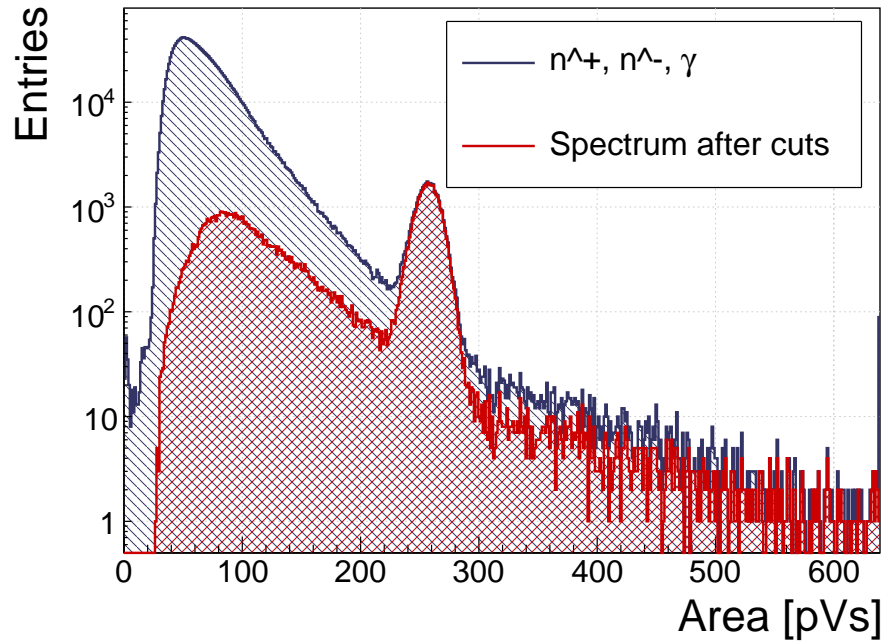


Figure 5.27: Energy spectrum in CROCUS before and after applied qualifiers

### 2752 5.10.3.2 Results and discussion

2753 The aim of this exercise is to identify both thermal and fast neutrons. For this the  
 2754 main qualifier used is the Form Factor - the linear line in the [area, amplitude×base  
 2755 value] phase space. Additional FWHM, FWHM-BW and slope constant qualifiers are  
 2756 used to clean the outlying entries. The resulting accepted entries in figure 5.26 have  
 2757 the distinctive three-line fast neutron signature in the [area, FWHM] subfigure with  
 2758 two superimposed islands by the  $\alpha$  and  ${}^3\text{H}$  cluster produced by thermal neutrons in the  
 2759 LiF foil. The  $\gamma$  background is sufficiently suppressed. The resulting one-dimensional  
 2760 histogram of the area/energy distribution is shown in figure 5.27.

### 2761 5.10.3.3 Conclusion

2762 By applying the Form Factor qualifier both fast and thermal neutrons can be identi-  
 2763 fied, suppressing the  $\gamma$  background.

2764 **5.11 Conclusion**

2765 This chapter describes a system that can identify the type of radiation in real time.  
2766 The system is implemented on an FPGA in a CIVIDEC ROSY box and is used with  
2767 diamond detectors. The signal from the diamond sensor is read in and analysed in the  
2768 firmware. First the shape of the pulse is parametrised. Then the logic determines the  
2769 type of particle according to the user defined cuts. Finally the parameters are written  
2770 into a histogram, which is read out by the user. The firmware is designed to carry  
2771 out the pulse shape analysis of a single pulse in  $\sim 200$  ns, yielding a maximum pulse  
2772 rate of  $5 \times 10^6$  particles per second. The rate as well as the linearity the measurement  
2773 stability with respect to noise have been verified using a pulse generator. Then several  
2774 radioactive sources were used to calibrate the device. Finally the system has been set  
2775 up in two neutron reactors to test the operation in a mixed field containing thermal  
2776 neutrons, fast neutrons and photons. The identification can be optimised using a  
2777 combination of qualifiers to achieve the desired effect.

<sub>2778</sub>

# Bibliography

- <sub>2779</sub> [1] *ASIC*. [http://www.embedded-systems-portal.com/CTB/CTB\\_images/L2/L2 ASIC.jpg](http://www.embedded-systems-portal.com/CTB/CTB_images/L2/L2 ASIC.jpg).
- <sub>2780</sub> [2] *Atominstitut, Technical University of Vienna, Austria*.  
<sub>2781</sub> <http://ati.tuwien.ac.at/startpage/EN/>.
- <sub>2782</sub> [3] *CROCUS neutron reactor*. <http://lrs.epfl.ch/page-55655-en.html>.
- <sub>2783</sub> [4] *DRS4*. <https://www.psi.ch/drs/evaluation-board>.
- <sub>2784</sub> [5] *Element Six*. <http://www.e6.com>.
- <sub>2785</sub> [6] *European Centre for Nuclear Research, CERN*. <http://home.cern>.
- <sub>2786</sub> [7] *IHa Technologies Pte. Ltd.* <https://www.2atechnologies.com>.
- <sub>2787</sub> [8] *ITER fusion reactor*. <https://www.iter.org/>.
- <sub>2788</sub> [9] *Neutron Time-of-flight experiment*. <https://ntof-exp.web.cern.ch/ntof-exp/>.
- <sub>2789</sub> [10] *Paul Scherrer Institute*. <https://www.psi.ch/>.
- <sub>2790</sub> [11] *RD42 collaboration*. <http://rd42.web.cern.ch/rd42/>.
- <sub>2791</sub> [12] *TRIGA MARK II neutron reactor*. <http://ati.tuwien.ac.at/reactor/EN/>.
- <sub>2792</sub> [13] *Xilinx Virtex 5 FPGA*. <http://www.hdl.co.jp/XCM-109/top.560.jpg>.
- <sub>2793</sub> [14] *Determination of operational dose equivalent quantities for neutrons*. ICRU,  
<sub>2794</sub> Washington, DC, 2001.
- <sub>2795</sub> [15] General Atomics. *View of the TRIGA reactor*. 2015.
- <sub>2796</sub> [16] H. Bethe and J. Ashkin. *Experimental Nuclear Physics*, ed. E. Segre, page 253,  
<sub>2797</sub> 1953.
- <sub>2798</sub> [17] W. Blum, W. Riegler, and L. Rolandi. Particle Detection with Drift Chambers,  
<sub>2799</sub> volume 2 of 2. Springer-Verlag, Berlin Heidelberg, 2008.
- <sub>2800</sub> [18] Giorgio Brianti. SPS North Experimental Area. Technical Report CERN-SPSC-  
<sub>2801</sub> T-73-8. LabII-EA-Note-73-4, CERN, Geneva, 1973.

## BIBLIOGRAPHY

---

- 2802 [19] Maximilien Brice. *View of the nTOF detector*. Oct 2010.
- 2803 [20] Maximilien Brice. *LHC tunnel*. Jan 2011.
- 2804 [21] P. Carazzetti and H. R. Shea. *Electrical breakdown at low pressure for planar*  
2805 *microelectromechanical systems with 10- to 500  $\mu\text{m}$  gaps*. *J. Micro/Nanolith.*  
2806 *MEMS MOEMS*, (8(3), 031305), Jul-Sep 2009.
- 2807 [22] Daniel Dominguez. *Standard Model. Le modele standard*. General Photo, Mar  
2808 2015.
- 2809 [23] CIVIDEC Instrumentation GmbH. *sCVD diamond sensor*.  
2810 <http://www.cividec.at>, 2015.
- 2811 [24] E. Griesmayer, R. Bergmann, H. Böck, M. Cagnazzo, P. Kavrigin, B. Morgenbesser,  
2812 and M. Villa. *A Novel Neutron Flux Monitor Based On Diamond*  
2813 *Detectors at the Vienna TRIGA Mark II Reactor*. submitted to the proceedings  
2814 of ICRR 2015, 2015.
- 2815 [25] E. Griesmayer and B. Dehning. Diamonds for beam instrumentation. *Physics*  
2816 *Procedia*, 37:1997 – 2004, 2012. Proceedings of the 2nd International Conference  
2817 on Technology and Instrumentation in Particle Physics (TIPP 2011).
- 2818 [26] Moritz Guthoff, Wim de Boer, and Steffen Müller. Simulation of beam induced  
2819 lattice defects of diamond detectors using {FLUKA}. *Nuclear Instruments and*  
2820 *Methods in Physics Research Section A: Accelerators, Spectrometers, Detectors*  
2821 *and Associated Equipment*, 735:223 – 228, 2014.
- 2822 [27] M. Huhtinen. Simulation of non-ionising energy loss and defect formation in  
2823 silicon. *Nuclear Instruments and Methods in Physics Research A*, 491:194–215,  
2824 September 2002.
- 2825 [28] Hendrik Jansen, Norbert Wermes, and Heinz Pernegger. *Chemical Vapour Deposition*  
2826 *Diamond - Charge Carrier Movement at Low Temperatures and Use in*  
2827 *Time-Critical Applications*. PhD thesis, Bonn U., Sep 2013. Presented 10 Dec  
2828 2013.
- 2829 [29] P. Kavrigin, P. Finocchiaro, E. Griesmayer, E. Jericha, A. Pappalardo, and  
2830 C. Weiss. *Pulse-shape analysis for gamma background rejection in thermal*  
2831 *neutron radiation using CVD diamond detectors*. *Nuclear Instruments and Methods*  
2832 *in Physics Research A*, (795), 2015.
- 2833 [30] P. Kavrigin, E. Griesmayer, F. Belloni, A.J.M. Plompen, P. Schillebeeckx, and  
2834 C. Weiss.  $^{13}\text{C}(n,\alpha_0)^{10}\text{Be}$  cross section measurement with sCVD diamond detector.  
2835 submitted to EPJA, 2016.
- 2836 [31] Claude A. Klein. Radiation-induced energy levels in silicon. *Journal of Applied*  
2837 *Physics*, 30(8):1222–1231, 1959.

## BIBLIOGRAPHY

---

- 2838 [32] Gregor Kramberger, V. Cindro, A. Gorisek, I. Mandic, M. Mikuz, and M. Zavr-  
2839 tanik. Effects of bias voltage during priming on operation of diamond detectors.  
2840 *PoS*, Vertex2012:013, 2013.
- 2841 [33] W. Y. Liang. Excitons. *Physics Education*, 5:226–228, July 1970.
- 2842 [34] Claudia Marcelloni De Oliveira. *IBL installation into the inner detector of the*  
2843 *ATLAS Experiment side C. General Photo*, May 2014.
- 2844 [35] M. Mikuž. *Diamond sensors for high energy radiation and particle detection*.  
2845 TIPP, 2011.
- 2846 [36] W P C Mills. *The present performance of the SPS*. *IEEE Trans. Nucl. Sci.*,  
2847 26(CERN-SPS-AOP-79-9):3176–3178. 3 p, Mar 1979.
- 2848 [37] S. F. Novaes. *Standard model: An Introduction*. In *Particles and fields. Pro-*  
2849 *ceedings, 10th Jorge Andre Swieca Summer School, Sao Paulo, Brazil, February*  
2850 *6-12, 1999*, 1999.
- 2851 [38] Joao Pequenao. *Computer generated image of the whole ATLAS detector*. Mar  
2852 2008.
- 2853 [39] Heinz Pernegger. *The Pixel Detector of the ATLAS Experiment for LHC Run-2*.  
2854 Technical Report ATL-INDET-PROC-2015-001, CERN, Geneva, Feb 2015.
- 2855 [40] S. Ramo. *Currents Induced by Electron Motion*. *Proceedings of the IRE*, 27:584–  
2856 585, 1939.
- 2857 [41] V. Sarin. *Comprehensive Hard Materials*. Elsevier Science, 2014. p. 411.
- 2858 [42] W. Shockley. *Currents to Conductors Induced by a Moving Point Charge*. *Journal*  
2859 *of applied Physics*, 9:635, 1938.
- 2860 [43] C. Weiss. A CVD diamond detector for  $(n,\alpha)$  cross-section measurements. PhD  
2861 thesis, TU Wien, Vienna, 2014.
- 2862 [44] C. Weiss, H. Frais-Kölbl, E. Griesmayer, and P. Kavrigin. *Ionization signals of*  
2863 *diamond detectors in fast neutron fields. publication in preparation*, 2016.
- 2864 [45] J. L. Yarnell, J. L. Warren, and R. G. Wenzel. Lattice vibrations in diamond.  
2865 *Phys. Rev. Lett.*, 13:13–15, Jul 1964.